Drying of complex fluids near the contact line : experimental and numerical studies

Ching Hsueh

THÈSE DE DOCTORAT DE L'UNIVERSITÉ PIERRE ET MARIE CURIE

Spécialité : Physique

Ecole doctorale : ≪ La Physique, de la Particule à la Matière Condensée ≫

réalisée au

Laboratoire FAST - UMR 7608 (UPMC-UPS-CNRS)
Bat. 502 - Campus Universitaire
91405 Orsay Cedex, FRANCE.

présentée par

Ching HSUEH

pour obtenir le grade de :

DOCTEUR DE L'UNIVERSITÉ PIERRE ET MARIE CURIE

Sujet de la thèse :

Drying of complex fluid near the contact line
- *experimental and numerical studies*

date de soutenance prévue le 5 Juillet 2012

Devant le jury composé de :

M. Yahya RHARBI	Rapporteur
M. Jean-Baptiste SALMON	Rapporteur
M. Pierre COLINET	Examinateur
Mme Martine MEIRELES	Examinateur
M. Dominique SALIN	Examinateur
Mme Béatrice GUERRIER	Directeur de thèse
M. Frédéric DOUMENC	Membre invitè

Table of Contents

Notations

Notations	Expressions
d	gap between two glass plates ($= 1mm$ in experimental set-up)
D	binary diffusion coefficient (m^2/s)
D_p	particle diameter (nm)
D_{tip}	distance to the contact line (m)
F	total volumetric evaporation flux per unit length in the z direction (m^2/s)
$h(t)$	in Ch 3: contact line displacement as a function of time (mm)
h	in Ch 4: H-h_m cf figure 4.1 (m)
h_m	the vertical height of the meniscus free surface cf figure 4.1 (m)
h_d	deposition thickness (m)
H	total height of 2D computational domain (m)
H_t	$H - \alpha$ cf figure 4.4 (m)
H_u	Humidity
j	local evaporation rate (m/s)
$\vec{J}$	local mass flux ($\frac{kg}{m^2 s}$)
$\vec{J}_p$	local mass flux of solute ($\frac{kg}{m^2 s}$)
$\vec{J}_s$	local mass flux of solvent ($\frac{kg}{m^2 s}$)
J_0	constant related to mean evaporation rate ($\frac{m^{3/2}}{s}$)
$\vec{n}$	normal vector to the meniscus
P	pressure (Pa)
Q	total volume flux of solution per unit length in the z direction (m^2/s)

Notations	Expressions
Q_p	total volume flux of solute per unit length in the z direction (m^2/s)
R	radius of the meniscus free surface
Re	Reynolds number
T	Temperature set for experiment $(°C)$
$\vec{t}$	tangential vector to the meniscus
$\vec{v}$	velocity vector
u	x component of the velocity (m/s)
u_n	normal component of the velocity (m/s)
u_t	tangential component of the velocity (m/s)
v	y component of the velocity field (m/s)
V_1	receding velocity of the contact line (m/s)
V_{air}	air flow velocity from the top to the meniscus free surface (m/s)
V_{ev}	mean evaporation velocity (m/s)
α	truncated height (m)
δ	truncated width (m)
δF_p	variation of pinning force
γ	surface tension of water (N/m)
θ_{eff}	effective contact angle
μ	dynamic viscosity of solution $(Pa \cdot s)$
μ_p	dynamic viscosity of polymer solution $(Pa \cdot s)$
μ_c	dynamic viscosity of colloidal suspensions $(Pa \cdot s)$
ϕ_p	volume fraction of solute
$\bar{\phi}_p$	mean volume fraction of solute at boundary 5 (cf figure 4.3
ϕ_{p0}	initial bulk volume fraction of solute
ρ	density of solution (kg/m^3)
ρ_p	solute concentration (kg/m^3)
ρ_s	solvent concentration (kg/m^3)

Notations	Expressions
ρ_p^0	density of pure solute (kg/m^3)
ρ_s^0	density of pure solvent (kg/m^3)
$\bar{V}_{tip}$	the y component of mean velocity at boundary 5 (cf figure 4.3(m/s)

Chapter 1

Introduction

1.1 Motivation

Drying of complex fluid is a common phenomena that happens in our daily life such as stain problems [1], painting works, cosmetics products-related phenomena (nail polish or skin-related drying) and even drying of blood droplets for disease detection [2]. Drying process is also a crucial issue for industrial applications. For **coating process** such as ink-jet printing [3, 4] or printed electronics [5], to avoid the "coffee stain" problems [6] is the key to improve the production rate. Fabrication by **self-assembly technology** of small scale structures for biological materials [7, 8, 9, 10], photonic crystals [11, 12] by drying process will cost less than traditional methods. From the physical point of view, during the drying of complex fluids, complexity comes from the coupling between hydrodynamics, heat and mass transfers and physico-chemical behaviors of the solution and substrate. Several scales are relevant, from the bulk to very thin films such as precusor film are measured to be less than $1\mu m$ [13, 14]. The contact line exhibits complex phenomena while drying, and it plays an important role for the pattern formation of the deposit. Therefore, to understand the fundamental mechanisms of the drying process is our motivation. The goal is to know how the movement of the contact line is related to the deposition thickness, how the hydrodynamics or chemical properties of the solution affect the deposition morphology.

1.2 Background

1.2.1 Sessile droplet drying

Many experiments are carried out on **sessile droplets**, since this geometry is easy to implement. Deegan *et al.* [6, 15] have shown that the accumulation of solute observed on the dried droplet edge was due to contact line pinning and strong evaporation rate at the droplet periphery, which induces a flow from the bulk to the edge (**coffee stain effect**). Snoeijer's group [16] has demonstrated mechanism to form a order-to-disorder transition in the ring-shaped colloidal stain. Different from drying colloids, Smalyukh *et al.* find periodic zigzag shape in the ring-shaped DNA stain and they related the phenomenon in terms of a simple model based on liquid crystal elasticity [17].

A reverse phenomenon (uniform deposit or accumulation in the central zone) can also be obtained by **capillary force** or Marangoni effect. Weon [18] and co-workers found that the capillary force (due to the large size of the particle compare to the height of the droplet which is in the order of $\sim 10\mu m$) can prevail the outward flow due to evaporation and than reverse the flow toward the center of the droplet. Multiple-ring formation in stead of one-ring shape was found in their experiment as a proof. When both large and small particles are used, this results in segregation effect [19, 20].

Marangoni flow is generated by gradient in surface tension which can result from temperature gradient or concentration gradient. Hu and Larson developed a model [21, 22] to describe the effects of Marangoni stresses on the droplet by mean of simplify Navier Stokes equationss and continuity equation. Their solutions show that the heat of vaporization and the nonuniform evaporation rate lead to a nonuniform distribution of temperature along the air-liquid interface and hence a nonuniform surface tension, which drives a thermal Marangoni flow. Experimentally [23, 1] it was found that strong Marangoni flow brings all the particles deposit in the center. This was mainly observed by these authors in organic liquid, and not in water droplet. It is maybe because water is easier to be contaminated by environmental surfactant, which weakens the gradient of surface tension. Then, Xu and Luo [24] used the fluorescence particles to see the Marangoni

flow inside the water droplets. A stagnation point where the surface flow changes directions is observed at the droplet surface. So there exists a maximum value of the surface temperature near the contact line. On another point of view, Ristenpart and coworkers studied the role of substrate thermal conductivity [25]. They found that the direction of the Marangoni flow depends on the relative thermal conductivities of the substrate and liquid and a reversing direction happens at a critical contact angle (31°) over a certain range of the ratio between substrate conductivity and liquid conductivity. Since the flow will redistribute the particles deposition, they suggest the final deposition patterns are significantly affected by Marangoni flow.

Morphologies of final patterns depends on the **process and system parameters** such as the contact angle, particle concentration, evaporation rate, *etc.* The shape of the particle can also determine the flow field and the resulting shapes. Kuncicky *et al.* [26] systematically studied the morphologies of the deposition by varying the substrate wettability (contact angle) and the particle volume fraction. After drying, concave shape is found at low contact angle and low concentration while convex shape is found at high contact angle and high concentration. Leng [27] found that in a confined 2D geometry the deposition (glassy or crystalline) mainly depends on competition of the diffusion of the colloids to the convection induced by the evaporation (local Peclet number). Recently, Yunker *et al.*[28] brought onto play the jamming at the interface observed for anisotropic particles compared to spherical ones. They point out that the ellipsoids particles form easily jammed network on the interface between water and air, so that it can prevent the ring pattern formation and leads to a uniform deposition.

Interactions between particle-particle/particle-substrate will also affect the flow fields and the final patterns. Yan *et al.* [29] found the charge interactions between the particles and the substrate can affect the colloidal crystal growth process and leads to ordered/disordered patterns. Bhardwaj *et al.* [30, 31] found the final deposition depends on the pH values of the solution. They proposed a phase diagram of the patterns (ring patterns, flat deposition, and the transitions) by considering how DLVO interactions modify the flow in the presence of evaporation and Marangoni effect.

1.2.2 Drying in dip-coating-like geometry

The sessile droplet geometry presents several drawbacks: 1. solute concentration and droplet radius continuously change during the drying so that it is a non-steady state and the results are difficult to analyze 2. For applications, droplets are in mm size, long range periodic patterns are difficult to achieve. Another geometry of drying, dip-coating, where a plate is withdrawn from a bath at a given velocity (*or similar systems*) allows the study of steady regimes. Besides, the velocity of the substrate is a independent control parameter that can be defined easily by users. Moreover, it is possible to develop regular patterns in a large area [32] which may have the potential for coating-process casting. The film thickness (h_d) as a function of the substrate velocity V_1 exhibits a "v" shape plot as shown in figure 1.1 (two slopes: -1 and $2/3$). This result has been obtained by different authors and for several different experimental systems [33, 34, 35] including drying polymer solutions or colloidal suspensions. Modelings [36, 37] are also developed to explain this phenomena. The two slopes come from two different mechanisms: for high withdraw velocities, the slope is $2/3$, this is called the dynamic wetting regime or Landau-Levich regime. For low withdraw velocity (slope $\simeq -1$), it is called the evaporative regime which is mainly dominated by evaporation. We give a brief introduction in the following. More details corresponding to our experimental configuration are given in chapter 3.

Landau-Levich regime :

When capillary number is high enough, with $Ca = \frac{V_1 \times \mu}{\gamma}$, V_1 being the substrate velocity, μ and γ are the solution dynamic viscosity and surface tension, the viscous force overcomes the surface tension and entrains a continuous film. The mean thickness of the film is proportional to the withdraw velocity $V^{2/3}$ as shown by Landau-Levich-Derjaguin model. After the study, extended theories and experiments [38, 39, 40] were studied during last few decades.

Evaporative regime:

When the withdraw velocity decreases, one shifts to the evaporative regime. The film thickness is found to linearly decrease as the velocity V_1 increases [34, 33]. The evaporation acts as a pump which drives the solute to deposit. The film thickness can be explained

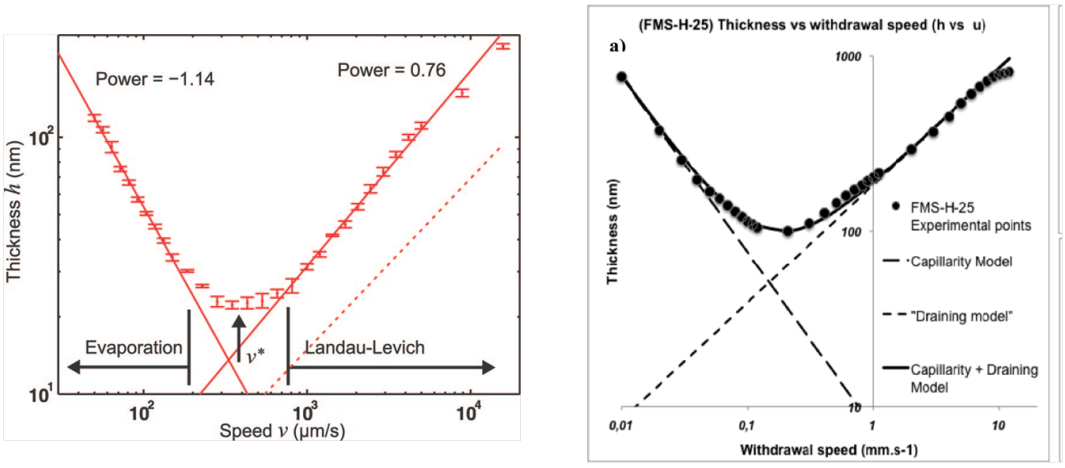

Figure 1.1: Examples of "v" shape curve - deposition thickness versus substrate moving velocity in a dip-coating-like system. Left: Le Berre [34] *et al.* found "v" shape for evaporative regime and Landau-Levich regime by drying phospholipids. Right: Faustini [35] *et al.* found "v" shape by drying sol-gel solutions in a dip-coating system.

by mass balance (detailed explanation will be presented in chapter 3). The film thickness is not affected by the viscosity but depends on the evaporation rate.

Stick-slip regime:

When the withdraw velocity is much lower, it is found that a stick-slip motion of the moving contact line appears and then form periodic deposition patterns. Stick-slip means here that the contact line is pinned or more generally slows down compared to the substrate velocity an then goes a lot faster before pinning again. One remarkable aspect of stick-slip phenomenon or periodic patterns formation are their universality, in the sense that it can be observed for very different systems such as small molecules, colloidal suspensions, polymer solutions in several geometries [43, 44, 45, 34, 46, 47, 41, 48]. Figure 1.2 give two typical examples for the periodic patterns that happen in both dip-coating geometry as well as a sphere-on-flat geometry. Note that even though periodic patterns can be found universally, however from one system to another, this regime is not observed for the same experimental conditions such as substrate velocity, evaporation rate, solute concentration, substrate wettability, etc. Several models tried to explain this phenomena [41, 48, 49],

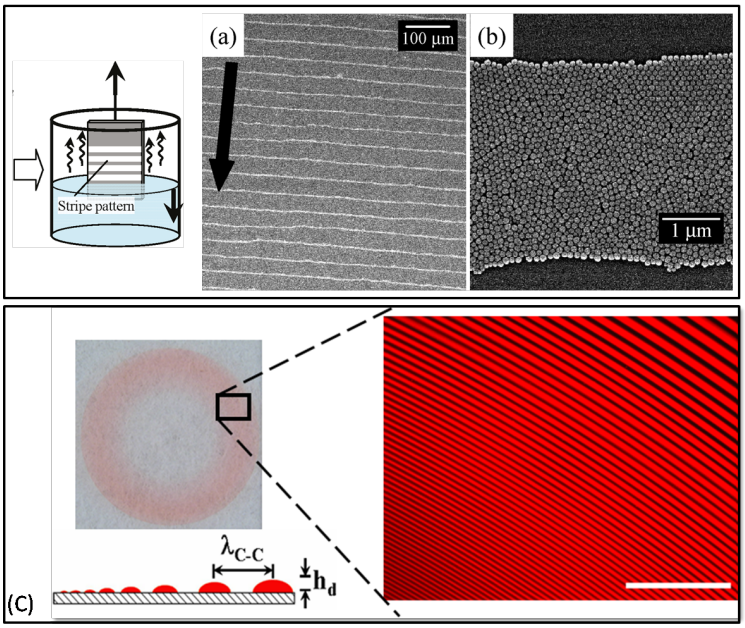

Figure 1.2: Examples of periodic patterns by stick-slip phenomena. (a) and (b): Watanabe *et al.* [41] found periodic stripes deposit on the glass substrate by drying colloidal particles in a dip-coating system. (c): Lin *et al.*[42] found periodic patterns by drying polymer solutions using capillary bridge in a confined geometry, scale bar = $200\mu m$.

but a complete understanding of the driving mechanisms is still missing. While the retraction force which acts to unpin the contact line is often easy to characterize (due to gravity for vertical set-up [48], capillarity for droplets [50, 51]), the physical origin of the pinning force during drying and the onset conditions of a periodic regime are still opened questions.

Simulations have also been performed by several groups [52, 53] taking into account thermal Marangoni effect, vapor diffusion, thermal conduction in the substrate, interaction of particles with the surface. But in most cases a phenomenological criterium for pinning/unpinning is assumed *a priori*, like for instance the minimal value of the receding angle.

Another approaches have been developed for evaporation of very thin films [54, 55, 49]. The authors used a disjoining pressure term taking into account Van der Waals forces, electrostatic forces or structural effects on one hand, and a concentration dependent viscosity on the other hand, to simulate dynamic behavior of thin films. Coupled with film evaporation, these models can predict, for some configurations, periodic movement of the contact line producing surface patterning.

1.3 Context

This manuscript include experimental as well as simulation results. The experimental set-up and solution characteristics are introduced in Chapter 2. Experiments of drying complex fluids (colloidal suspensions/polymer solutions) in a dip-coating-like system at low capillary number are described in Chapter 3. Note that we mainly focus on the stick-slip regime. Thanks to the in line recording of the contact line movement, a quantitative description of the stick-slip motion is obtained for the different systems. Pinning forces, wavelengths, stick and slip and velocities are compared for different pH, as a function of the substrate velocity, evaporation rate, bulk concentration and particle sizes. Empirical laws are deduced from these sets of experiments. A posteriori observations of the dried deposits show important differences in the morphology of the patterns for the different pH.

For polymer solutions drying, some preliminary results are obtained. Stick-slip motion are found only at high temperature, the periodic patterns are different from the the one of colloids. At last, the results are compared with existing models of the literature.

Chapter 4 is dedicated to the simulation of our experiments. A 2D model has been developed to describe the flow inside a Hele-Shaw cell with a non-uniform evaporation which is inspired by our experimental set-up. Deposit is studied as a function of the process parameters (substrate velocity V_1 , evaporation rate V_{ev}) and the solution properties (solute volume fraction ϕ_p, dynamic viscosity μ, diffusion coefficient D). This model is a first step to study mass transfer in a meniscus. We assume a small truncated part at the contact line to eliminate the singularity problem. An iterative procedure is used to define the truncated boundary condition using mass balance. The concentration and velocity fields are calculated by solving Stokes equation and Fick's law. Then, a systematic comparison with a simplified model and experiments are performed.

Finally, we give a conclusion and suggest future works for experiments as well as simulations.

Chapter 2

Experimental system

In this chapter we introduce the experimental set-up and we describe how we measure the evaporation velocity. We present the characteristics of the solutions including the rheology as well as the chemical properties. Finally, we will define the experimental procedure.

2.1 Experimental set-up

This section includes three parts. First, we present the dip-coating-like system which is a home-made design. This design allows to control the evaporation velocity and the contact line speed independently. The second part is the description of the chamber shown in figure 2.1 used for the regulation of the temperature, humidity in order to control the evaporation velocity of the dip-coating-like system. In the third part, we will discuss the observation.

2.1.1 Dip-coating-like system

Figure 2.2 shows the dip-coating-like set-up which is composed of a Hele-Shaw cell and a reservoir. The cell contains two parallel glass slides separated by $1mm$. The small spacers are located at the top of the glass slides and close to the edges. Then, a channel (cf figure 2.3) that brings the air flow is carefully screwed on the top. An air flow from the

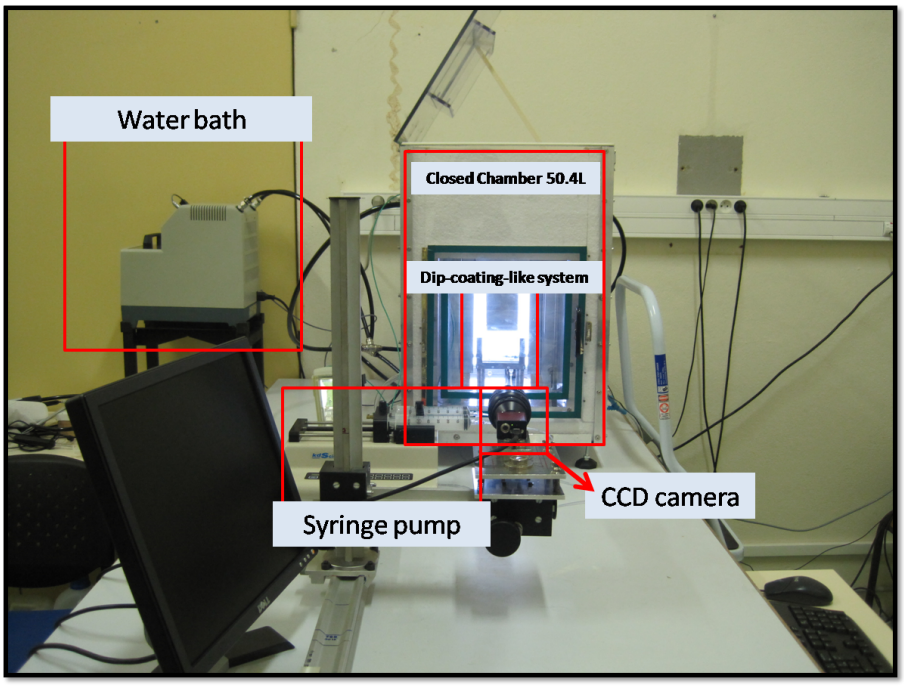

Figure 2.1: Lab picture of the experimental set-up: it contains the **water bath** which controls the temperature, the syringe pump system which controls the movement of the contact line, the CCD camera to record the images and the 60L chamber which used to isolate from outside. The dip-coating-like system is placed inside the chamber.

top of the channel brings the environmental air (in the chamber) to the interface of the meniscus. To control the flow rate, a digital power supply is used to control the voltage of the small fan which is set on the top of the channel. The air flow is set between $0.7m/s$ and $1m/s$ to prevent the deformation of the interface.

A spontaneous capillary rise as shown in figure 2.2 is achieved in between these two glass slides. The glass planar dimensions are $55 \times 80mm$. Parallelism of the glass slides has been verified by measuring the capillary rise height as a function of the contact line position and typical variations are typically on the order of 1%. The planar dimensions of the reservoir are $30.6 \times 85mm$. This is sufficient for the free-surface of the reservoir to reach its infinite position within an accuracy on the order of 1%.

The reservoir is connected to a pumping system (Kd Scientific; Syringe: 60ml Maximum). **Contact line velocity** is controlled by the syringe pump using Labview software. The accessible range of flow rates allows us to explore a contact line velocity range lying between a few nanometers per second up to $2mm/s$.

2.1.2 Evaporation velocity control

Chamber For Regulation

The dip-coating-like set-up is put inside a chamber of volume of 60L, thermally isolated from the room as shown in figure 2.1. Inside the chamber, temperature and humidity are regulated by a PID system. A water bath connected to the heat exchangers which are inside the chamber is set by a feedback loop to regulate the temperature T. It could be raised up to 80°C and down to −5°C. Most of the experiments presented in this study are performed at $25°C$. For humidity Hu, an air flow pumped through either a dessicator or a moisture air is controlled by a feedback loop as well. It can vary from 10% to 90%.

In our system, the evaporation velocity V_{ev} depends on the combination of the temperature, the humidity, the top air flow velocity, and the distance between the meniscus surface and the entrance of air flow. To get an estimation of the evaporation velocity in different configurations, preliminary experiments are performed with pure water. To

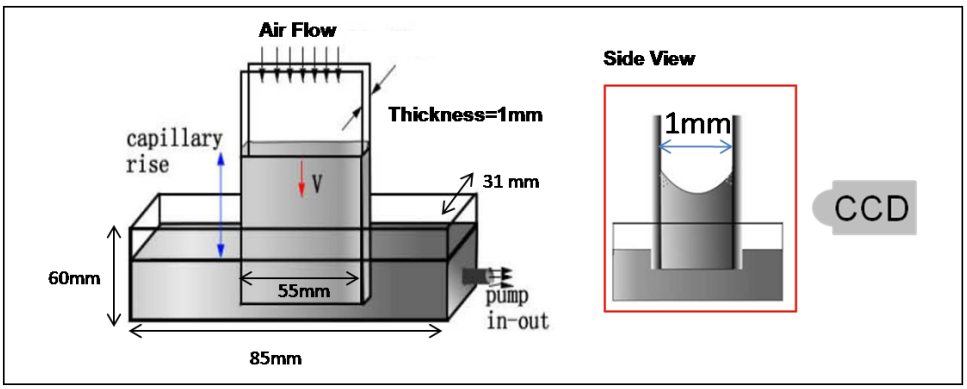

Figure 2.2: Scheme of the experimental set-up. A capillary rise is achieved in between two glass slides immersed in a reservoir. A push-syringe (not shown) is used to empty the reservoir and thus to obtain a displacement of the contact line. An air flow is driven between the glass slides. Side view shows the CCD position which allows to take the image of the capillary rise.

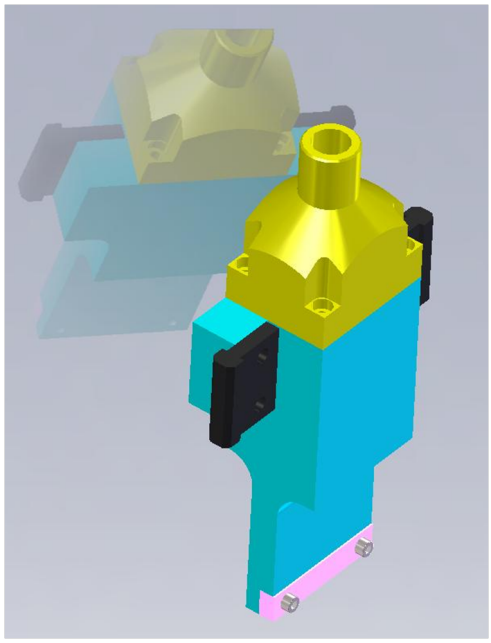

Figure 2.3: Air channel above the dip-coating-like system. All made in aluminium. A fan is hind inside the yellow part. Black are "hooks" for hanging the whole weight on a support. The pink part is used to fix the Hele-Shaw cell.

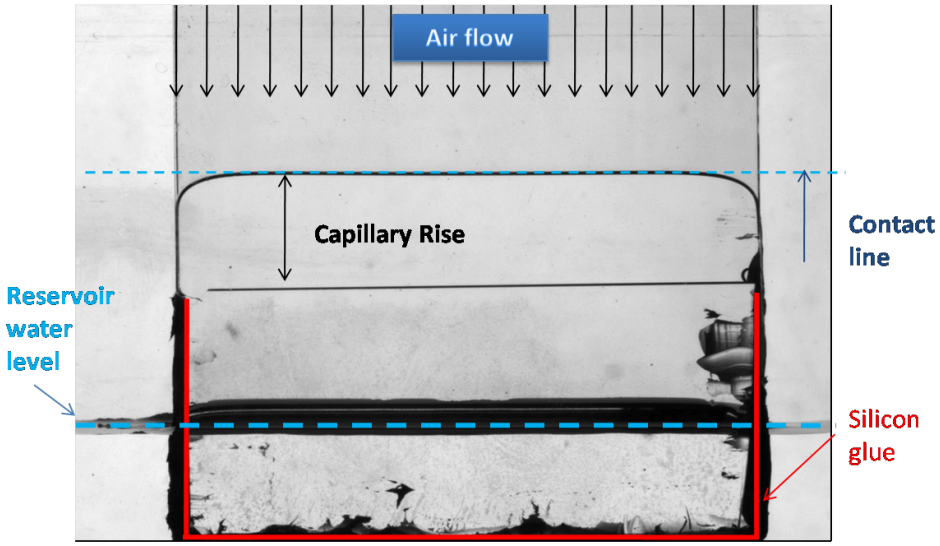

Figure 2.4: The set-up to measure the evaporation velocities. Silicon glue is used to make a close system as shown in red lines. A capillary rise is achieved by first filling water and then pumping out so that there is no connection between the capillary rise and the reservoir. Blue dash is the water level of the reservoir. Evaporation velocity is calculated by recording the contact line movement versus time.

get the evaporation velocity in the same conditions than during the drying experiments, the reservoir is filled with water (same level for every measurement). In order to prevent the fulfilling from the reservoir, a cut between the meniscus and the reservoir is made by silicone glue shown in figure 2.4. Then, we record the receding movement of the contact line to get evaporation velocity, V_{ev}, in the unit of $\mu m/s$.

The highest V_{ev} can reach $3.4\mu m/s$ corresponding to $T = 70°C$ and $Hu = 10\%$, and the lowest V_{ev} is $0.018\mu m/s$ corresponding to $T = 2°C$ and $Hu = 80\%$ as shown in figure 2.5. The leaking due to glue defects can be ignored since at low temperature and high humidity, the evaporation velocity is as low as 10 magnitudes smaller than the case at room temperature, which means that there is no significant leaking in our Hele-Shaw set-up. All the experimental protocol mentioned above is used for the preliminary pure water experiments.

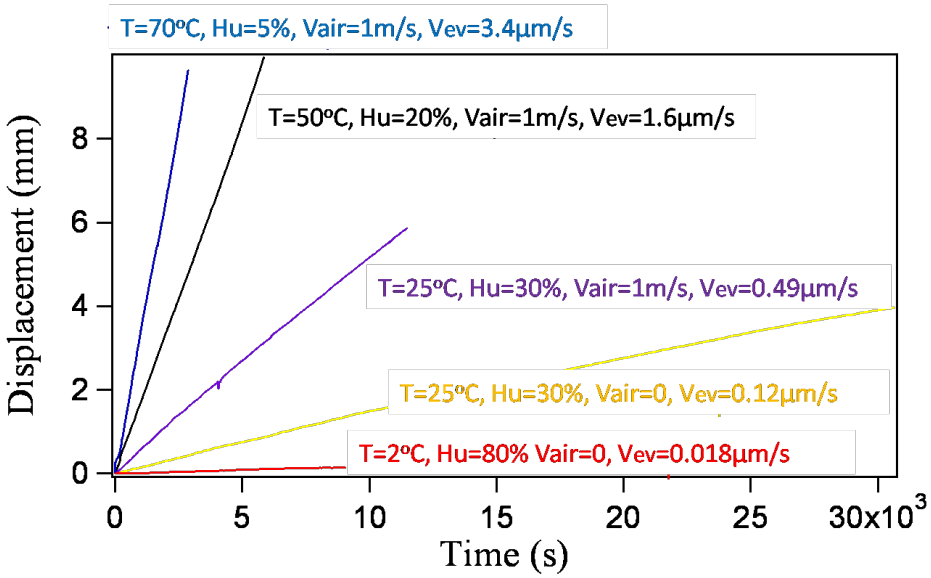

Figure 2.5: Evaporation velocities deduced from recording the movement of the contact line. The straight lines are under different conditions. The highest evaporation velocity shows here is $3.4\mu m/s$. The lowest evaporation velocity is $0.018\mu m/s$.

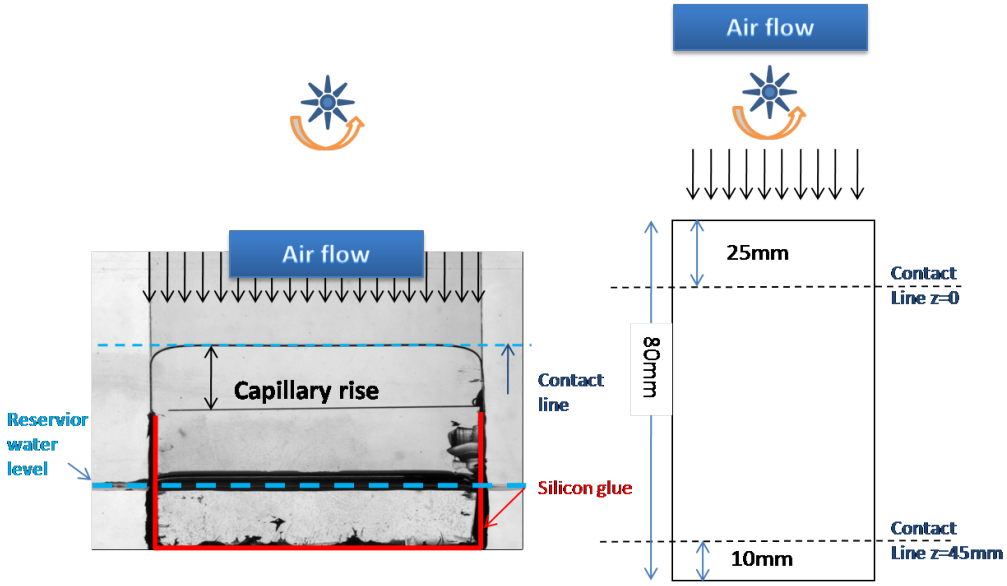

Figure 2.6: Definition of the position z to measure the evaporation velocity. When z=0mm it is closer to the air flow so that the evaporation velocity is higher while lower evaporation velocity is obtained at z=45mm.

Distance effect

The evaporation velocity depends on the distance between the small fan and the free surface of the meniscus. In order to have a more accurate estimation of the evaporation velocity V_{ev}, it is measured for several distances (see figure 2.6 for the definition of "z"). The result is shown in figure 2.7 with conditions: $T = 25°C$, $Hu = 30\%$, $V_{air} = 1m/s$. The highest evaporation velocity $V_{ev} = 0.6\mu m/s$ is at position $z = 0$, while the lowest evaporation velocity $V_{ev} = 0.3\mu m/s$ is twice smaller at the position $z = 45mm$.

Beside room temperature, high evaporation velocity is also tested: $T = 60°C$, $Hu = 10\%$, $V_{air} = 0.8m/s$. The result is shown in figure 2.8. As can be seen there is also a factor of 2 for the highest and lowest evaporation velocities corresponding to the positions (z=5mm-10mm).

In conclusion, there are two evaporation velocities tested in the unit of $\mu m/s$ for V_{ev}

and mm for z:

- Room temperature: $V_{ev}(z) = 0.6 - 0.007z$.
- High temperature: $V_{ev}(z) = 3.03 - 0.041z$.

Reproducibility

In order to test the control of the evaporation velocity, we repeat the same experiment under the same conditions (a fixed distance between the small fan and the free surface of the meniscus, the temperature, the humidity, and the water level). Three cases here are considered:

- $T = 70°C\ Hu = 10\%\ V_{air} = 1m/s$
- $T = 25°C\ Hu = 30\%\ V_{air} = 1m/s$
- $T = 2°C\ Hu = 80\%\ V_{air} = 0.7m/s$

As can be seen in the picture 2.9 for high, middle, and low evaporation velocity, results are similar, which confirms the reproducibility. Note that all the evaporation velocities are tested for $\Delta z < 8mm$, therefore, the distance effect presented in the previous section does not appear.

2.1.3 Observation

A CCD camera (Marlin F201B Allied Vision Technologies) with a lens (AF Micro Nikkor 60 mm f/2.8D) is used for taking the images of the contact line position as shown in picture 2.1. The images are analyzed by IgorPro software. A subpixel analysis is performed, and leads to a precision on the order of $2\mu m$ for the position of the contact line.

A posteriori observation of the dried deposits are performed by optical microscope (morphologies3000), profilometry (3D optical profilometer FOGAL nanotech and NT9100

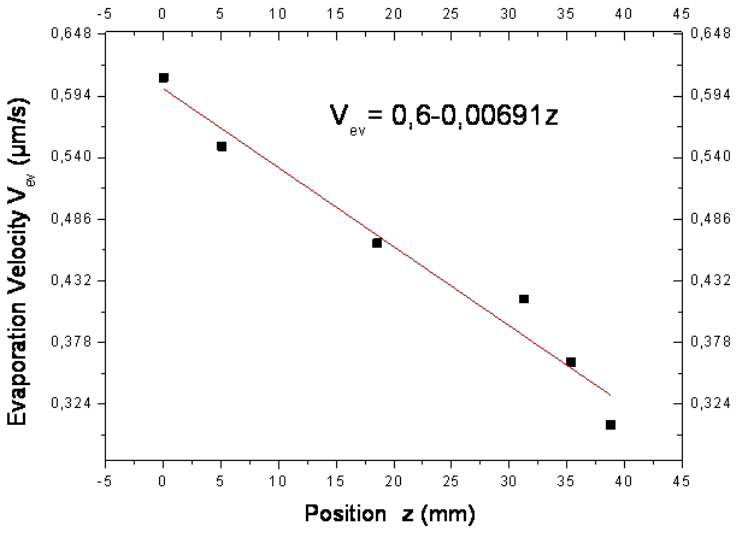

Figure 2.7: Evaporation velocity as a function of the contact line position under conditions: $T = 25°C$, $Hu = 30\%$, $V_{air} = 1m/s$. At room temperature, V_{ev} is between $0.3\mu m/s$ to $0.6\mu m/s$.

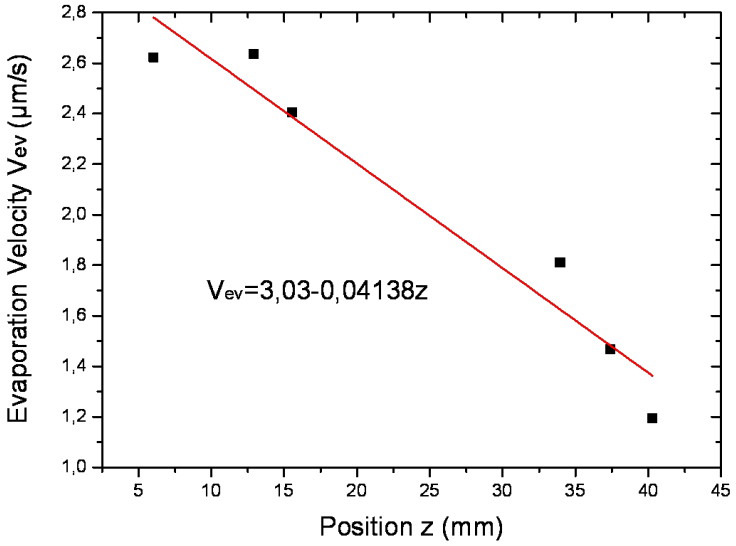

Figure 2.8: Evaporation velocity plot under the condition: $T = 60°C$, $Hu = 10\%$, $V_{air} = 0.8m/s$. At high temperature, V_{ev} is between $1.2\mu m/s$ to $2.6\mu m/s$.

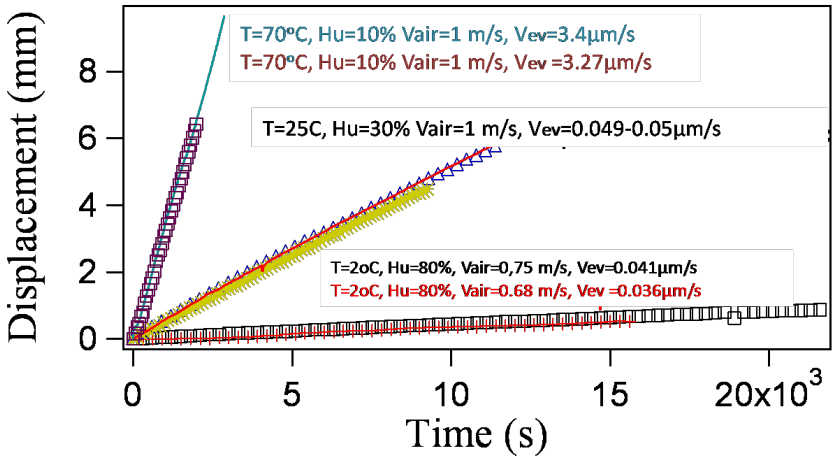

Figure 2.9: Evaporation velocity plot for reproducibility test.

WYKO in Lab PPMD, ESPCI) and AFM microscopy (Veeco dimension 3100 in Lab LPS, UPS).

2.2 Solution Characteristics

In this section, we present the solution characteristics for the silica suspensions and the polymer solution.

2.2.1 Basic information

1. Silica suspension

Commercial suspensions of silica colloidal have been used (50R50, 30R25, 30R12 Klebosol AZElectronic Materials). According to our measurement (density meter and AFM), batch 50R50 is 50% in weight concentration and the particle's mean diameter D_p is $83 \pm 7nm$. Batch 30R25 is 30% in weight concentration with mean diameter of $D_p = 32 \pm 4nm$. Batch 30R12 is 31% in weight concentration with mean diameter of $D_p = 27 \pm 4nm$. A complementary measurement using light scattering equipment for the particle size has

Bench No.	D_p (AFM) (nm)	D_p (LS) (nm)	Weight Concentration	pH value
50R50	83 ± 7	92 ± 9	51.26%	≈pH9
30R25	32 ± 4	32 ± 3	30%	≈pH10
30R12C	27 ± 4	21 ± 6	31%	≈pH10

Figure 2.10: Summary of the silica particle information. The particle size is measured by AFM in Vecco company. The concentration is measured by density meter. LS stands for light scattering equipment (Brookhaven Zeta PALS).

been performed by Carmen Lucia Moraila Martinez using Brookhaven Zeta PALS (Phase Analysis Light Scattering) in Biocolloid and Fluid Physics group in Granada University, Spain. These data are summarized in table 2.10. As can be seen two methods give close results. AFM images are shown in figure 2.11. The silica particle density is 2.208 g/cm^3 measured by density meter (Anton Paar DMA5000).

2.Polymer solutions

We choose polyacrylamide (PAAm) polymer to perform the experiments because it is soluble in water. Two PAAm solutions are used: the low-molar-mass PAAm in water (Sigma-Aldrich 43,494-9) with weight concentration $wt = 50\%$ and molar mass $M_w = 10000 g/mol$. The high-molar-mass PAAm powder (Lot572434, Polysciences Inc.) with molar mass $M_w = 5000000 - 6000000$.

3.pH buffer

DI water is used to prepare the desired pH buffer. pH2 buffer was prepared by diluting Nitric Acid (sigma-aldrich 438073); while Acetic Acid (sigma-aldrich 320099) is used for pH4. The original silica suspension is about pH9. All measurement are done by a pre-calibrated pH meter (HANNA pH209). Note that low values of pH were not accurately estimated, due to some limited detection of our pH meter electrode. Then, we use the notation $pH \simeq 2$ for values between 1 and 2.

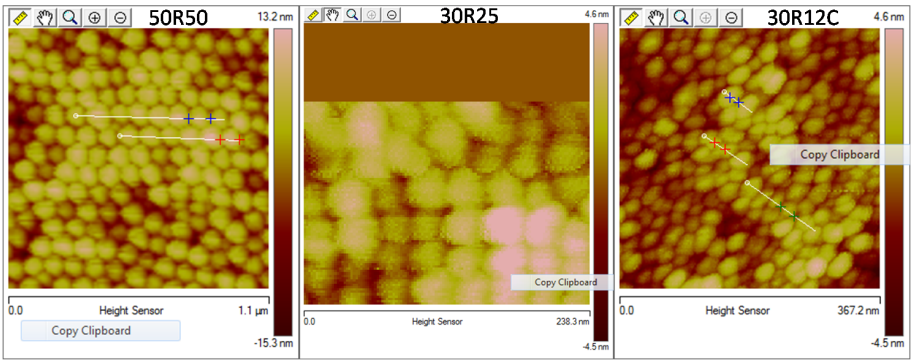

Figure 2.11: AFM images of silica particles.

2.2.2 Ionic Properties

As we use industrial solutions, we have no detailed data of the solution composition, such as the salts composition or concentration (important to stabilize the colloidal suspensions). Therefore, we have not performed a detailed characterization of the electrochemical properties of the suspension. In this section, we just present partial results of conductivity and electrophoretic mobility. A more complete characterization from a macroscopic point of view will be made in the next section, where viscosity as a function of concentration is studied.

1. Electrical conductivity

Electrical conductivity of the solution depends on the ionic composition inside the solution. The value can be used to deduce the Debye length by comparing it with the conductivity of a blank solution (e.g. NaCl) at different concentrations. Hence, we assume that the ionic strength of our suspension is due to an equivalent salt at a given concentration. All data are measured by a pre-cleaned conductivity meter (Microprocessor-pocket-conductivity meter LF69-A/SET) under room temperature ($25°C$).

In our measurement, we found that the sodium chloride (NaCl), 1 $\mu S/cm$ is equivalent to 0.603 mg of NaCl per kg of DI water, which is obtained by linear fitting several measurements as shown in figure 2.12.

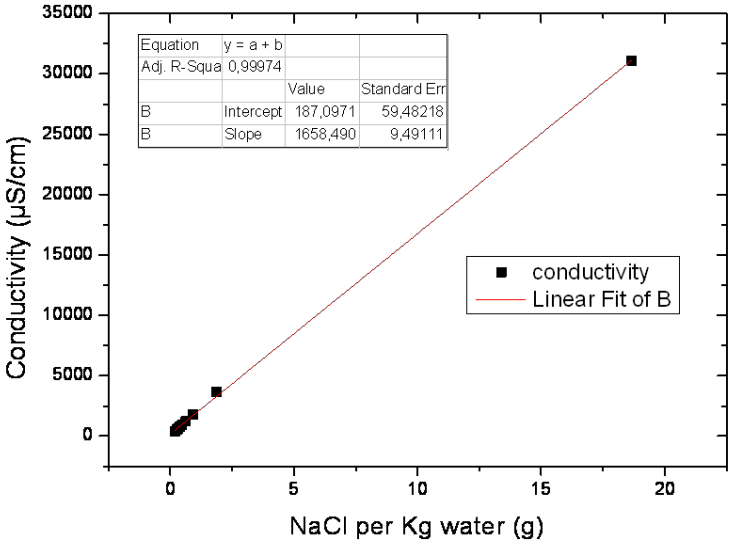

Figure 2.12: Conductivity measurement of NaCl with linear fitting.

2. Debye-Length κ^{-1}

The conductivity of the solution is converted to salt concentration in the unit of molar per liter. To determine the Debye-length of our solutions, we use the equation in SI units (cf appendix A):

$$\kappa^{-1} = 3.055 \times 10^{-10} M^{-0.5} \tag{2.1}$$

where M is the salt molar concentration in mole/liter (NaCl with molar mass=58.44 g/mole was used in our experiment). The results are summarized in the table 2.13. As can be seen the Debye-Length for all the solutions at the initial concentration used in the experiments are in the scale of $1nm$.

3. Electrophoretic mobility

To measure the electrophoretic mobility, silica particles are diluted by different pH buffers. Measurements using Brookhaven Zeta PALS (Phase Analysis Light Scattering) were performed in Biocolloid and Fluid Physics group in Granada University. Figure 2.14 shows

Solution	Volume fraction Φ	Conductivity (µS/cm)	NaCl concentration (M)	Debye Length (nm)
DI water	0%	0.55	5,67505E-06	128
50R50 pH2	8%	2060	0,021255647	~2
50R50 pH4.7	8%	834	0,011205647	~3
50R50 pH9	8%	594	0,006129055	~4
30R12C pH10	1.1%	474	0,004890862	~4
30R12C pH10	4%	1331	0,013733624	~2.6
30R12C pH10	6%	1889	0,019491222	~2

Figure 2.13: Debye Length deduction from conductivity measurements.

the pH effect for both size particles ($\phi = 0.01\%$): the higher pH value the lower electrical mobility.

2.2.3 Viscosity measurement

Changes in electrostatic properties and the particle size is also reflected in macroscopic properties such as the viscosity [56]. We have then performed a systematic study on the viscosity of the suspensions as a function of pH and solute concentration. We regularly measured the suspensions for several volume fraction at room temperature. The steps are:

- Prepare 8% volume fraction colloidal suspension in a open beaker and drying it at room temperature by stirring for 8 hrs.
- Stop stirring and cover the baker by parafilm for 1 to 2 hours to test the solution stability.
- Use syringe to take out 5ml of the solution. 1ml is used for viscosity measurement (Contraves low shear30); 4ml is used for density measurement (Density meter Anton Paar DMA5000).

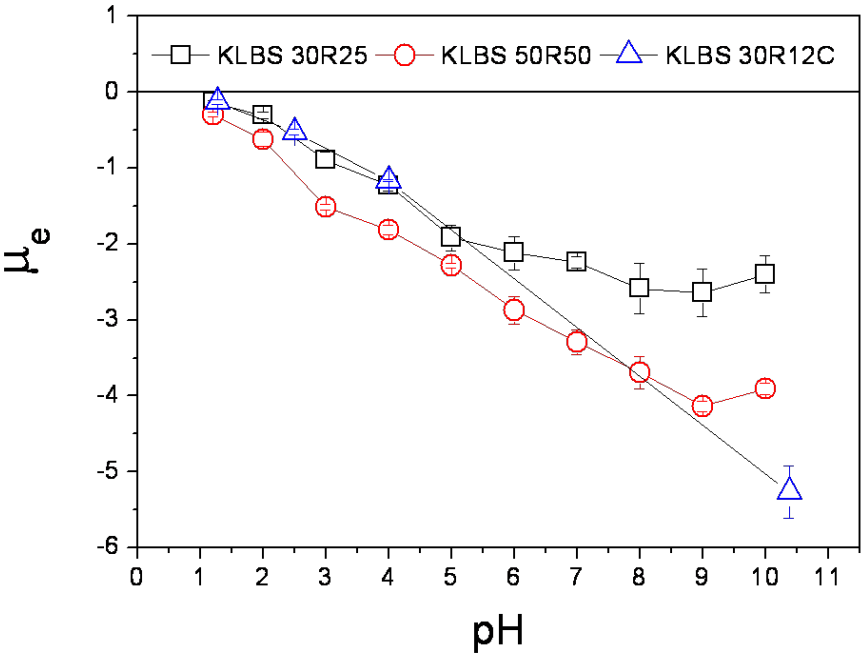

Figure 2.14: Electrophoresis mobility of the colloidal suspension versus the pH value for two different size of particles. Volume concentration is 0.01%.

- repeat step 2 until the solution becomes unstable (phase separation or non-constant viscosity)

The results are plotted in the figure 2.15, each point is averaged by more than 25 measurements. The concentration is convert from density with $\rho_w^0 = 0.998 g/m^3$ for DI water at $25°C$ and $\rho_c^0 = 2.208 g/m^3$ for silica particle. The viscosity variation have been fitted by the Krieger-Dougherty law (cf [57]) which predicts a power dependance with the following expression:

$$\mu = \mu_0 \times (1 - \frac{\phi}{\phi_c})^c \tag{2.2}$$

where μ is the dynamic viscosity of the solution, μ_0 is the dynamic viscosity of the pure solvent ($0.912 mPa \cdot s$ for DI water in our case), ϕ is the volume fraction of the solute and viscosity diverges at ϕ_c. Constant c depends on the characteristics of the solution [58, 59]. It was estimated by data fitting using Matlab (*cftool*). Fitting our data give an exponent c between -1 and -2, and a critical concentration ϕ_c between 0.37 to 0.42.

A summary is shown in table 2.16. The third column is the volume fraction when the suspension starts to become unstable (we found phase separation). These concentrations are consistent to the corresponding ϕ_c. We also report data for PAAm solution which is from our previous study [60]. Note that the viscosity diverges for higher concentration not shown in the figure.

2.3 Experimental procedure

2.3.1 Solution preparation

Colloidal suspensions are stirred for one hour at room temperature before the experiment starts.**Polymer solutions** are stirred for one night at room temperature and filtered by a filter with pore size 200nm (hydrophilic,Lot16532GUK, Sartorius Stedim) just before the experiment. For different pH values (pH2 or pH4), we use pre-prepared pH buffers to dilute the original suspension solution by using micro balance. For pH9 colloidal

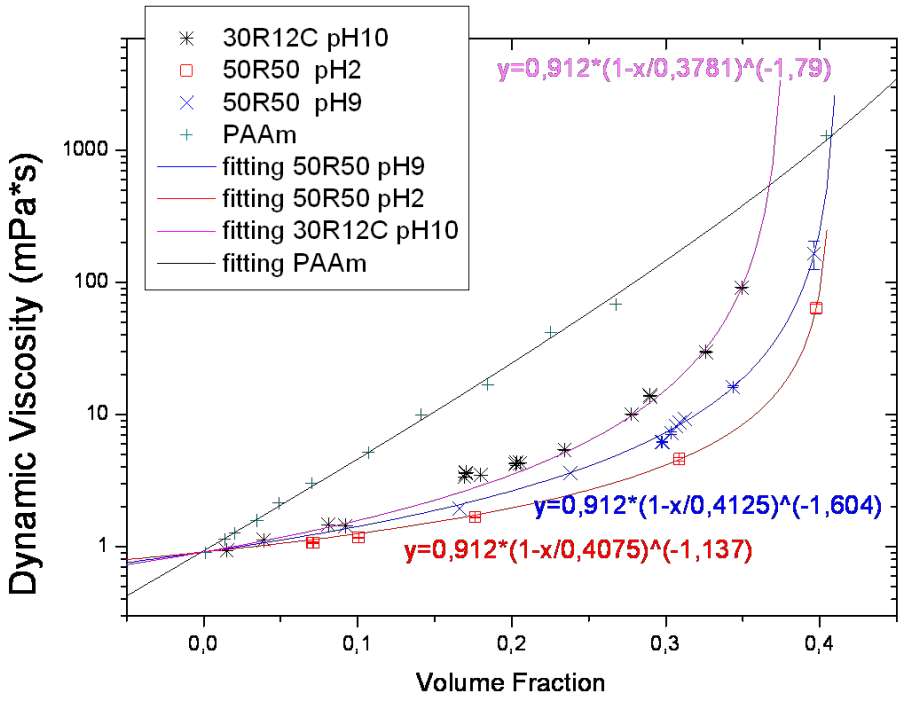

Figure 2.15: Dynamic viscosity of the colloidal suspension and PAAm solution as a function of concentration. Fitting line is done by Matlab.

Suspension Bench No.	Φ_c (fitting value)	C (power)	Unstable Volume Fraction (experimentally)
50R50 (≈pH9)	0.4125	-1.604	0.4036
50R50 (≈pH2)	0.4075	-1.137	0.3977
30R12 (≈pH10)	0.3781	-1.79	0.35

Figure 2.16: Summary of the viscosity fitting.

suspensions, we just dilute it by DI water. Density of the solution will be measured by a density meter (Anto Paar DMA5000) before and after the experiments.

2.3.2 Glass plates cleaning

Glass plates are cleaned by "Piranha" solution (hot mixture of concentrated sulfuric (98%) acid and hydrogen peroxyd (50% water solution), in 70/30 proportions) for at least 20min. They are rinsed by pure water for 2min. Nitrogen flow is used to dry them. At the beginning of the experiment, the receding contact angle is 10° to 15° due to contamination by the environment. In order to ensure that the contact angle remains at similar values for all the experiments, the cleaned glass slides are always used 15 minutes after the cleaning procedure.

2.3.3 Experiments

At the same time when cleaning the glass plates, we set the desired temperature and humidity in the chamber by using the feedback loop controlled by Labview program. The glass substrates are fixed immediately in the dip-coating-like system by carefully screwing just after cleaning. The whole cell is then put inside the chamber. Just before the experiment starts, a small but fast filling out of the reservoir is imposed by manually withdraw the syringes, so that the contact line reaches its receding contact angle. Then, we wait for 10-15 minutes for the system to reach the setting state (Temperature and humidity is controlled by PID system). The movement of the capillary rise is governed through the pumping rate achieved using a pushing syringe. The position of the meniscus that is on the top of the capillary rise is monitored during the experiment by CCD camera outside the chamber.

Chapter 3

Experimental Results and Discussion

We first recall the main results obtained by Bodiguel *et al* [46, 48] and Jing *et al* [33] on a similar set-up. Second, **dynamics of the moving contact line** as well as **pinning force variation** is defined and discussed. Third, **deposition morphologies** such as deposition slopes and shapes are discussed. We provide a detailed study of colloidal suspensions, and first potential results for polymer solutions. Finally we will discuss the existing models for the stick-slip regime.

3.1 Previous results

This study follows previous experiments performed on a similar set-up, using a capillary rise between two vertical plates [46, 48, 33]. The changes between the set-up used during this work and the previous one concern mainly the temperature and humidity regulations, whose accuracy and variation ranges have been significantly improved.

First, we have performed some experiments in the same conditions than the old set-up to check the reproducibility of the results. These tests were conclusive, so that empirical laws and scalings deduced from previous studies will be used to analyze new data. Before presenting experimental results, an important point should be highlighted: for these kind of drying experiments, some dispersion in the results are always observed. Comparison or scaling determination must then rely on numerous experiments to get a meaningful overview of the system behavior.

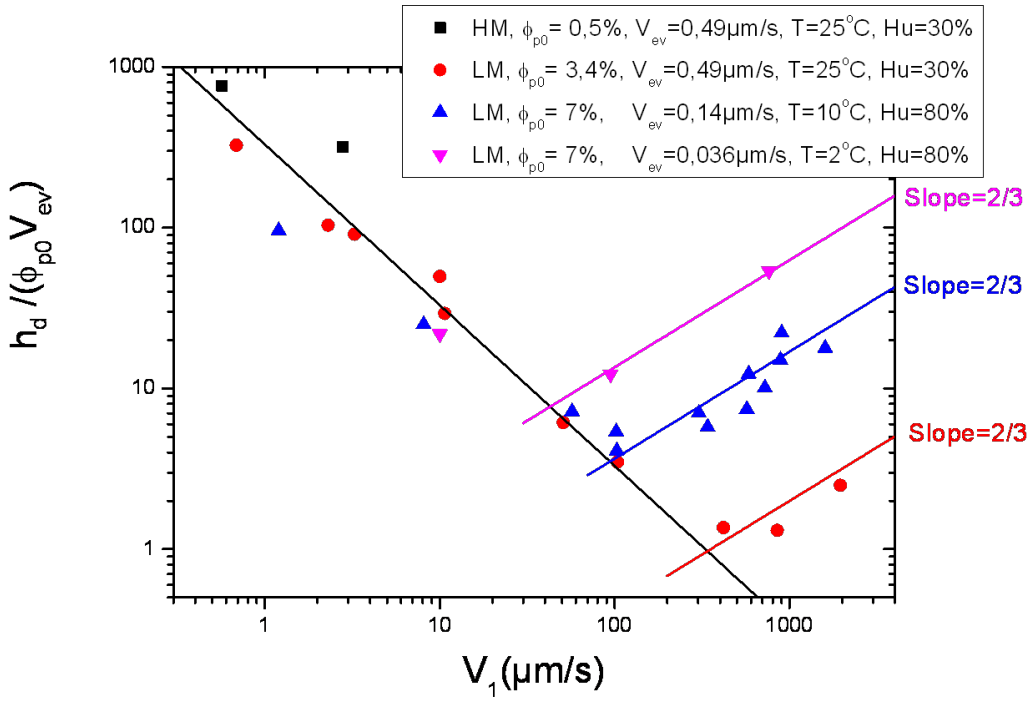

Figure 3.1: "V" shape plot to show the two regimes LLD and Evaporative regime. For PAAm/water solutions, LM: low molar mass; HM: high molar mass. Red line is eq.3.1 The green line is deduced from the LLD theory where the slope = 2/3.

As mentioned in the introduction, several regimes have been identified depending on the capillary number. This leads to a "v" shape plot when the deposit thickness h_d is plotted as a function of the substrate velocity V_1. In the following, a brief review of the previous results is introduced. Experimental results obtained in our set-up with the PAAm solution are presented in figure 3.1. The deposit thickness h_d is obtained by optical profilometry measurement performed on the dried deposit, after having made a scratch with a steel needle to strip the substrate. The mean thickness of the deposit is given by step height measurements, repeated several times at different places and averaged.

3.1.1 Evaporative regime and Landau-Levich regime

Evaporative regime

The evaporative regime is the left part of the "v" shape, at low receding velocities. In this regime, experimental results performed previously on a large range of evaporation rates and initial concentrations [33] have shown that data gather on a master curve (red line), given by:

$$\frac{h_d \times V_1}{\phi_{p0} V_{ev}} = L, \quad with \quad L \simeq 330\mu m \tag{3.1}$$

This empirical law can also be deduced from a simple model based on mass balances in the meniscus. It will be described in detail in chapter 4 dedicated to simulation. The main idea of this simple model is that evaporation at the free surface of the meniscus is the driving mechanism. It acts as "a pump" that brings solute to the meniscus edge. As can be seen in figure 3.1, new data obtained with the PAAm solution are in agreement with equation 3.1, which confirms the similarity of the old and new set-up.

Landau-Levich regime

The Landau-Levich regime corresponds to the right part of the "v" shape. This is also called dynamic wetting regime. There viscous forces are large enough to drag a film from the bath. The thickness of the dragged film can be estimated by adapting the Landau law to our confined geometry:

$$h = 0.67\ d\ Ca^{2/3}, \tag{3.2}$$

where d is the distance between the two glass plates.

One can assume that the final deposit corresponds to the drying of the dragged film ($h_d = \Phi_0 h$) and then the thickness of the deposit is expected to increase with the velocity at power 2/3, as confirmed by various experimental results in the literature (cf [61, 34]), and by figure 3.1.

Note that the thickness in this regime depends on the Capillary number, and then on the viscosity which changes as a function of the initial concentration and temperature.

The velocity V_1 corresponding to the intersection of the two lines is given by $V_1^{5/3} \simeq 0.5V_{ev}(\gamma/\eta)^{2/3}$. The transition is shifted to the left when the viscosity increases and the evaporation flux decreases, which explains that the transition for experiments performed at high concentration and low temperature ($\Phi_{p0} = 0.07$ and $T = 2°C$) occurs at about $40\mu m/s$, while the transition velocity is about ten times larger for $\Phi_p = 0.034$ and $T = 25°C$.

3.1.2 Stick-slip regime

When the contact line velocity is very small, the coating may be no longer continuous but may form periodic stripes. The movement of the contact line becomes pinning-unpinning cycles. We focus now on this regime which is described in details in the end of chapter 3.

3.2 Dynamics of the contact line

In this section we first present the tools we have developed to analyze the contact line movement during the stick-slip regime. Results about **pH effect** and **size effect** on the pinning force and wavelengths are presented for the colloidal suspensions. Then, preliminary results are given for the polymer solution.

3.2.1 Definitions

The contact line movement is recorded by CCD camera from a side view of the meniscus (cf figure 2.2). By image processing, the contact line displacement versus time can be plotted. Figure 3.2 (a) shows a typical example of a periodic motion. Stick-slip motion is defined as following: stick means that the contact line slows down compared to the mean velocity (red lines) and slip means that it accelerates (purple lines). For the two stages (stick and slip), we can deduce the length dh_i, duration τ_i and velocity V_i from the observation of the contact line displacement. Definitions are straightforward from the

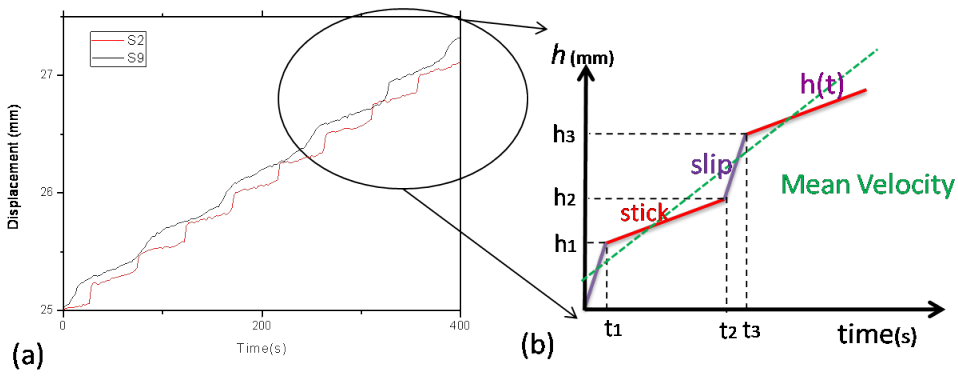

Figure 3.2: Typical examples of the contact line movement versus time. The experimental parameters are: $V_1 = 5\mu m/s$, $V_{ev} = 0.4\mu m/s$, $\phi_{p0} = 8\%$. Only pH values are different. S2 stands for $pH \simeq 2$ and S9 stands for $pH \simeq 9$. t_1, t_2, t_3 are arbitrary times corresponding to h_1,h_2,and h_3 positions.

diagram drawn in figure 3.2 (b).

$$dh_{total} = h_3 - h_1, \quad dh_{stick} = h_2 - h_1, \quad dh_{slip} = h_3 - h_2$$
$$\tau_{stick} = t_2 - t_1, \quad \tau_{slip} = t_3 - t_2, \quad V_{stick} = \frac{h_2 - h_1}{t_2 - t_1}, \quad V_{slip} = \frac{h_3 - h_2}{t_3 - t_2} \tag{3.3}$$

3.2.2 Variation of the pinning force

For experiments performed with pure water and with a constant pumping rate, the contact line displacement is a straight line: $h_W(t) = V_1 t$, with $h_W(t)$ the distance from the initial capillary rise before pumping and V_1 the velocity imposed by the pumping rate. Deviations from the linear variation observed during the stick-slip correspond to a modification of the contact angle, due to an interaction between the contact line and the deposit that is formed on the glass substrate. The corresponding pinning force can be estimated from the weight of the water corresponding to this deviation, that is for one side of the substrate and neglecting the change in meniscus shape (cf figure 3.3):

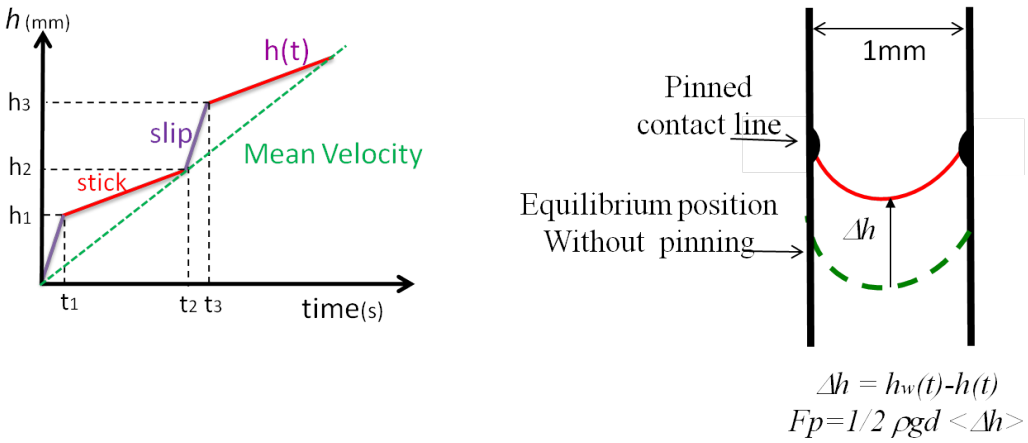

Figure 3.3: Sketch for pinning force F_p. ρ is solution density, d is the gap width (1mm), g is gravity.

$$F_p = \frac{1}{2}\rho g d(h_W(t) - h(t)) \tag{3.4}$$

It is implicitly supposed here and in the following that the pinning force which is in principle a local quantity is constant along the contact line. Thus the problem could be in a first approximation considered as two-dimensional. This assumption is consistent with experimental observations that always show patterns parallel to the contact line.

During an experiment performed with a colloidal suspension, we have no access to the equilibrium pure water capillary rise $h_W(t)$. However, we may estimate the variation of the pinning force from the end of the stick stage ($t = t_2$, just before unpinning, where the pinning force is maximum) and the end of the slip stage ($t = t_3$, just before pinning again):

$$\delta F_p = \frac{1}{2}\rho g d[h(t_3) - h(t_2) - V_1.(t_3 - t_2)] = \frac{1}{2}\rho g d[dh_{slip} - V_1\tau_{slip}] \tag{3.5}$$

Numerical estimation of δF_p is made by assuming that the velocity V_1 corresponding to the pure water experiment is close to the mean velocity obtained with the colloidal

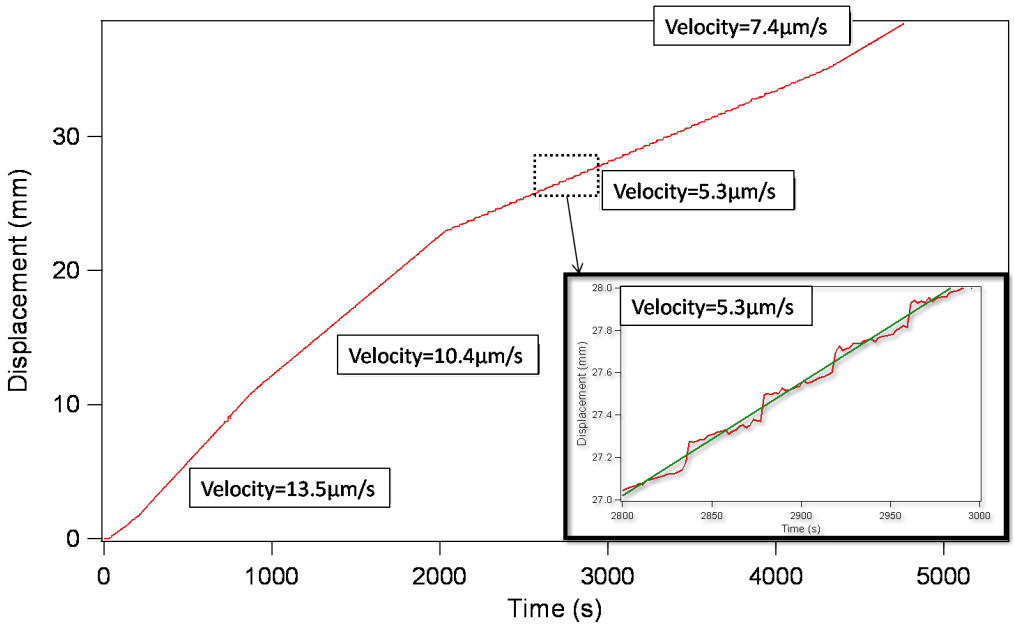

Figure 3.4: Example of the displacement of the contact line versus time. There are 4 imposed velocities under the experimental conditions: $T = 25°C$, $Hu = 30\%$, colloidal suspension volume fraction is 8%. The inset is a zoom on a small portion of the displacement when $V_1 = 5.3\mu m/s$, showing the periodic deviations (in red) of the contact line from the mean velocity (in green).

suspension and deduced from the average motion of the contact line (cf figure 3.3).

3.2.3 Data analysis

A systematic method has been developed to analyze the dynamic of the contact line. One example (displacement versus the time of the contact line movement) is illustrated in figure 3.4. For this set of experiments (1.5 hours), 4 different velocities are imposed by the pumping system. The velocities $(13.5, 10.4, 5.3, 7.4\mu m/s)$ are obtained by linear fit of the displacement versus time. It is called **mean velocity** V_1, as shown in the inset in figure 3.4 in green. In order to quantify the periodic behavior, a substraction $h'(t) = h(t) - V_1 \times t$ is performed as shown in figure 3.5. The sawtooth-shaped curve

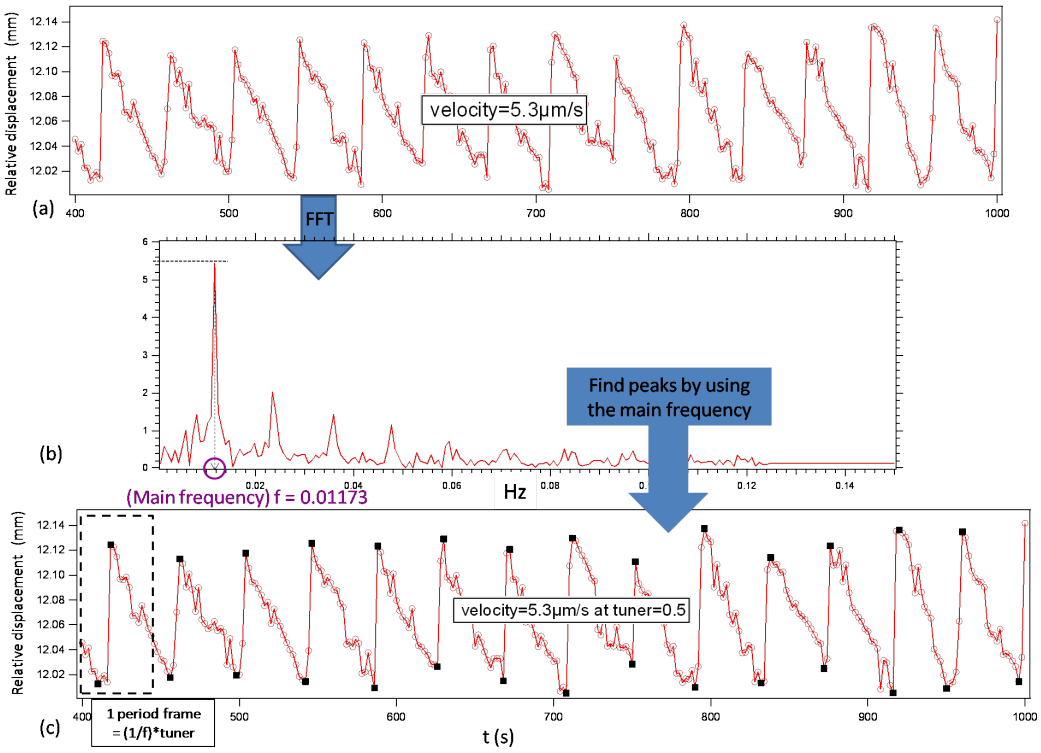

Figure 3.5: Example of pinning force variation measurement. (a) relative displacement (deduced from a substraction from original displacement versus time as shown in figure 3.4. (b) To get the periodic behavior we use FFT to get the main frequency f (1 period frame $=1/f\times$tuner). This is then used to locate the peaks as shown in black dots in (c). Experimental conditions: $T = 25°C$, $Hu = 30\%$, colloidal suspension volume fraction is 8%, $V_1 = 5.3\mu m/s$, S2 solution. (Note that since V_1 is a mean value, the ordinate is known $\pm$ a constant. In the following, only difference of peaks are used.)

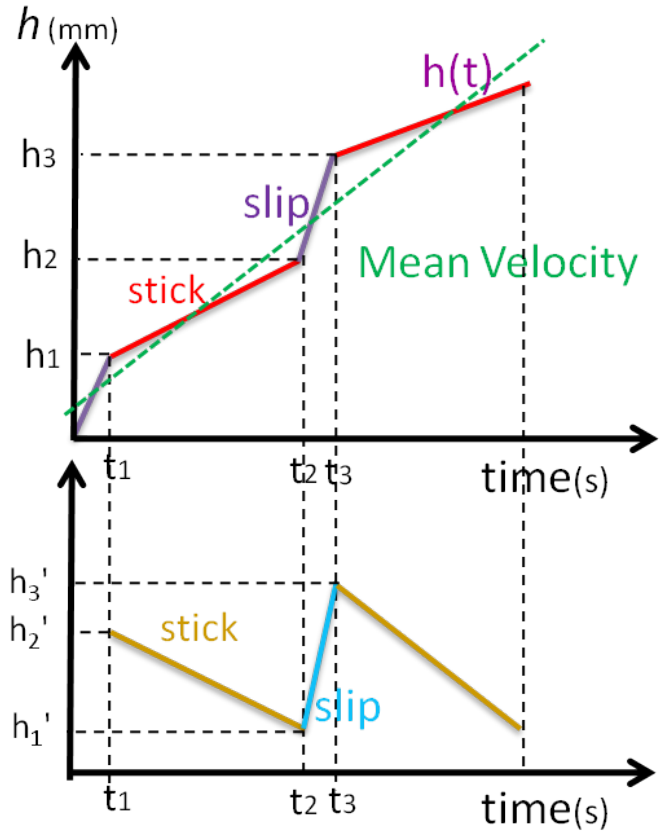

Figure 3.6: Sketch to show the relative displacement $h'(t) = h(t) - V_1 \times t$.

shows clear periodic behavior of the stick-slip motion. Using Fast Fourier Transform (FFT), the main frequency f is estimated and then used to find the corresponding peaks without taking into account secondary extrema. The procedure is the following:

- Start for instance from a maximum $h'(t)$ which is found in the first period interval $[0, t_p]$ with $t_p = 1/f$. Suppose the maximum value is h'_{max1} at $t = t_{max1}$.
- Then, the minimum h'_{min1} is located in the interval $[t_{max1}, t_{max1} + t_p]$.
- Then, second maximum h'_{max2} is found in the interval $[t_{min1}, t_{min1} + t_p]$.

- Then, the same procedure is repeated using the period t_p, and all the peaks are located.

Sometimes, the main peak found in FFT corresponds to 2 oscillations instead of 1. In that case, a correction factor of 0.5 is manually applied to the period (tuner=0.5 shown in figure 3.5 (c)).

Peaks give the information of the periodic behavior, including dh, τ and $V_{stick/slip}$ defined in equations 3.3, explained in the following: (cf figure 3.6).

$$
\begin{aligned}
h'(t_2) &= h(t_2) - V_1 \times t_2 \,, && \text{(3.6a)}\\
h'(t_1) &= h(t_1) - V_1 \times t_1 \,, && \text{(3.6b)}\\
dh_{stick} &= h(t_2) - h(t_1) \,, && \text{(3.6c)}\\
&= h'(t_2) - h'(t_1) - V_1 \times (t_2 - t_1) \,,\\
&= V'_{stick} \times (t_2 - t_1) - V_1 \times (t_2 - t_1) \,,\\
&= (V'_{stick} - V_1) \times (t_2 - t_1) \,,\\
&= V_{stick} \times \tau_{stick}
\end{aligned}
$$

Since $h'(t) = h(t) - V_1 \times t$, we get the first two equations. V_1 is known by linear fitting, V'_{stick} and τ_{stick} are obtained from the peak information. Note that the absolute value of $h'(t)$ (figure 3.5) is not important, the important information is the difference between the absolute values. The same deduction can be used for slip part.

When the velocity increases ($V_1 > 12\mu m/s$), we no more observe periodic patterns but a flat film with small undulations. A typical example for $V_1 = 16.8\mu m/s$ where stick-slip motion starts to disappear is shown in figure 3.7 and 3.8. This kind of data is not taken into account for our analysis of the stick-slip motion, since the wavy motion is too small compared to our image processing resolution (around $10\mu m$). The peaks obtained by the procedure described above have no meaning.

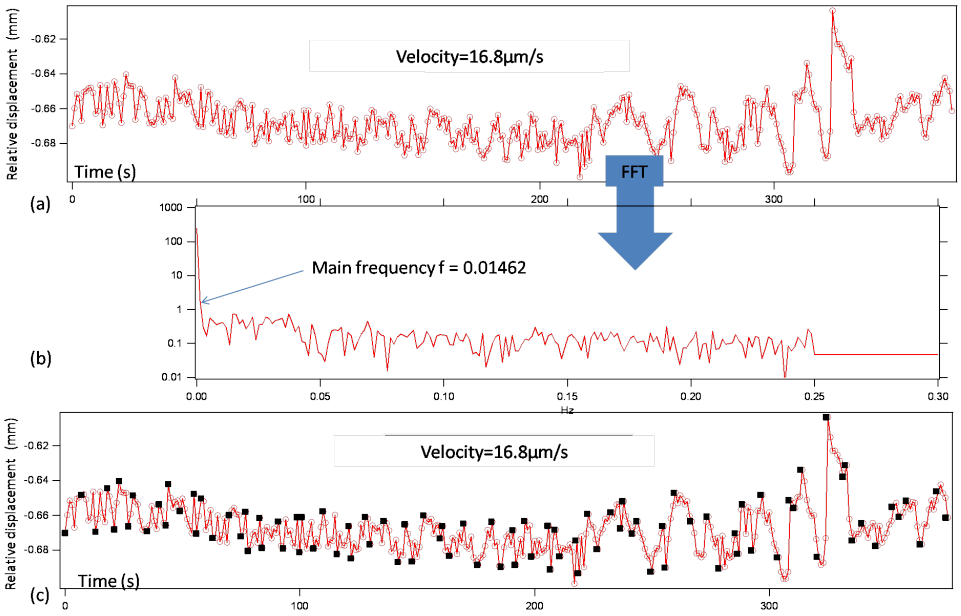

Figure 3.7: Example of pinning force variation measurement at high velocity $V_1 = 16.8\mu m/s$. (a) Relative displacement. (b) FFT gives the main frequency. (c) Illustration of configuration where peaks determination failed. Experimental conditions: $T = 25°C$, $Hu = 30\%$, colloidal suspension volume fraction is 8%, $V_1 = 16.8\mu m/s$, S9 solution.

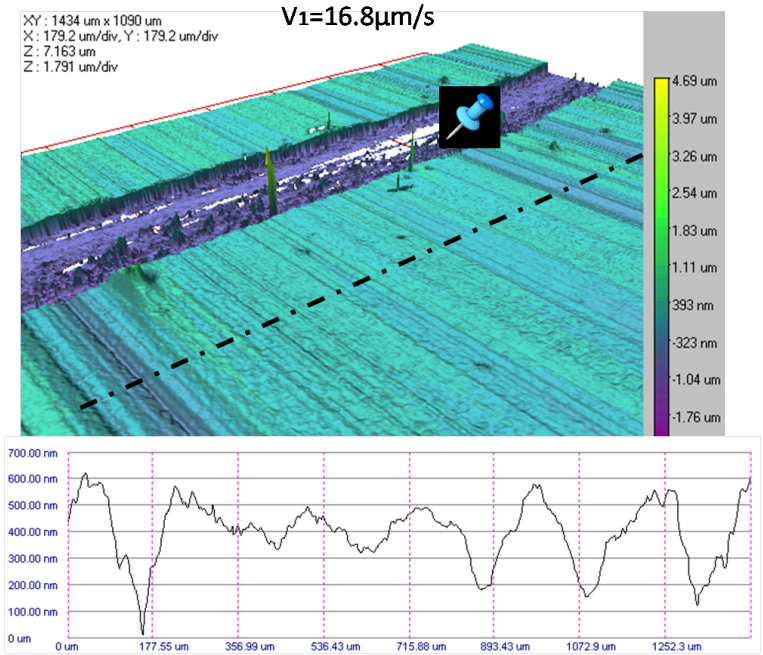

Figure 3.8: 3D image from profilometer corresponding to the experiment shown above. The amplitude of the non-uniform undulation is around $0.4\mu m$ while the film thickness is about $2\mu m$. An artificial gap cut by a needle is performed to measure the film thickness.

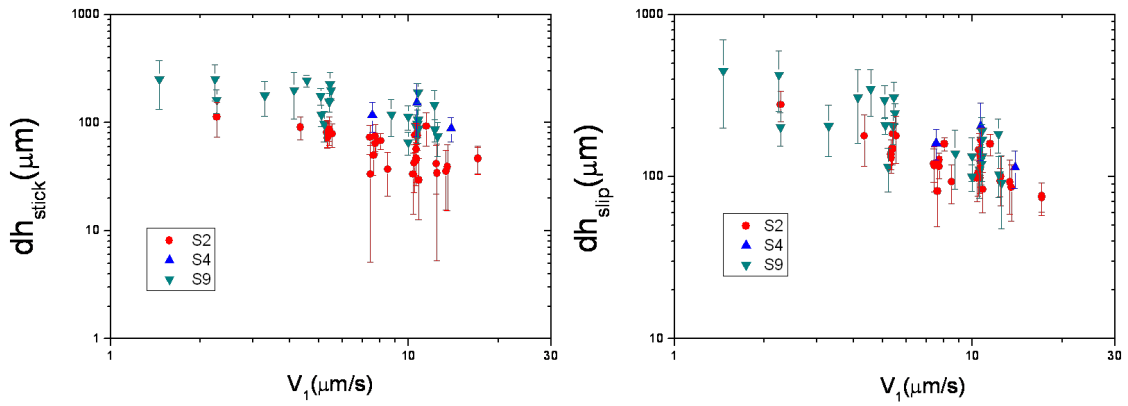

Figure 3.9: Stick (left) and slip (right) lengths for S_9, S_4 and S_2 suspensions.

In conclusion, once stick-slip motion clearly appears, stick-slip can be easily analyzed. The values (dh, τ and $V_{stick/slip}$) can be obtained by the relative values of the peaks $h'(t_i)$. To deduce the pinning force, equation 3.5 is used. The final value(s) are averaged over more than 10 periods which are shown in the following results as an error bar (standard deviation). All data processing are made with IgorPro.

3.2.4 Results for colloidal suspension

The results for colloidal suspensions include two parts, first we analyze the pH effect on the dynamic of the contact line and the pinning force variation δF_p. Second, we tested two sizes of silica particles, we will compare the results for the pinning force variation and the total wavelength.

pH effect

We first focus on the effect of variation of the ionic properties of the solution on the pinning forces and wavelength, for the 83nm particles. Figure 3.9, 3.10, and 3.11 give the results obtained for all the experiments performed with S2($pH \simeq 2$), S4($pH \simeq 4$),

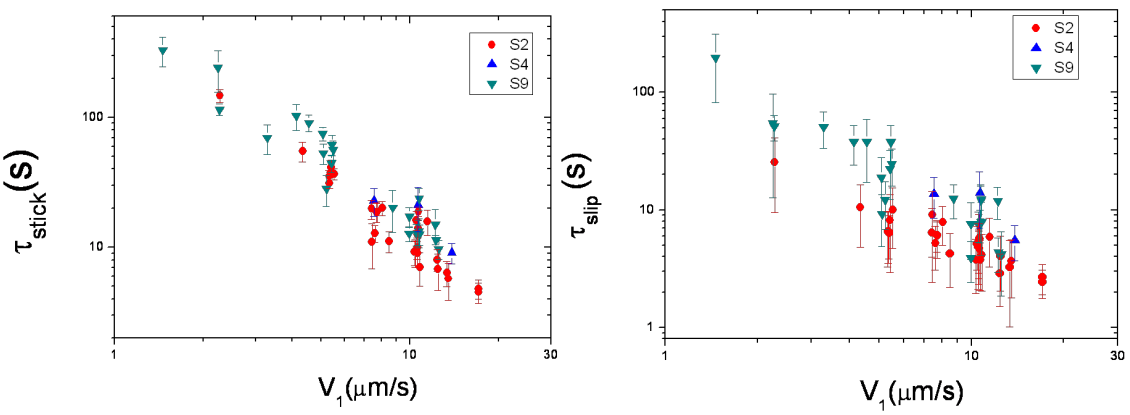

Figure 3.10: Stick (left) and slip (right) period for S_9, S_4 and S_2 suspensions.

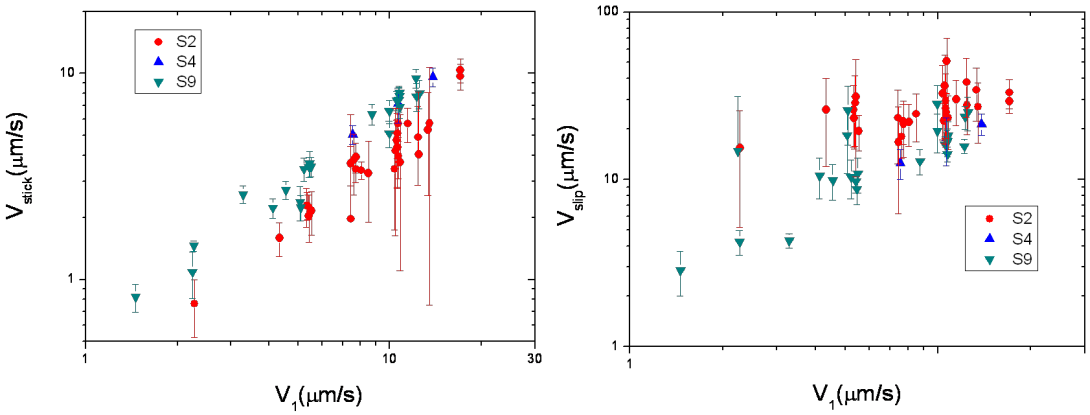

Figure 3.11: Stick (left) and slip (right) velocity for S_9, S_4 and S_2 suspensions.

S9($pH \simeq 9$) colloidal suspensions. The conditions are:

- Initial volume fraction $\phi_{p0} = 8\%$.
- Evaporation velocity: $0.3\mu m/s < V_{ev} < 0.6\mu m/s$.
- Imposed velocity: $1\mu m/s < V_1 < 20\mu m/s$.

Pinning Force Variation

It is worthwhile to compare the results obtained here with previous experiments performed at pH $\simeq$ 9, and covering a large range of initial volume fraction and evaporation rate. Empirical scaling was obtained for the pinning force, that reads [46, 48] :

$$\frac{\delta F_p}{\gamma} = 1.4 \frac{\phi_{p0} V_{ev}}{V_1} \tag{3.7}$$

where γ is the water surface tension. As can be seen in figure 3.12, no significant difference is observed for δF_p among the three suspensions S_2, S_4, and S_9. Except for the dispersion of the results, all the data gather on the same master curve given by eq. (3.7). Indeed, as stated in section 3.5, δF_p is given by $dh_{slip} - V\tau_{slip}$. dh_{slip} and τ_{slip} are both smaller for low pH (cf figure 3.9 and 3.10 right) and it appears that these two quantities compensate each other.

Wavelength

We have tested the same scaling for the wavelength. As shown in figure 3.13, the same scaling holds for the wavelengths $dh_{total} \simeq C \times \phi \frac{v_{\mathrm{evap}}}{V_1}$ with $C \simeq 74mm$. Experiments performed at pH $\simeq$ 9 (S_9 solutions) compare well with wavelengths deduced from previous experiments [48] with the same pH. No significant difference is observed with S_4 suspensions while the drying of S_2 leads to roughly two times smaller wavelengths: using the same scaling for S_2 points, we get $C \simeq 44mm$. A microscope view that illustrates the difference in wavelength is shown in 3.15. By observing the contact line movement with more detail (cf figure 3.14), it can be seen that both the stick and slip lengths contribute to the decreasing of the wavelength. Let us note that, for a given experiment, the wavelength distribution (corresponding to error bar) is much narrower than in Shmuylovich

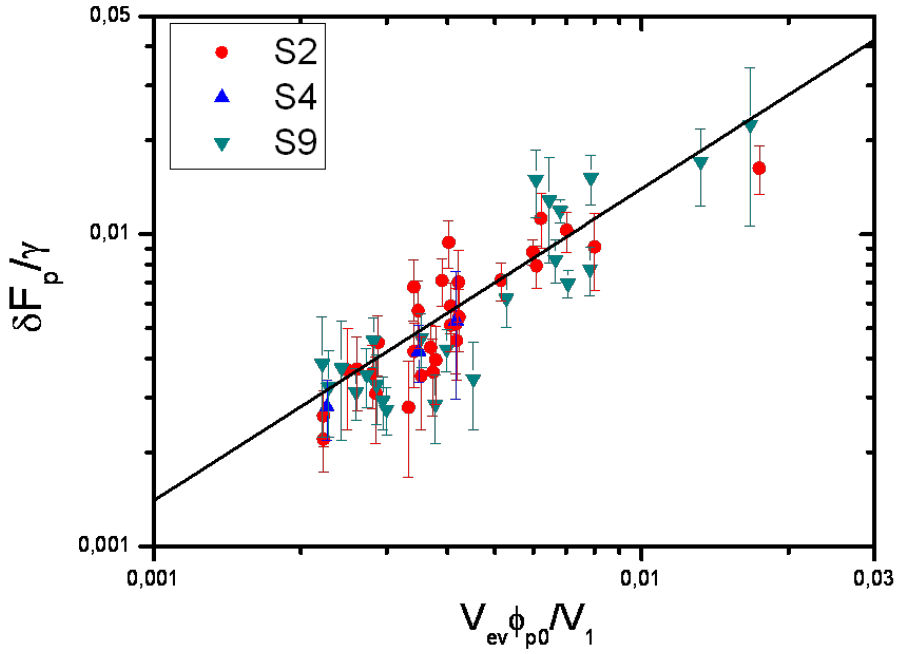

Figure 3.12: Variation of the pinning force for the three suspensions S_9, S_4 and S_2. $\gamma = 72mN/m$ is the water surface tension at 25^oC. The solid line is the empirical scaling law suggested by Bodiguel *et al.* [46, 48].

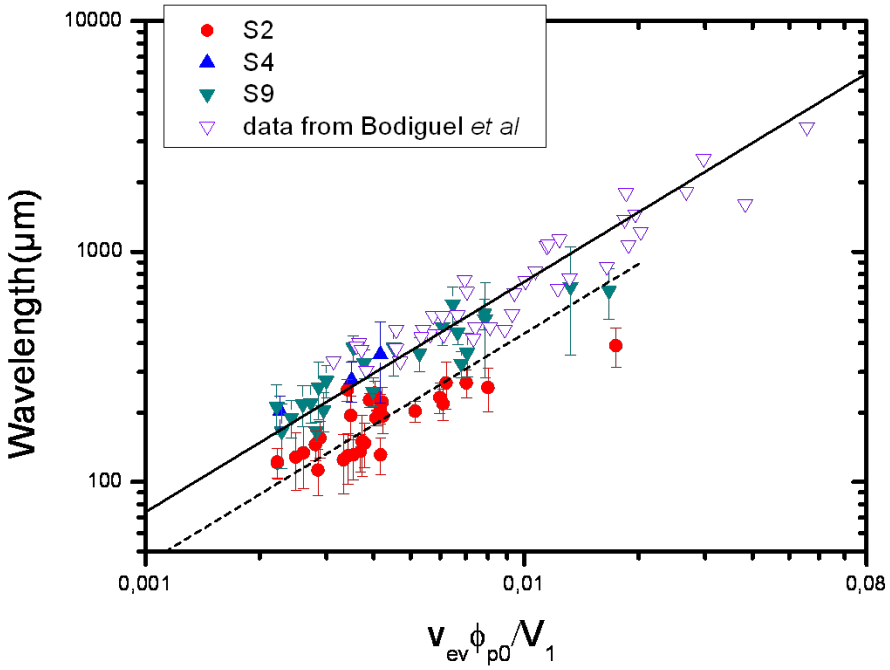

Figure 3.13: Wavelength for S_9, S_4 and S_2 suspensions and hollow triangle is the data from Bodiguel *et al* [46, 48]. The solid straight line is a fitting of S_9, S_4, and Bodiguel' data (prefactor $74mm$). The dash line is a fitting of S_2 data.

et al. experiments performed on sessile droplets [62]. These authors related the large distribution they observed to the stochastic contact line movement which pinned again when it encounters a particle that has previously adhered to the substrate. Obviously the geometry used here (dip-coating instead of droplets) and/or carefully cleaned substrates significantly decrease the stochastic aspect of the stick-slip. Lin et al [42] observed that the use of an exceptionally clean and homogeneous substrate (cleaved mica sheets) enhanced uniformity of the patterns.

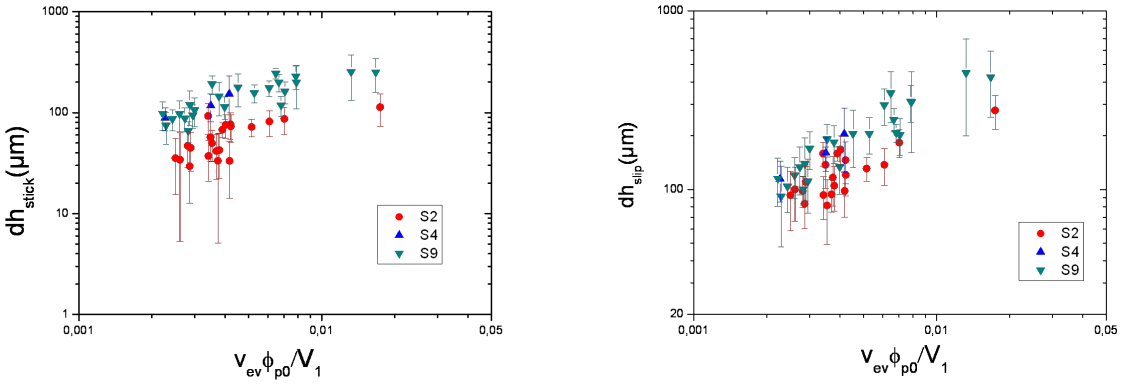

Figure 3.14: Stick (left) and slip (right) lengths for S_9, S_4 and S_2 suspensions.

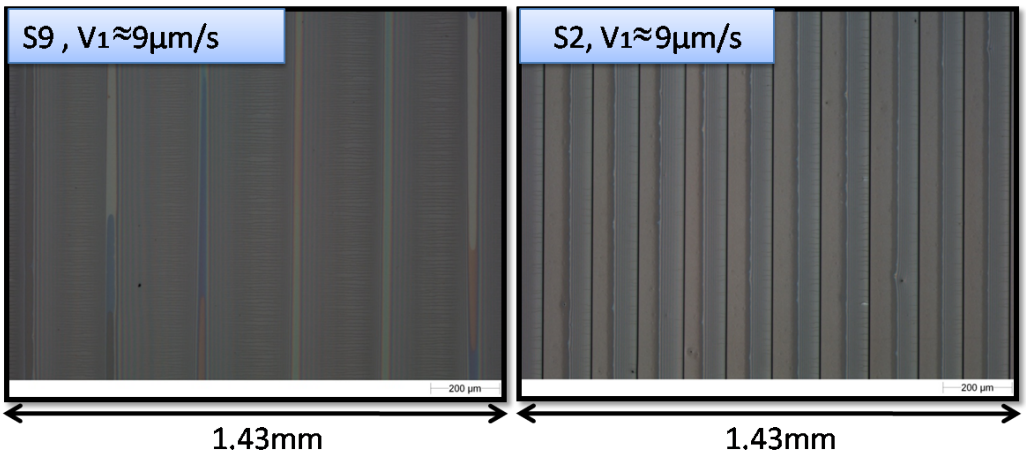

Figure 3.15: Microscope views: wavelength comparison for S_9 and S_2 solutions. Condition parameters: $V = 9\mu m/s$, $v_{ev} = 0.4\mu m/s$, $\phi_{p0} = 8\%$.

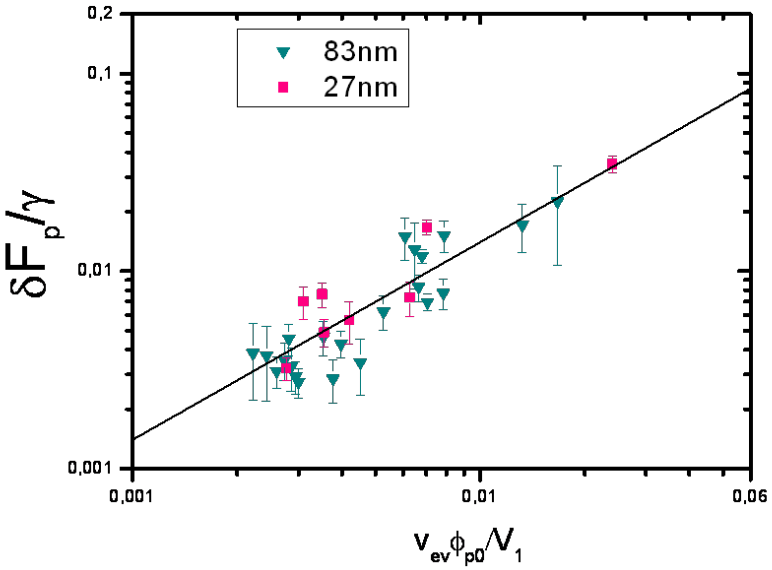

Figure 3.16: Variation of the pinning force at high pH, for two particles sizes. $\gamma = 72mN/m$ is the water surface tension at 25^oC. The solid line is the empirical scaling law reported by Bodiguel and co-author [46, 48].

Size effect

In a second set of experiments, two particle sizes are tested for the pinning force measurement: $D_p = 83nm$ for S9 and $D_p = 27nm$ for pH10. For smaller particles, the deposition is more brittle and then detaches from the substrate. Several parameters were tried to get well-patterned depositions: volume fraction is varied from 1.2% to 6% and speed is varied from $1\mu m/s$ to $7\mu m/s$. The results are shown in figure 3.16 and 3.17 for pinning force and wavelengths respectively. As can be seen, there is no significant size effect on the wavelengths or pinning force variation. Other results such as dh_{stick},dh_{slip}, the ratio of two velocities are shown in appendix B.

As a conclusion of these experiments, it appears that δF_p, the variation of pinning force between the unpinning and the beginning of the successive new pinning, is quite independent on the two parameters studied here, particle sizes and solution pH. On the

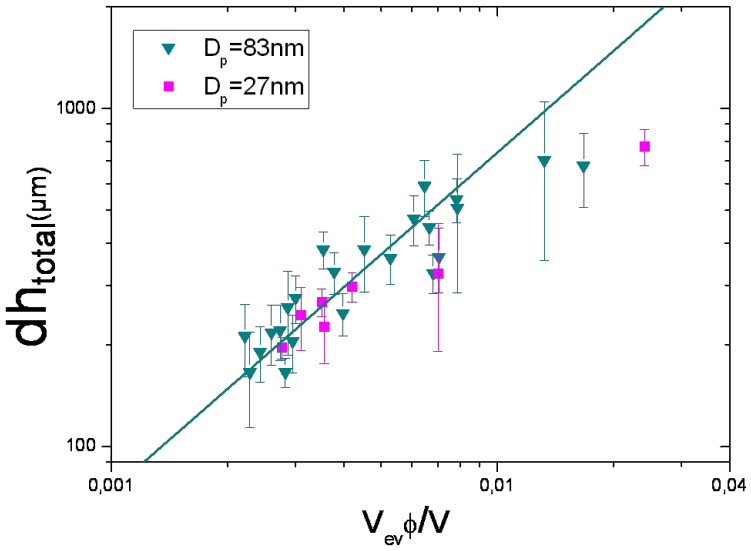

Figure 3.17: Wavelength for $83nm$ and $27nm$ particle suspensions. Solid line: power law with exponent 1 and prefector $= 74mm$.

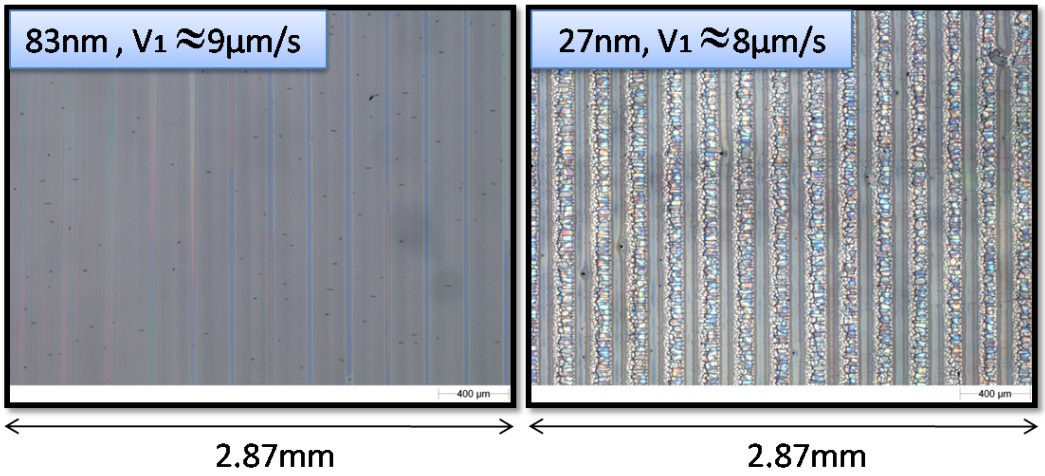

Figure 3.18: Microscopic View for big particle and small particle comparison. Experimental conditions bigger particle: $V_1 = 9\mu m/s$, $V_{ev} = 0.35\mu m/s$, $\phi_{p0} = 8\%$, smaller particle: $V_1 = 7.8\mu m/s$, $V_{ev} = 0.33\mu m/s$, $\phi_{p0} = 6\%$.

PAAm Volume Fraction	3.4% (LM)			1.35%(LM)			1.3%(LM)			1.3%(HM)		
	V1(µm/s)	Vev(µm/s)	StickSlip	V1(µm/s)	Vev(µm/s)	StickSlip	V1(µm/s)	Vev(µm/s)	StickSlip	V1(µm/s)	Vev(µm/s)	StickSlip
Low V_{ev} 25°C	10.4	0.45	N	10.3	0.49	N	5.5	0.27	N	1.2	0.46	Y*
	6.0	0.28	N	6.0	0.37	N	10.4	0.35	N	7.2	0.40	N
	1.2	0.23	N	1.2	0.26	Y*	1.2	0.44	N	0.32	0.34	N
High V_{ev} 60°C	2.0	2.69	Y	3.2	1.8	N	5.7	3.0	N	Bubble formation (probably due to outgassing)		
	3.4	1.93	N									
	4.1	3.22	Y	1.5	2.3	N	10.7	2.5	N			
	1.9	2.67	Y									
	1.76	2.0	N	4.7	2.9	N	1.7	2.2	N			
	5.0	1.92	N									

Figure 3.19: Table to summarize the experimental conditions and results using PAAm/water solutions. "Y" indicates that the stick-slip phenomena can be observed. "N" indicates that the stick-slip phenomena is not observed. "Y*" means the reproducibility has to be confirmed.

contrary, wavelengths depend on solution pH values.

3.2.5 Results for polymer solutions

We present in this subsection the first results obtained with a polymer solution (PAAm in water. Two molar mass are used: $M_w = 10000 g/mol$ (LM) and $M_w = 5000000 - 6000000$ (HM). We did not observe stick-slip at room temperature except for very low velocities and low concentrations. But results are difficult to analyze. Then our objective is first to determine the experimental conditions where stick-slip can be found and analyzed.

Several concentrations (0.5% to 5% mass fraction) at different evaporation velocities are tested. The results are shown in table 3.19. The receding velocity V_1 are tested from $1\mu m/s$ to $10\mu m/s$. Low evaporation rate corresponds to $T = 25°C$, $Hu = 30\%$ so that V_{ev} is between $0.3\mu m/s$ to $0.6\mu m/s$. The high evaporation rate corresponds to $T = 60°C$, $Hu = 10\%$ so that V_{ev} is between $1.3\mu m/s$ to $2.6\mu m/s$. N stands for NO stick-slip motion. We now determine the pinning force and the wavelength for the stick-slip configurations.

As described in equation (3.7) the power law for colloidal suspensions has a pre-factor

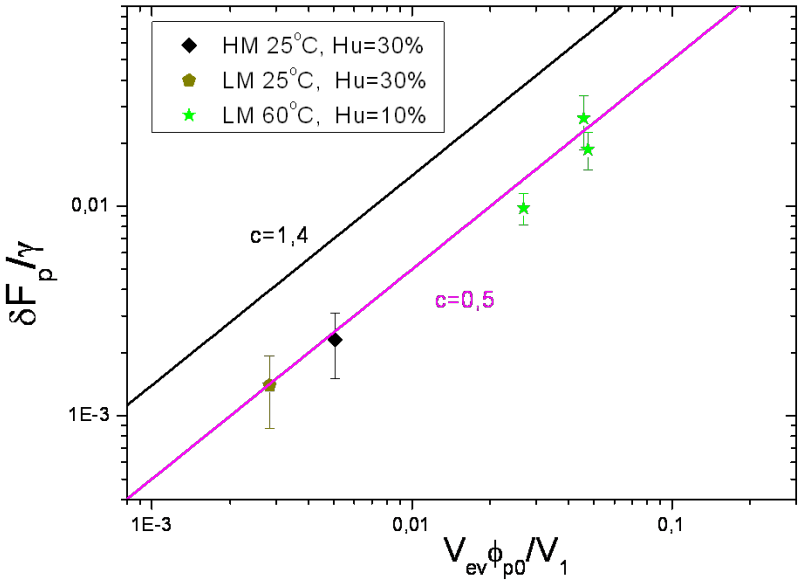

Figure 3.20: Pinning force variation for polymer solutions. Black solid line: fitting from colloidal suspensions' results.

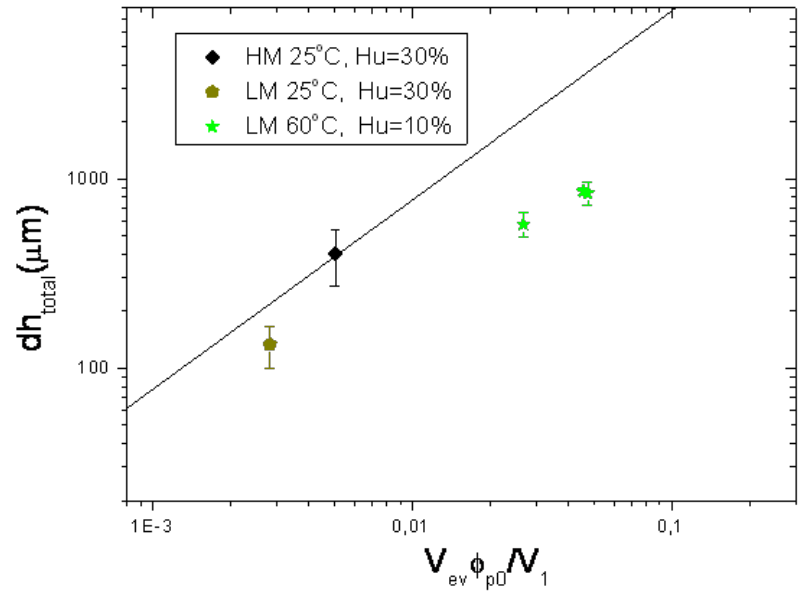

Figure 3.21: Wavelength for polymer solutions. Solid line has a prefector $74mm$ deduced from colloidal suspensions' results.

1.4. In figure 3.20 we plot the variation of the pinning force for polymer solutions. Though we have only a few results, it seems that the prefactor is about 3 times lower compare to the colloidal suspensions. We also plot the wavelength dh_{total} shown in figure 3.21. The solid line is the previous fitting of colloidal suspensions (cf figure 3.13). As can be seen, there is a significant decrease of dh_{total} for polymer solutions. However, more experiments should be made to confirm these first results.

Summary

To conclude this section, we quantified the dynamics of the contact line movement such as the total wavelength dh_{total}. We also defined the pinning force variation, and related it to the pH effect and size effect for colloidal suspensions. We found lower pH value suspensions will have lower wavelength and it may due to the lower viscosity. However, there is no strong pH effect or size effect for the pinning force variation.

On the other hand, stick-slip motion of polymer solutions is observed at high evaporation velocities ($60°C$). The variation of pinning force and the wavelength dh_{total} are found lower than the values of colloidal suspensions. This is only first results, which need more investigation in the future.

3.3 Morphologies of depositions

Apart from these quantities deduced from the measurement of the contact line displacement, direct observations of the dried deposit have been performed with microscope, AFM or optical profilometer for a few samples, to get the wavelength, shape and height of the deposits.

3.3.1 Results for colloidal suspensions

In this part, all the results are obtained with silica particles ($D_p = 83nm$) at different pH values. Note that deposits obtained from smaller particles ($D_p = 27nm$) could not be analyzed due to crack and delamination problems. Two parameters of the morphology

are going to be discussed: first, the slope of the deposit in the side where unpinning takes place. Second, the amplitude which is defined as the distance between the highest and the lowest point of the height profile.

1. Downward slope α

The downward slope α corresponds to slip side (the contact line movement is toward left) as shown in figure 3.22. As can be seen, the profile is much sharper for S2 solution. We measured the angle for S9 by profilometer and the sharp angle for S2 using AFM as shown in figure 3.23. The slopes for S2 are one order of magnitude higher than the ones for S9 as shown in figure 3.24, this is because the slip process goes faster as mentioned in the last section. In order to relate it to the contact line movement, we plot also the ratio of the slip velocity and stick velocity. This ratio is larger for S2 suspensions than S9/S4 suspensions as shown in figure 3.25.

2. Amplitude

The amplitude is defined as the difference between the maximal and minimum heights of the deposit. A 3D picture of two pH depositions are compared in figure 3.26($V_1 = 12\mu m/s$, $V_{ev} = 0.39\mu m/s$ $\phi_{p0} = 8\%$). We observe that longer wavelengths and more symmetric deposit for S_9 suspensions. We manually measure the amplitude for 3 pH values at different velocities as shown in figure 3.27. We found that there is no significant pH effect on the amplitude of the depositions.

In conclusion of these part, an illustration of the strong influence of the ionic properties of the suspension on the deposit morphology is given by observing the wavelength and the slope of the deposition. For S2, the deposit is asymmetric and the transition is much sharper at one side, but the amplitude of the three solutions (S2, S4 and S9) are similar.

3.3.2 Results for polymer solutions

We performed the same analysis for a few points where stick-slip was observed with PAAm solutions. In figure 3.28 we show an example to illustrate the amplitude of the

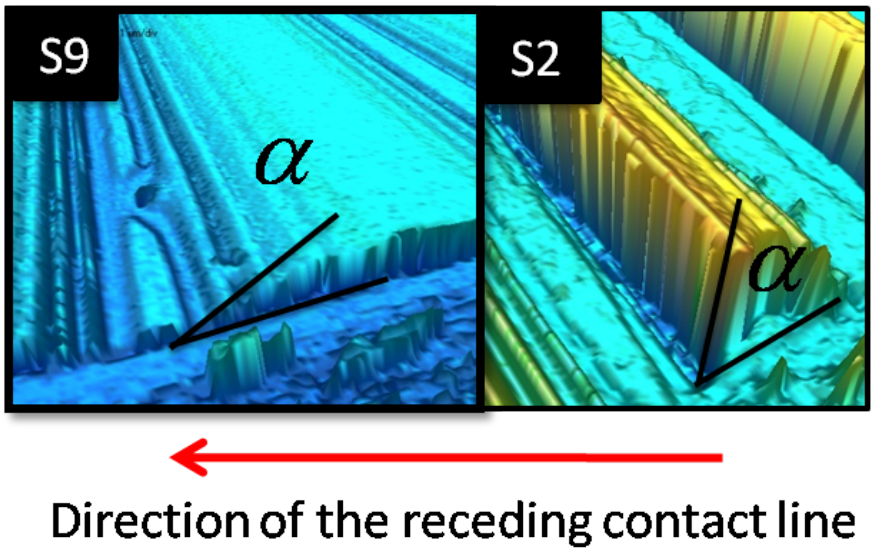

Figure 3.22: Example of slopes obtained after drying of S_9 and S_2.

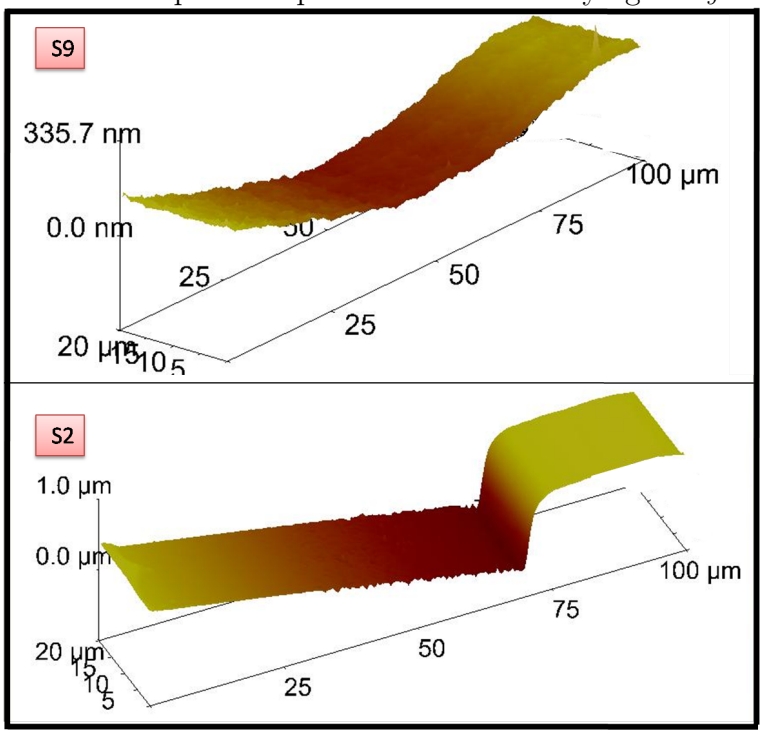

Figure 3.23: AFM images for S9 and S2. Experimental conditions: $V_1 = 12\mu m/s$, $\phi_{p0} = 8\%$, $V_{ev} = 0.4\mu m/s$. The contact line moves toward left of the picture.

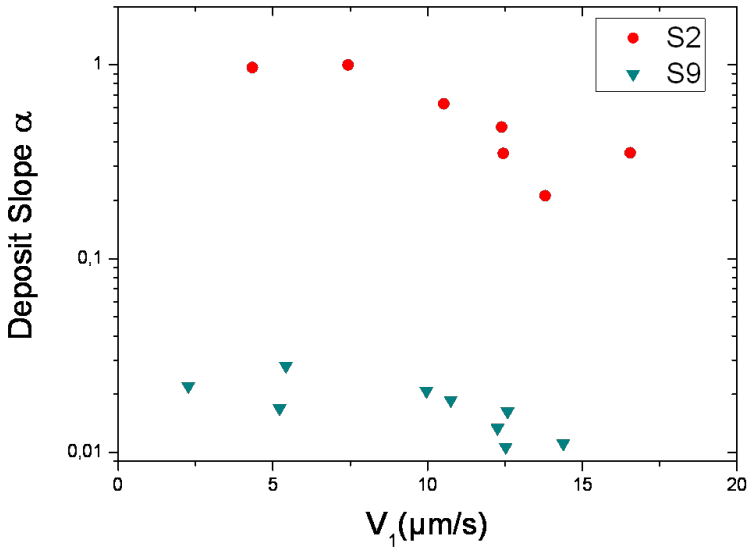

Figure 3.24: Downward slope comparison for 2 pH values.

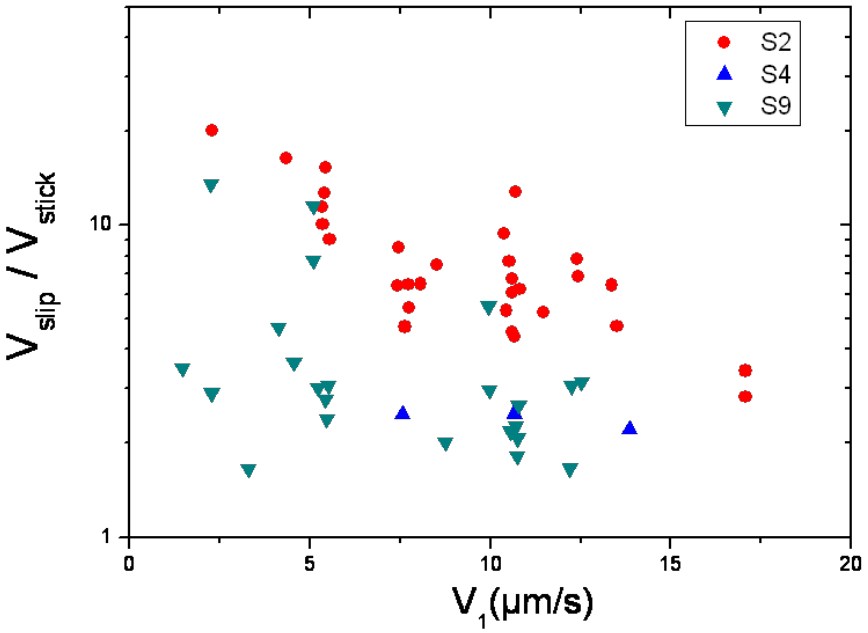

Figure 3.25: ratio of slip velocity versus stick velocity

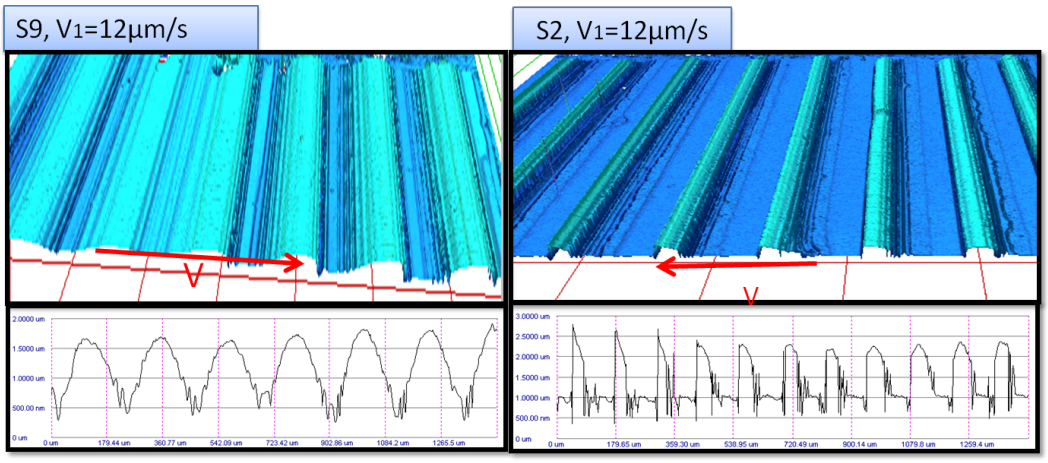

Figure 3.26: 3D images obtained from profilometer measurement of the colloidal depositions under different pH values. The lower images are the cross section contour line of the morphologies.

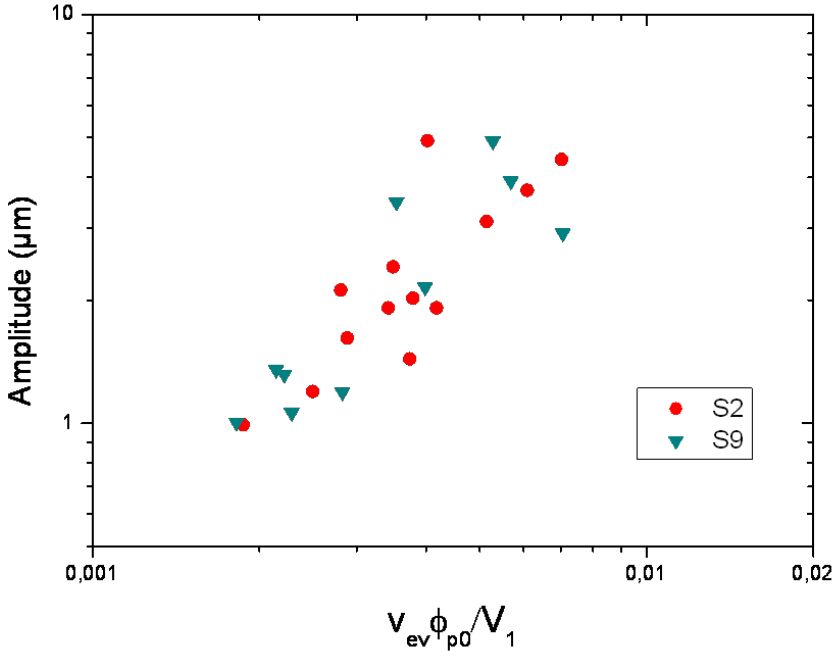

Figure 3.27: Amplitude as a function of all the parameters

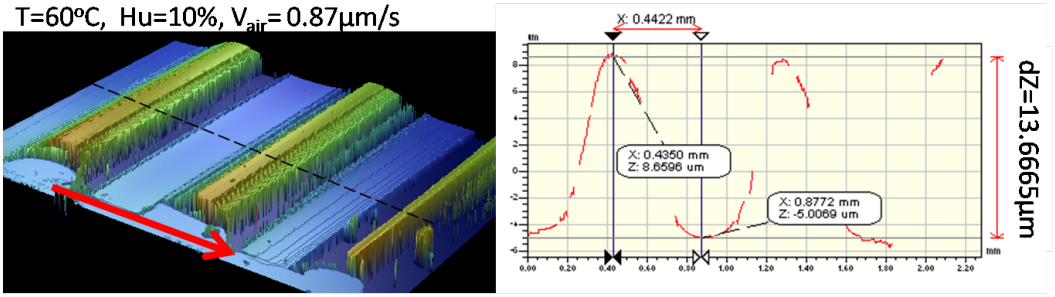

Figure 3.28: Morphology for PAAm solution drying at high temperature. Experimental conditions: $V_1 \simeq 2\mu m/s$, $\phi_{p0} = 5\%$, PAAm with molar mass = 10000 g/mole. Temperature is at $60°C$. The slope of the stripe pattern is too steep to be obtained from profilemeter.

stripe patterns. The experimental conditions are :$V_1 \simeq 2\mu m/s$, $\phi_{p0} = 5\%$, PAAm with molar mass = 10000 g/mole with evaporation velocity $V_{ev} = 2.7\mu m/s$. As can be seen the amplitude (dz) is $13\mu m$. Note that the red arrow refers to the receding contact line direction. The profiles below the 3D images are cross sections corresponding to the dash lines. Note that the profile of the stripe patterns is not complete. The slope of the bump is too large to be obtained from profilometer. However, the amplitude which is defined as the distance between the highest and lowest point can still be obtained as shown in the figure 3.28.

Results are summarized in table 3.29. As can be seen, the amplitude increases with $\frac{\phi_{p0}V_{ev}}{V_1}$ as for colloidal suspensions. We have not enough points to go further in the analysis. It will be interesting to complete the results on the one hand, and to perform experiments with colloids at high evaporation rate on the other hand.

3.4 Discussion

As stated in the introduction, some models rely on the modification of the equilibrium contact angle to explain some characteristics of the observed stick-slip. We are going to test these models using our experimental results.

Volume Fraction	V1(µm/s)	Vev(µm/s)	Amplitude(µm)	$\phi_{p0}V_{ev}/V_1$
1.35%	1.2	0.26	0.33	0.003
3.4%	2.0	2.69	13.3	0.046
3.4%	4.1	3.22	5.8	0.027
3.4%	1.9	2.67	11.4	0.048

Figure 3.29: Table to summarize the morphology of the stripe patterns formed by PAAm solution.

3.4.1 Topological origin of the pinning

It is well known that a contact line can be pinned by a topological change of a surface [63], so we can try to relate the value of the pinning force to the geometry of the deposit. Indeed, when the contact line stands on the negative slope of the deposit (the positive direction being given by the displacement of the contact line, see figure 3.30), the effective contact angle θ is modified in such a way that it produces a pinning. Assuming the same equilibrium contact angle θ_0 on the substrate (glass) and the deposit (silica), the pinning force reads

$$F_p = \gamma \, \Delta cos\theta \simeq \ \gamma \, \alpha \, sin\theta_0. \tag{3.8}$$

In a previous work [46], the pinning force F_p and the deposit slope α were measured by the same technics than in the present article, on the same suspension than S9 samples (pH close to 9, same particle diameter). The values of F_p predicted by equation 3.8 were found to be in very good agreement with the direct measurements. The conclusion is very different if we take into account the new results at low pH. Indeed, we see in figure 3.12 that the pH doesn't induce any significant effect on the pinning force, while figure 3.24 shows that the slope α is changed by at least one order of magnitude. This clearly demonstrates that the above model is not pertinent. One point that may be erroneous in this approach is the assumption of a clear transition between the deposit, considered as

a solid, and the solution with a well defined contact line as sketched in figure 3.30. This view appears too simple to model the forming deposit.

3.4.2 Free meniscus at the top of the deposit

Another static model has been proposed by Watanabe *et al* [41] and Lee *et al* [47]. These authors consider a liquid meniscus on a solid multilayer deposit of height h_d. The contact angle at the top of the deposit is assumed flexible, due to particle sphericity. When the liquid level decreases, the meniscus stretches itself out, keeping its static shape (i.e. given by the Laplace law), and get closer from the substrate (see figure 3.30). When the distance h_c between the meniscus and the substrate is too small, the meniscus breaks up and the contact line jumps to another location, depending on the particles diameter D_p. Adapting this approach to our geometry is very easy. Indeed, in our case, the gap $d = 1mm$ between the plates is much smaller than water capillary length, so the meniscus is a circle, of diameter d at break out. Assuming $h_d \ll d$, simple geometric arguments lead to the following expression for the band spacing w:

$$w = z_1 + z_2 \simeq \sqrt{d(h_d - h_c)} + \sqrt{d(D_p - h_c)} \tag{3.9}$$

The parameter h_c is included in the range from 0 to the particle diameter D_p (Watanabe *et al* [41] obtained a good agreement with their experiments taking h_c/D_p of $0.5 - 0.8$).

Comparison of our experimental results with Watanabe *et al* model was deduced from optical profilometer profiles. It was restricted to S_2 solutions, for which the distance between the top of the deposit and the new pinning event can be clearly measured (cf figure 3.26). Two limiting cases are considered: $h_c = 0$ and $h_c = D_p$. As seen in figure 3.31, this model gives the right order of magnitude of the band spacing, whatever the choice of h_c. The best agreement is obtained by setting $h_c = 0$. Then we can conclude that the unpinning mechanism proposed in this model is in agreement with our data. Nevertheless, it is far from giving a complete theory of stick-slip. Indeed, it cannot predict the wavelength. Moreover, it is limited to strong stick-slip configurations, where the slip velocity is much higher than the stick one.

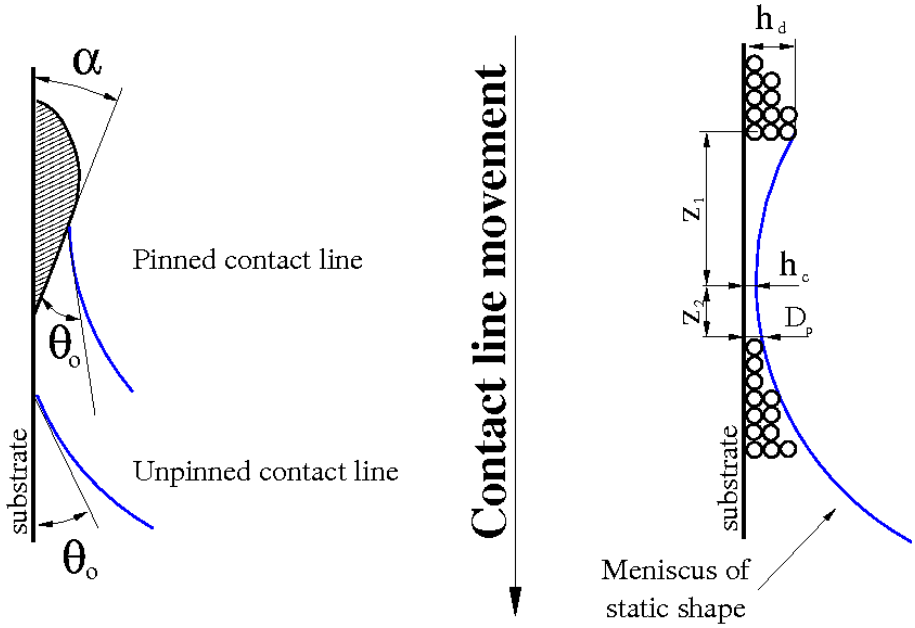

Figure 3.30: Models based on a variation of the equilibrium contact angle. Left: topological origin of the pinning force ; right: free meniscus at the contact line (with $c = 0$.)

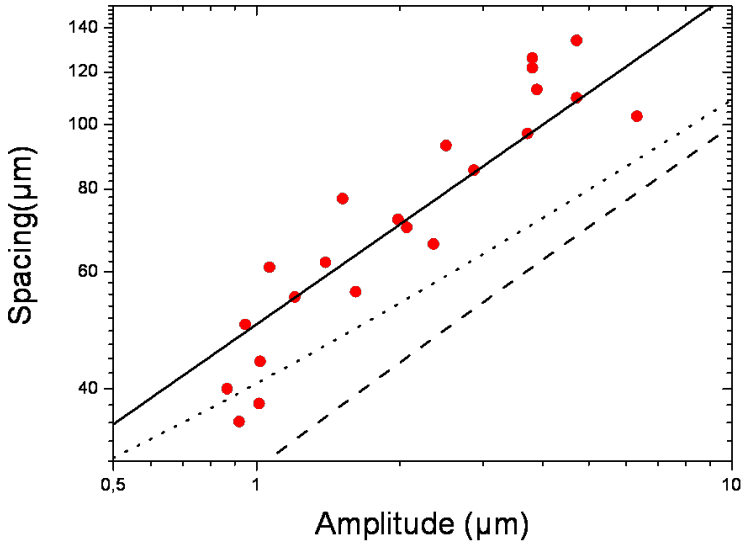

Figure 3.31: Spacings obtained with S_2 suspension. Comparison of experimental data with Watanabe *et al* model [41]

3.4.3 Hydrodynamic model: a promising track ?

The two models discussed above rely on equilibrium considerations. Another track should be to capture stick-slip phenomenon through a dynamical model, taking into account the hydrodynamic in the meniscus, and including the concentration dependent viscosity. Indeed, looking at the different results obtained in this experimental section, it seems that the viscosity might be a key ingredient. Since it changes with pH for colloidal suspensions and with temperature for polymer solutions. As stated in the introduction, the approach developed by Frastia *et al* [49] leads to a periodic patterning of the deposit, without any artificial trigger: the periodic movement of the contact line is produced by the competition between a dewetting and a drying fronts. However, the configuration under study is far from the one considered here, making any direct comparison impossible. Indeed, in their model, the chemical potential depends on the film pressure only (Kelvin effect with disjoining and capillary pressure), and not of the concentration. The main consequence is that evaporation decreases when the film thickness is small enough to activate Kelvin effect via the disjoining pressure, which happens when the thickness goes to nanometric scale [64]. In other words, the solution is assumed to evaporate like a pure liquid, and this restricts the use of the model to very dilute solutions, and ultrathin liquid films. Anyway, adapting this type of model to get closer from experimental configurations where the deposit thickness is of order of micron is a very interesting and promising issue.

Chapter 4

Numerical Simulation

In this chapter we present a first step towards the modelisation of our experimental set-up. Several simplifying assumptions are used. We focus on the concentration and velocity field induced by the evaporation and the moving substrate. This model does not aim to simulate the periodic stick/slip regime but analyze the effect of the evaporation velocity and substrate velocity on the mean deposit thickness. Numerical simulations results are compared with a **simplified model** and **experimental results**.

4.1 Model description

As a first step, we build a 2D model of our experimental set-up. We study the flow field and concentration distribution inside the meniscus induced by evaporation and the moving substrate. We consider a continuous model in Cartesian coordinates. The meniscus free surface spontaneously forms a circle-shape due to Laplace pressure. An electrostatic analogy, suggested by Deegan and co-authors [6], is used to evaluate the evaporation flux at the free surface. Note that this approach predicts a divergence of the evaporation velocity at the contact line. To solve the singularity problem, we truncate the tip part and we apply lubrication theory and mass balance to deduce the velocity field at the boundary with the truncated part.

4.1.1 Main assumptions

To simplify the model, there are several important assumptions:

1. Marangoni effect is neglected so that we assume zero tangential stress at the free surface of the meniscus.

2. No buoyancy effect.

3. Inertia is neglected. This assumption is valid when $Re = \frac{V_1 d}{\nu} << 1$, where V_1 is the receding velocity of the contact line, d is the characteristic length of the meniscus ($1mm$), $\nu \sim 10^{-6} m^2/s$ is the minimum kinematic viscosity of the solution. This assumption is thus valid for $V_1 << 1mm/s$.

4. The solution density, ρ, is a constant.

5. Isothermal problem, which is justified by temperature measurements. We found that, at 25^oC there is only 2^oC difference between the bulk temperature and the air temperature. (Note that our dip-coating-like set-up is inside a thermostated environment).

6. The **local evaporation rate** $j(m/s)$ is $\frac{J_0}{\sqrt{D_{tip}}}$ [6] where D_{tip} is the distance to the tip. Note that this expression holds for the tip vicinity. In this study it is extended to the whole meniscus free surface, as a first approximation. $J_0(\frac{m^{3/2}}{s})$ is a constant deduced from the **mean evaporation velocity** V_{ev} (m/s) deduced from our experiment. See appendix D for the relation between the **local evaporation velocity** j and the **mean evaporation velocity** V_{ev} (m/s).

4.1.2 Geometry and governing equations

The model is constructed to simulate our experimental set-up (figure 4.1). The total height is $H = h + h_m$; h is large enough to define realistic boundary conditions at the bottom (cf. next section). R stands for meniscus radius. For total wetting configuration, $h_m = R = d/2$. In the experimental configuration, the contact line receding velocity is

V_1, imposed by pumping. In our model, we suppose that the wall is moving toward $+y$ direction with velocity V_1, while the liquid solution is fixed.

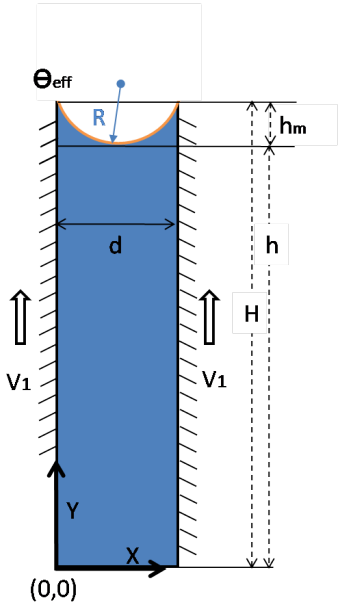

Figure 4.1: Sketch of the model geometry.

For our problem, we focus on the flow inside the meniscus. We define the truncated region shown in figure 4.2 by cutting off a small tip region whose height is α and width is δ. Here δ is a function of α and the effective contact angle θ_{eff} ($\theta_{eff} = 0$ in total wetting).

Equations solved in the blue domain shown in figure 4.3 are discussed in the following. We first assume an incompressible flow of Newtonian fluid with constant viscosity and steady state, therefore the mass conservation and the Navier-Stokes equations read in vector form:

$$\vec{\nabla} \cdot \vec{v} = 0\,, \tag{4.1a}$$

$$\rho(\vec{v} \cdot \vec{\nabla})\vec{v} = -\vec{\nabla}P + \vec{\nabla} \cdot (\mu\vec{\nabla}\vec{v} + \mu\vec{\nabla}^t\vec{v}) \tag{4.1b}$$

where ρ is the density of the fluid, $\vec{v} = u\vec{x} + v\vec{y}$ is the velocity field; μ is the viscosity.

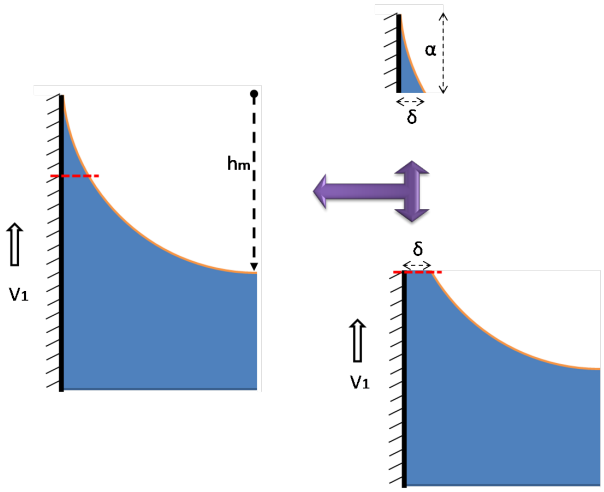

Figure 4.2: Sketch for the meniscus boundary conditions truncated by red line. The width is δ and the height is α

As stated in the main assumption, we ignore the inertia term to get the so-called "Stokes Equation", with variables u, v, P:

$$0 = -\vec{\nabla}P + \vec{\nabla} \cdot (\mu\vec{\nabla}\vec{v} + \mu\vec{\nabla}^t\vec{v}) \tag{4.2}$$

The mass balance for the solute leads to equation (4.3). It contains the convective term (left) and diffusive terms (right) in steady state. ϕ_p is the volume fraction of solute and D is the **binary diffusion coefficient**:

$$\vec{v} \cdot \vec{\nabla}\phi_p = D\nabla^2\phi_p \tag{4.3}$$

In conclusion, there are four variables u, v, P, ϕ_p governed by equations (4.1a), (4.2) and (4.3).

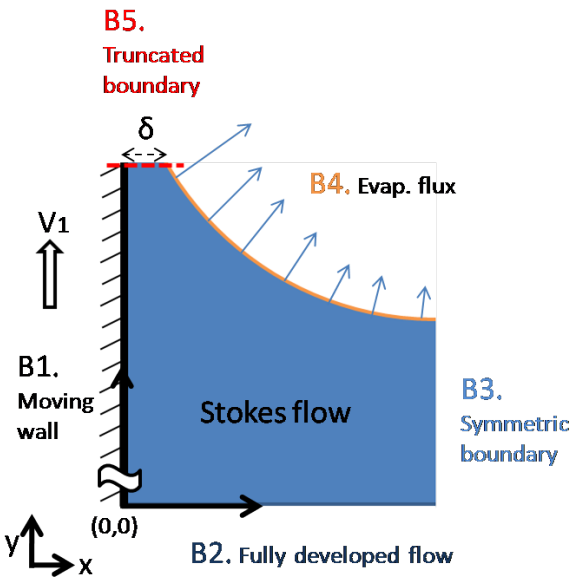

Figure 4.3: 5 boundary conditions.

4.1.3 Boundary conditions

The boundary conditions are shown in figure 4.3:
Boundary 1: At $x = 0$ the moving wall velocity is V_1. We assume no slip and impermeable boundary conditions so that:

$$u = 0\,, \tag{4.4a}$$

$$v = V_1\,, \tag{4.4b}$$

$$\frac{\partial \phi_p}{\partial x} = 0 \tag{4.4c}$$

Boundary 2: At y=0 we consider a fully developed flow, which implies that the velocity field does not change in $\vec{y}$ direction. Impermeable condition (eq (4.4a)) condition along the wall (B1) and mass conservation (cf 4.1a) imply $u = 0$ along B2. In such a case the pressure gradient along the boundary will balance shear stress at the wall. Concentration is assumed to be the bulk concentration ϕ_{p0} of the inflow, while diffusion is neglected for

the outflow. Summary is given in the following equations:

$$u = 0\,, \tag{4.5a}$$
$$\frac{\partial v}{\partial y} = 0\,, \tag{4.5b}$$
$$\vec{v}\cdot\vec{y} > 0, \Longrightarrow \phi_p = \phi_{p0}, (inflow)\,, \tag{4.5c}$$
$$\vec{v}\cdot\vec{y} < 0, \Longrightarrow \frac{\partial \phi_p}{\partial y} = 0, (outflow) \tag{4.5d}$$

Boundary 3: at $x = R$, the velocity or concentration fields are symmetric along the plan $x = R$, from $y = 0$ to $y = h$:

$$u = 0\,, \tag{4.6a}$$
$$\frac{\partial v}{\partial x} = 0\,, \tag{4.6b}$$
$$\frac{\partial \phi_p}{\partial x} = 0 \tag{4.6c}$$

Boundary 4: along the meniscus, we suppose that the viscous shear stress along the interface is 0. Note that we switch from the global coordinate $\vec{v} = u\vec{x}+v\vec{y}$ into $\vec{v} = u_n\vec{n}+u_t\vec{t}$ with $\vec{n}\cdot\vec{t} = 0$ and the norm of tangential and normal vectors along the meniscus are $\|\vec{n}\| = \|\vec{t}\| = 1$ (cf figure 4.4). The local mass flux $\vec{J} = \vec{J_p} + \vec{J_s}$ where $\vec{J_p}$ is the solute mass flux and $\vec{J_s}$ is the solvent mass flux.

In our experiment, the solute across the meniscus is nonvolatile, so that the normal flux of solute across the meniscus is zero $\vec{n}\cdot\vec{J_p} = 0$. The total normal flux, $\vec{J}\cdot\vec{n} = j \times {\rho_s}^0$, is the local evaporation rate j times the pure solvent density. Here we use Deegan's proposition [6] for the evaporation rate. With the assumption of constant density for the solution, one can deduce $j = u_n$ (cf Appendix C). J_0 is a constant which can be experimentally obtained. The boundary conditions are summarized in the following equations:

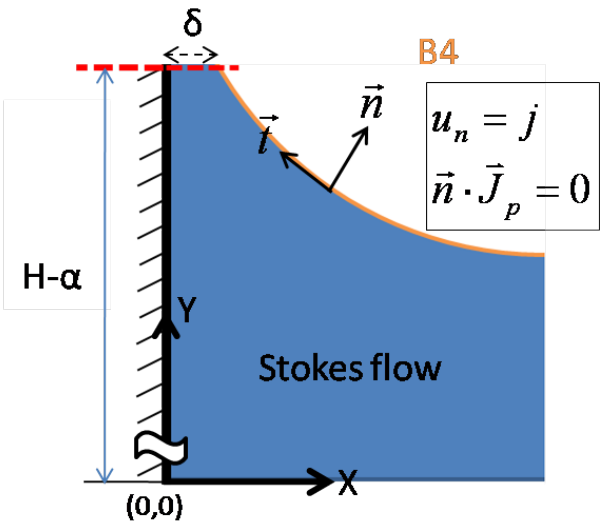

Figure 4.4: boundary condition along meniscus surface

$$\frac{\partial u_t}{\partial n} + \frac{\partial u_n}{\partial t} = 0\,, \tag{4.7a}$$

$$\vec{J}_p \cdot \vec{n} = 0\,, \tag{4.7b}$$

$$u_n = j\,, \tag{4.7c}$$

$$j = \frac{J_0}{\sqrt{H - y}} \tag{4.7d}$$

Boundary 5: The last boundary is the most intricate. We truncate a small distance of the contact angle with the width δ and height α, see figure 4.2. This small cut off allows us to ignore the singularities at the contact line. Since we assume a small contact angle along the boundary, the flow can be assumed quasi parallel to the moving wall and lubrication approximation can be applied. Moreover, δ is assumed small enough to neglect the variation of solute volume fraction along the boundary. The simplified Stokes equations reads:

$$\frac{\partial P}{\partial x} = 0\,, \tag{4.8a}$$

$$\frac{\partial P}{\partial y} = \mu \frac{\partial^2 v}{\partial x^2} \tag{4.8b}$$

From equation (4.8a) and (4.8b), $\frac{\partial^2 v}{\partial^2 x}$ only depends on y. By integration we get:

$$\frac{\partial^2 v}{\partial x^2} = K(y) \Longrightarrow v(x,y) = ax^2 + bx + c \tag{4.9}$$

Coefficients $a(y)$, $b(y)$, $c(y)$ are obtained using the conditions:

1. at $x = 0$, the no slip condition gives $v(x = 0, y = H - \alpha) = V_1 \Rightarrow c = V_1$.

2. at $x = \delta$, the shear stress is 0, so $\frac{\partial v}{\partial x} \mid_{x=\delta} = 0 \Rightarrow 2a\delta + b = 0$.

3. $\int_0^\delta v(x,y)dx = \bar{V}_{tip} \cdot \delta$, with $\bar{V}_{tip}$ the mean velocity of y component along the boundary.

From the 3 equations,we get $v(x,y)$ along boundary 5:

$$v(x,y) = \frac{3}{\delta}(\bar{V}_{tip} - V_1)x(1 - \frac{x}{2\delta}) + V_1 \tag{4.10}$$

The x component of velocity $\vec{v}$ is deduced from mass conservation (4.1a):

$$\frac{\partial u}{\partial x} + \frac{\partial v}{\partial y} = 0 \quad \Rightarrow \quad u(x,y) = -\int_0^x \frac{\partial v}{\partial y} dx' \tag{4.11a}$$

combined with equation 4.10 and computed by MAPLE software, we get:

$$u(x,y) = [\bar{V}_{tip}\frac{d\delta}{dy}(3\delta - 2x) + V_1\frac{d\delta}{dy}(2x - 3\delta) + \delta\frac{d\bar{V}_{tip}}{dy}(x - 3\delta)]\frac{x^2}{2\delta^3} \tag{4.12}$$

In the following we are going to deduce 1)$\frac{d\delta}{dy}$, 2)$\frac{d\bar{V}_{tip}}{dy}$ as a function of $\bar{V}_{tip}$:

1. For small contact angle ($\theta_{eff} << 1$), small slope approximation can be used to get:

$$\delta(y) = (H_t - y)\theta_{eff} + \frac{(H_t - y)^2}{2R} \quad \Rightarrow \quad \frac{d\delta}{dy} = -\theta_{eff} + \frac{y - H_t}{R} \tag{4.13}$$

Here H_t is the total height of the meniscus except the truncated part, therefore equals to $H - \alpha$ (cf figure 4.4).

2. $\frac{d\bar{V}_{tip}}{dy}$ can be obtained by considering the local mass balance (with the assumption of constant density ρ for the solution):

$$\frac{d}{dy}(\bar{V}_{tip}\delta) = -j(y) \quad \Rightarrow \quad \frac{d\bar{V}_{tip}}{dy} = -\frac{1}{\delta}[j(y) + \bar{V}_{tip}\frac{d\delta}{dy}] \tag{4.14}$$

The **hydrodynamic boundary conditions** on B5 are thus given by equations (4.10), (4.12), (4.13), (4.14), which express u, v as a function of the mean velocity $\bar{V}_{tip}$ over B5. At this stage, $\bar{V}_{tip}$ is still unknown. The determination of $\bar{V}_{tip}$, which requires more information, will be described in the next section.

Finally, we also need a boundary condition on the **concentration field**. Assuming that B5 is an outlet ($\vec{v}\cdot\vec{y} \geq 0$ over the whole boundary), we impose the following condition:

$$\frac{\partial \phi_p}{\partial y} = 0 \tag{4.15}$$

We expect that this approximation induces an error in a small region over a length of order $\frac{D}{\bar{V}_{tip}}$ close to the boundary. The validity of this assumption will be checked in section 4.3.2.

4.1.4 Estimation of $\bar{V}_{tip}$

The value $\bar{V}_{tip}$ is obtained by a global mass balance on the truncated part of the tip (cf figure 4.5). Assuming total drying in the tip (no more solvent for $y > H$) and if the solute volume fraction ϕ_p is about constant along the boundary, the global mass balance in the truncated tip reads (with $ds \simeq dy$ in the tip):

$$\bar{V}_{tip}(1 - \bar{\phi_p})\delta = \int_{H-\alpha}^{H} \frac{J_0}{\sqrt{H-y}}\,\mathrm{d}y = 2J_0\sqrt{\alpha} \tag{4.16}$$

where $\bar{\phi_p}$ is the average volume fraction of solute along the boundary. Since $\bar{V}_{tip}$ depends on $\bar{\phi_p}$, it is obtained by successive trials. For a given value $\bar{V}_{tip} = \bar{V}_i$, the velocity

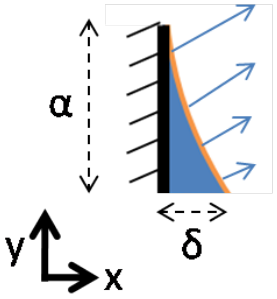

$$Flux = \int_{H-\alpha}^{H} \frac{J_0}{\sqrt{H-y}} dy$$

Figure 4.5: truncated tip

and concentration fields are obtained in the 2D computational domain by solving the equations presented in the previous section. Thus we get $\bar{\phi}_{p_i}$, the solute volume fraction at boundary 5.

We check that equation (4.16) satisfied for the two values $\bar{V}_i$ and $\bar{\phi}_{p_i}$. If not, a new trial is performed with another value of $\bar{V}_{tip}$ until the relative error is less than 1%. Error is defined as:

$$Err_i = \frac{\bar{V}_i(1-\bar{\phi}_{pi})\delta - 2J_0\sqrt{\alpha}}{2J_0\sqrt{\alpha}} \tag{4.17}$$

We will show examples after we implant our model into COMSOL software.

4.1.5 Dry thickness

Deposition thickness can be obtained knowing $\bar{\phi}_p$ and $\bar{V}_{tip}$ from the above solution. We assume that the deposit moves at substrate velocity V_1. In the truncated region shown in figure 4.6, the total solute across boundary 5 (cross section δ) should be $\bar{\phi}_p \times \delta \times \bar{V}_{tip}$, and the total deposit on the moving substrate should be $h_d \times V_1 \times \phi_c$ where ϕ_c is the compaction of the deposit such as 0.74 for a close-packing deposit. For simplicity, we assume completely dry deposit, so $\phi_c \simeq 1$. The mass balance reads:

$$h_d \times V_1 = \bar{\phi}_p \times \delta \times \bar{V}_{tip} \quad \Rightarrow \quad h_d = \frac{\bar{\phi}_p \times \delta \times \bar{V}_{tip}}{V_1} \tag{4.18}$$

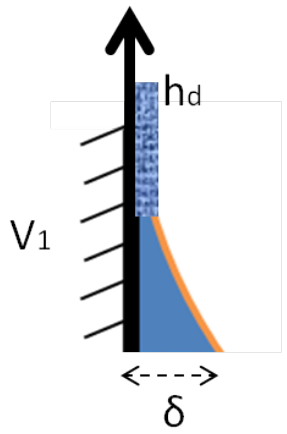

Figure 4.6: Film thickness deduced from solute mass balance in the truncated region

4.2 COMSOL Implemention

In this section, we will implement the theoretical model into a commercial software called COMSOL. This software is based on finite element method. It offers 5 simple steps for implementation and to obtain solutions: **1.Define geometry 2.Specify physics 3.Define mesh 4.Solve 5.Visualize results.** Following are the geometry scales and testing variables' ranges inspired by our experimental set-up and parameters:

- The total Height H : $3mm < H < 20mm$.
- The truncated height α: $15\mu m < \alpha < 100\mu m$.
- The mean evaporation velocity V_{ev}: $0.78\mu m/s < V_{ev} < 1.5\mu m/s$.
- The substrate moving velocity V_1: $0.1\mu m/s < V_1 < 100\mu m/s$.
- The initial volume fraction of solute ϕ_{p0}: $1\% < \phi_{p0} < 10\%$.
- The dynamic viscosity: set to be constant $\mu = 0.001Pa \cdot s$, or variable from empirical laws: polymer solution viscosity $\mu_p(\phi)$, colloidal suspension viscosity $\mu_c(\phi)$.

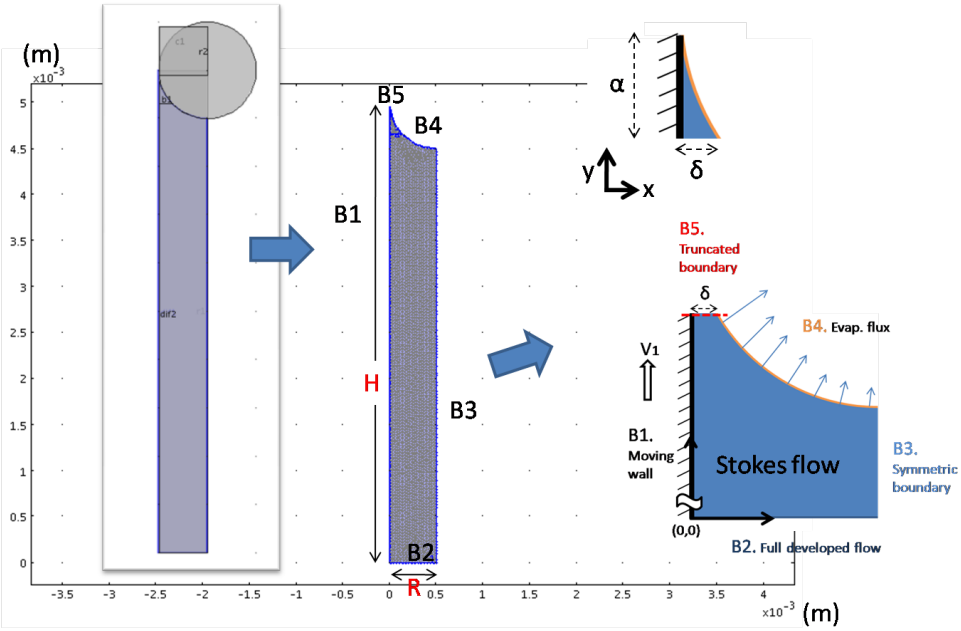

Figure 4.7: geometry buildup and 5 boundaries

- The diffusion coefficient D: $5 \times 10^{-12} < D < 5 \times 10^{-10} m^2/s$.

4.2.1 Model implementation

1.Define geometry

To build our model, we draw simple shapes and by difference we can have a flat edge at the tip part for boundary 5 whose width is δ. We select one example to walk through in detail: $H = 5mm$, $R = 0.5mm$, $\alpha = 50\mu m$ so that $\delta = 2.5\mu m$ as shown in figure 4.7 for a total wetting case.

2.Physics for domain and boundaries

Given the model described in the previous section, we couple two packages **Transport of dilute species** and **Creeping flow** from the model library. In **Transport of dilute**

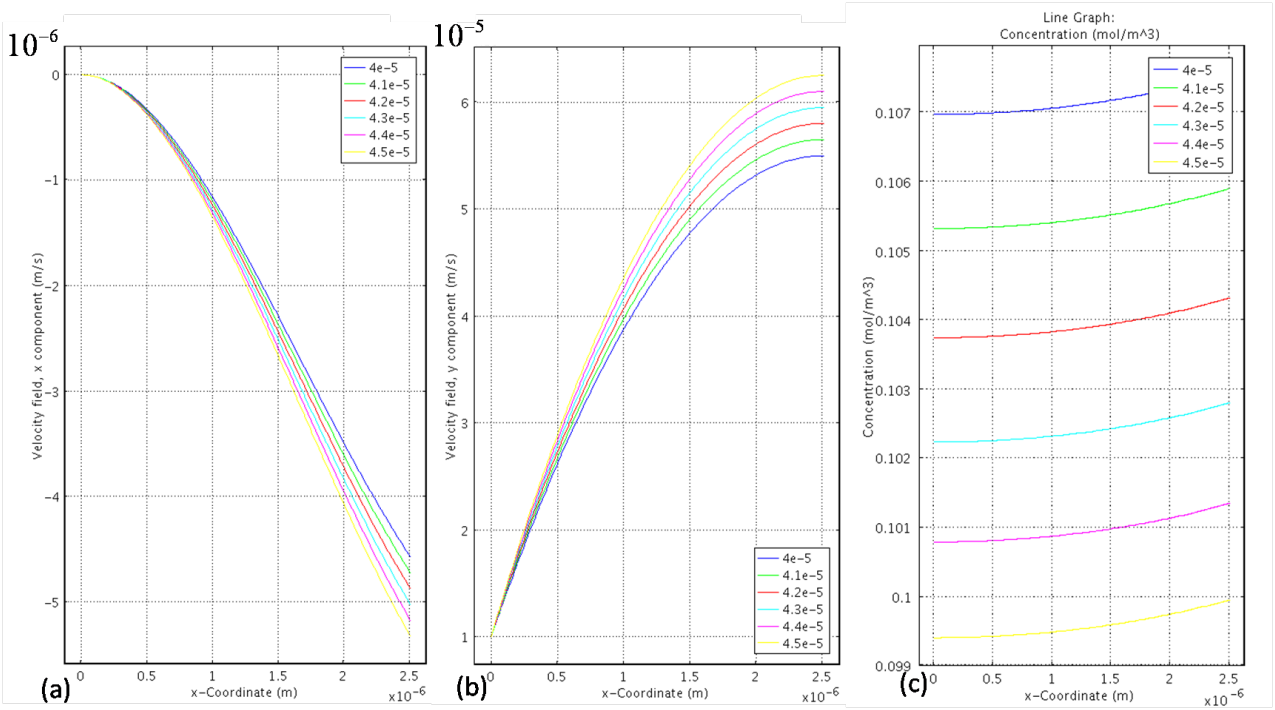

Figure 4.8: Simulation results corresponding to 5 different $\bar{V}_{tip} = (40\mu m/s, 41\mu m/s, ..., 45\mu m/s)$ along boundary 5. $V_1 = 10\mu m/s$, $V_{ev} = 1.5\mu m/s$, $\phi_{p0} = 3\%$. (a) the x component velocity profile. (b)the y component velocity profile (c)concentration profile

species equations are written for the solute. In **Creeping flow**, Stokes equation is solved for the velocity and pressure (cf appendix E for details).

4.2.2 Example of iterative procedure

One example is shown for the procedure in COMSOL. In this example, the moving substrate velocity is $V_1 = 10\mu m/s$, the evaporation velocity $V_{ev} = 0.78\mu m/s$, the initial volume fraction is 3%. Different $\bar{V}_{tip} = (40\mu m/s, 41\mu m/s, ..., 45\mu m/s)$ are manually input to COMSOL software for simulation. Then, different velocity profiles and concentration profiles along boundary 5 are obtained. They are shown in figure 4.8. Note the v, y

V_1	$\bar{V}_{tip}$	$\bar{\phi}_p$	$(1-\bar{\phi}_p)*\bar{V}_{tip}$	$\frac{2J_0\sqrt{\alpha}}{\delta}$	Error
1,00E-05	4,10E-05	0,1055	3,67E-05	3,79E-05	3,234%
1,00E-05	4,20E-05	0,1039	3,76E-05	3,79E-05	0,696%
1,00E-05	4,30E-05	0,1024	3,86E-05	3,79E-05	-1,839%
1,00E-05	4,40E-05	0,101	3,96E-05	3,79E-05	-4,369%
1,00E-05	4,50E-05	0,0996	4,05E-05	3,79E-05	-6,908%

Figure 4.9: Numerical results corresponding to 5 different $\bar{V}_{tip}$. Yellow filled row is chosen for the solution based on mass balance. Error is defined in equation (4.17).

component of velocity, should be positive along the boundary since we assumed that in this narrow region there is no down flow. Figure 4.8(c) shows that the concentration along the boundary is almost a constant for each $\bar{V}_{tip}$ which is consistent with our assumption. Finally we average the concentration along boundary 5 to get $\bar{\phi}_p$ for mass balance calculation until the error is less than 1% by equation (4.17).

In table 4.9, we summarized numerical results for the trials $\bar{V}_{tip}$ based on the mesh of 10-element configuration discussed in the next section. As can be seen the **errors in the mass balance** depends on $\bar{V}_{tip}$ and the yellow colored row shows the lowest error (0.7%) from (4.17). Therefore $\bar{V}_{tip} = 42\mu m/s$ will be chosen to be the best approximation.

4.2.3 Mesh optimization

Before we start to study our model, we have to try several meshes to reach a reasonable result while saving the cpu memory and the program running time. We will compare

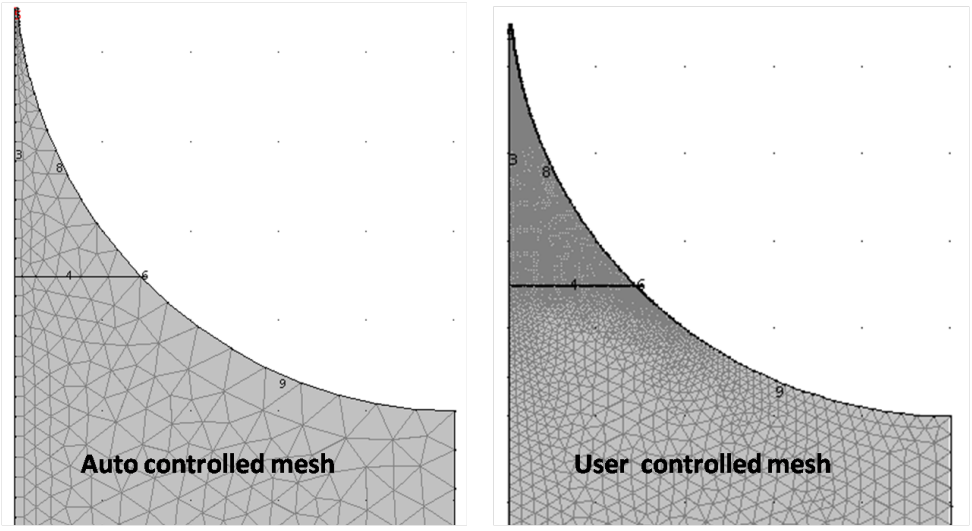

Figure 4.10: Mesh control. Left: auto-mesh generated by COMSOL without tuning. Right: user-controlled mesh

results from different types of meshes by calculating global mass balance errors. There are some key points that we should take care: first, at boundary 5, more elements will be needed to describe accurately the results. Second, too many elements in the whole domain can saturate the memory or make too long computational time. Therefore, we divide the meniscus into two domains: 1. the narrow part at the upper meniscus which is the crucial part for all the results. 2. the lower part. Figure 4.10 shows two examples of mesh. The first is **auto controlled mesh** generated by COMSOL without tuning anything. The second one is called **User controlled mesh**, which can be fine controlled by defining the element size and shape, element growth rate, resolution of narrow regions, etc. Therefore, you will find the second one is much refined, especially in the upper part of the meniscus.

Mesh generating time for both methods are less than 1 minute. Therefore, we will stick on **user controlled mesh** which allows us to tune more functions for a desired mesh. Therefore, different resolutions at the narrow region will be mainly compared. Five mesh methods at the truncated region are compared in detail as shown in figure 4.11:

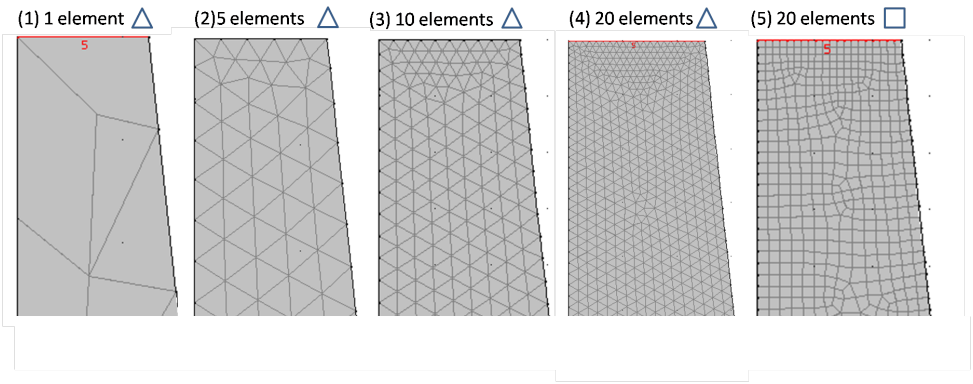

Figure 4.11: 5 mesh configurations at the tip part

1. Generated by auto controlled mesh with 1 element △ at tip part.
2. Generate by user controlled mesh with 5 elements △ at tip part.
3. Generate by user controlled mesh with 10 elements △ at tip part
4. Generate by user controlled with 20 elements △ at tip part.
5. Generate by user controlled with 20 elements □ at tip part.

After solving the test case ($V_1 = 10\mu m/s$, $V_{ev} = 0.78\mu m/s$, $\phi_{p0} = 3\%$.), velocity profile along boundary 5 are plotted for the comparison of five mesh configurations. At first glance, the velocity profile are similar for all mesh configurations except auto controlled mesh. Since there is only one element in the boundary, we get a straight line for the velocity and concentration and this solution is not accurate enough. Zoom in figures shown at top right corner of figure 4.12, shows that the other four meshes configurations give similar results for velocity and concentration.

In order to optimize the mesh configuration, we numerically compare the **total number of mesh elements**, **calculating times**, and **global mass balance errors** summarized in the table shown in 4.14. Note that for all mesh methods, we use the same discretization: *linear* for **pressure**, *quadratic* for **velocity** and **solute concentration**. The total number of elements depends on the size and the shape. More mesh elements

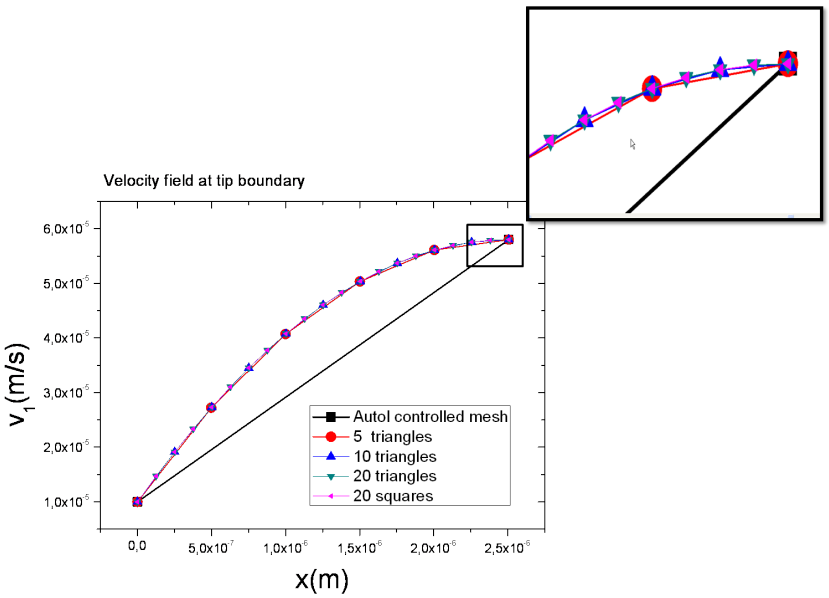

Figure 4.12: Velocity profile along B5 for 5 different mesh configurations.

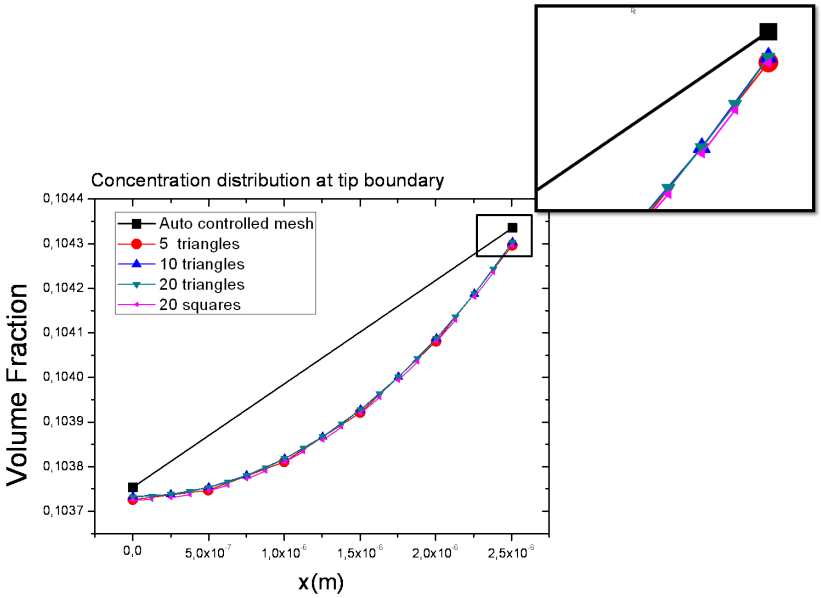

Figure 4.13: Solute volume fraction distribution along B5 for 5 different mesh configurations.

Mesh Method	Total # of Elements	Degree of Feedom	Computational Time(s)	$\int_{B2} vdx$	$\int_{B4+B5} vdx$	Error
Auto controlled	7763	54038	30	4,01E-10	4,13E-10	-3,008%
5 triangles	12646	84338	16	4,02E-10	4,04E-10	-0,363%
10 triangles	22249	147699	29	4,03E-10	4,03E-10	-0,191%
20 triangles	68160	448266	97	4,03E-10	4,03E-10	-0,174%
20 squares	52662	469002	113	4,03E-10	4,03E-10	-0,114%

Figure 4.14: Table of 5 mesh configurations comparison under condition of $V_1 = 10\mu m/s$, $V_{ev} = 1.5\mu m/s$, $\phi_{p0} = 3\%$.

gives more degree of freedom, therefore, needs more calculating time. All simulation times are within 2 minutes as can be seen in the table. The last three columns correspond to global mass balance estimation: we expect the integration of fluid velocity at boundary 2 should be equal to the integration of fluid velocity along boundary 4 and 5. The last column indicates the relative difference between these two quantities. As you can see, the error decreases while the number of mesh elements increase. 10-elements mesh configuration gives the same errors as 20-elements one. Besides, the running time is 3 times shorter. Therefore, we use 10-elements configuration in the following discussion.

4.3 Validation of Boundary conditions

Definitions of boundary conditions in B1, B3 and B4 do not require further validations since they do not demand specific assumptions. On boundary 2 we assume fully developed flow, bulk concentration for the in flow and we neglect solute diffusion. On Boundary 5 we assume no back flow, quasi uniform concentration The objective of this section is to define the computational domain (height H and truncated length α) so that these assumptions are valid, namely for arbitrary H and α the concentration and velocity fields must be the same or at least very close.

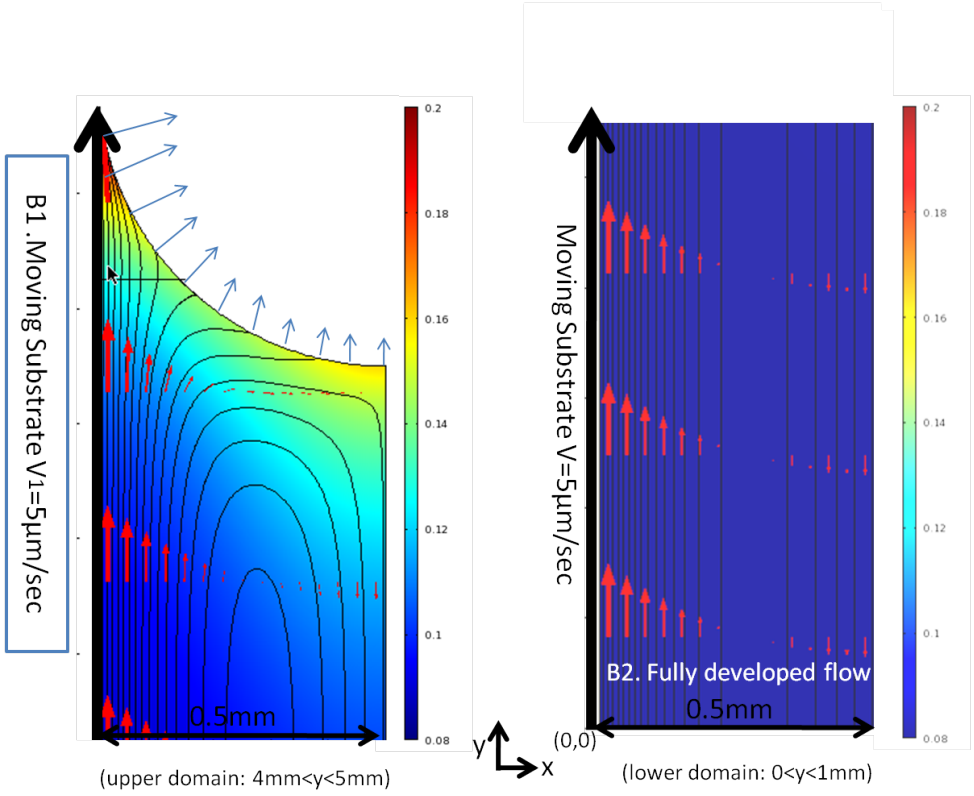

Figure 4.15: Numerical results corresponding to $V_1 = 5\mu m/s$, $V_{ev} = 0.78\mu m/s$, $\phi_{p0} = 3\%$. Left: upper domain. Right: lower domain with fully developed flow in boundary. Color bar shows the solute volume fraction, the stream lines and the arrows correspond to velocity field (u, v).

4.3.1 Flow field and concentration distribution

We first present the general behavior of flow field and concentration distribution. One example is shown in figure 4.15 corresponding to the conditions: $V_1 = 5\mu m/s$, $V_{ev} = 0.78\mu m/s$, $\phi_{p0} = 3\%$. Left figure is the zoom in at the upper domain near the meniscus free surface. The right one is the zoom at the bottom domain where "fully developed flow" is expected and it can be confirmed by the stream line plot. The total height we assumed $(= 5mm)$ is large enough. The flow itself is also reasonable: due to the movement of the substrate, the velocity is higher close to the moving substrate compared

to the velocity in boundary 3. Moreover, near boundary 5 which is the truncated part, solute accumulation is observed as expected. From the color bar which stands for the concentration, one can find the higher solute volume fraction near the free surface which is expected since only solvent evaporates.

4.3.2 Geometry test

Two cases will be discussed: First, we vary α with a fixed height H. Second, we vary H with a fixed truncated height α. We choose the following parameters: $V_1 = 5\mu m/s$, $V_{ev} = 0.78\mu m/s$, $\phi_{p0} = 8\%$. Higher substrate velocity will be discussed later. Three important results are going to be compared:

1. concentration distribution along several cross sections.
2. velocity field profile along several cross sections.
3. deposition thickness which can be deduced by mass balance, see equation (4.18).

1. Test for truncated height α

To validate the model, three geometries $\alpha = 15\mu m, 50\mu m, 100\mu m$ are compared in figure 4.16. The total meniscus height is fixed : $H = 5mm$. To compare the three geometries, color ranges for concentration data are from 8% to 16.75% so that blank parts near the tip part mean the concentration is above 16.75%. As can be seen, the concentration and velocity field distribution are qualitatively similar for the three geometries. To be more quantitative, four cross sections (separated by $100\mu m$) at upper meniscus $L1, L2, L3, L4$ are set as shown in figure 4.16. Figure 4.17 shows the concentration distribution along the four cross sections for three α. Colors correspond to four cross sections, 3 shapes are for the 3 different α. As can be seen they are the same. Figure 4.18 shows the y component of velocity along the four cross sections. Right figure is to zoom in for the square region. Little difference are found at cross section L4, but it is less than 1% which can be ignored.

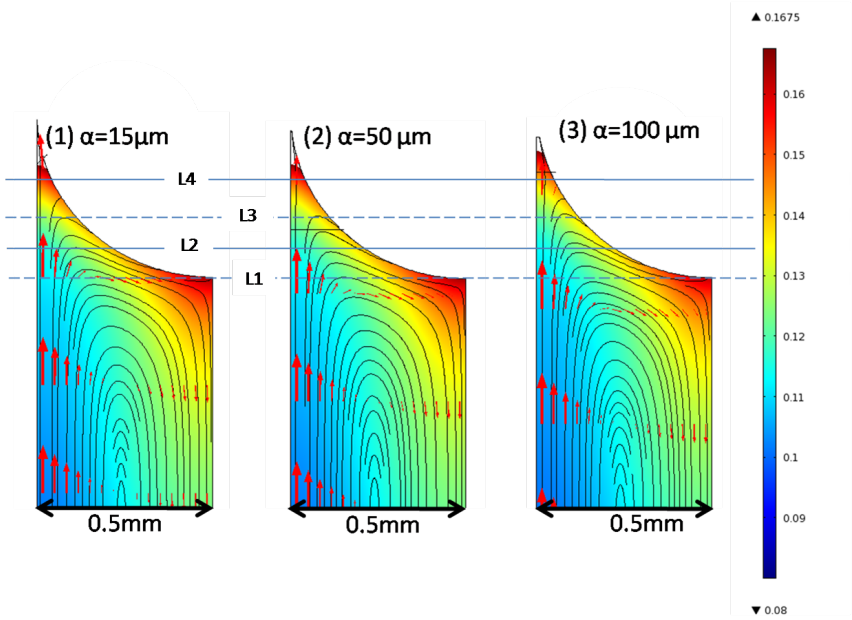

Figure 4.16: Flow field comparison for different α at $V_1 = 5\mu m/s$, $V_{ev} = 0.78\mu m/s$, $\phi_{p0} = 8\%$.

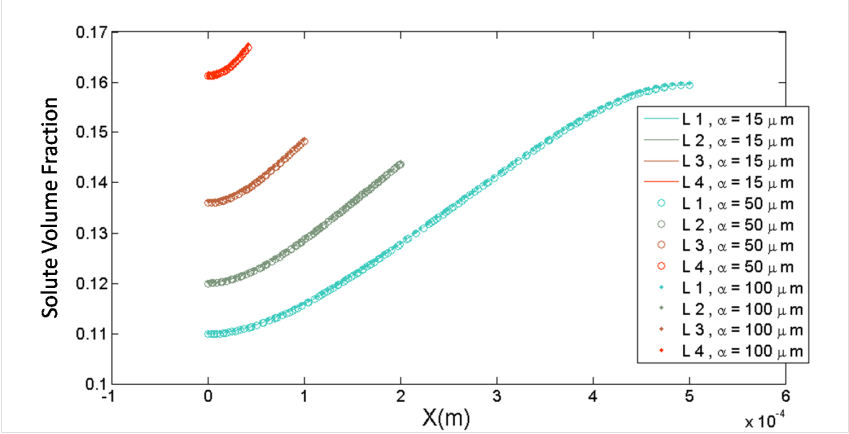

Figure 4.17: Concentration distribution along 4 cross sections at upper meniscus for 3 different α. Parameters: $V_1 = 5\mu m/s$, $V_{ev} = 0.78\mu m/s$, $\phi_{p0} = 8\%$, $H = 5mm$.

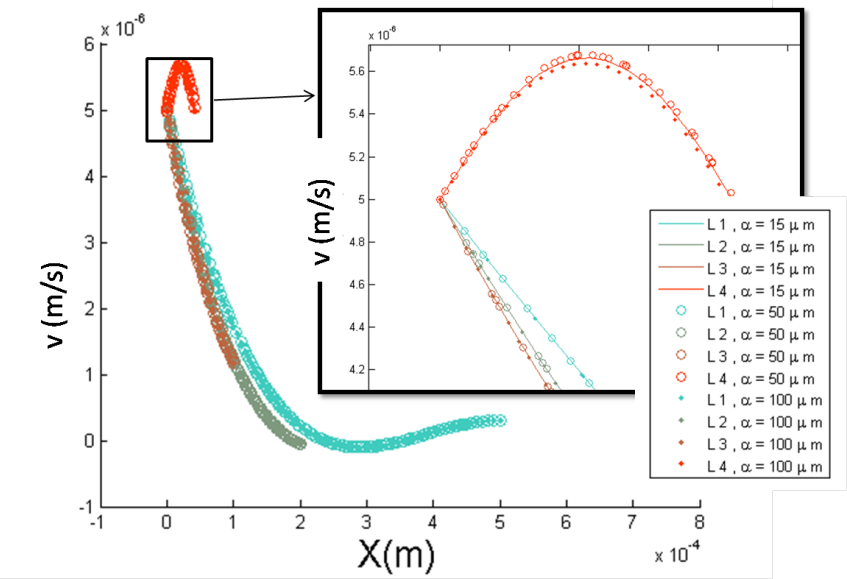

Figure 4.18: Velocity v along 4 cross sections in the upper part of meniscus for 3 different α. Parameters: $V_1 = 5\mu m/s$, $V_{ev} = 0.78\mu m/s$, $\phi_{p0} = 8\%$, $H = 5mm$.

2. Test for meniscus height H

Now we fix $\alpha = 15\mu m$ and change the total height of the meniscus $H = 5mm, 10mm, 20mm$ in the same testing case: $V_1 = 5\mu m/s$, $V_{ev} = 0.78\mu m/s$, $\phi_{p0} = 8\%$.

The results for upper meniscus cross sections (L1 to L4) are shown in figure 4.20 and 4.21. It confirms H has no effect on the concentration and velocity fields. The results for lower meniscus cross sections (cf figure 4.19) are shown in figure 4.22 and 4.23. It confirms that the three heights $H = 5mm$, $10mm$, $20mm$ give the same results not only for concentration, but also for the velocity fields at all cross sections, therefore, we can conclude the assumptions used to write boundary conditions at B2 are valid.

Finally, we test more substrate velocities for different H and α. The film thicknesses computed from equation (4.18) is shown in figure 4.24. It confirms that the results do not depend on the truncated height α and the total meniscus height H. For higher velocity, $10\mu m/s < V_1 < 100\mu m/s$ the same analysis was performed. It was shown that the tip length α must be smaller than $15\mu m$ to ensure the assumption of no back flow at the tip.

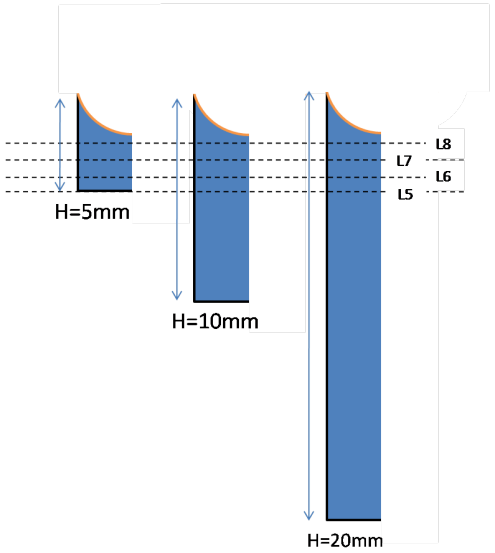

Figure 4.19: 4 cross sections ($L5 - L8$) for 3 different H.

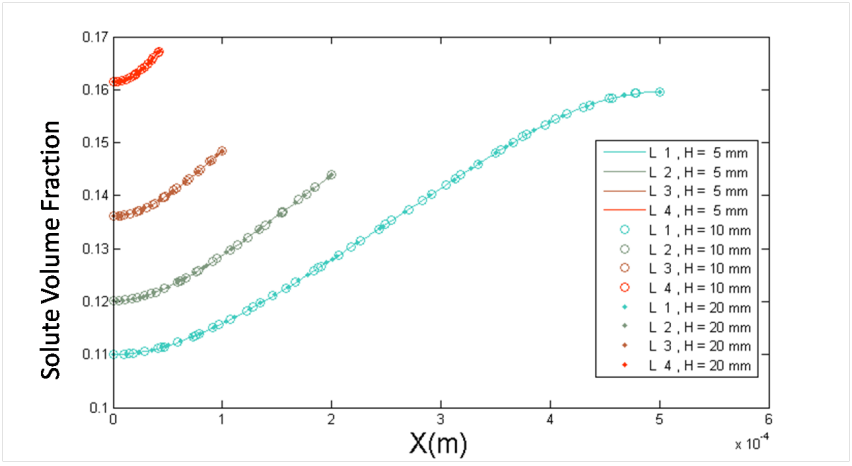

Figure 4.20: Concentration distribution along 4 cross sections (L1-L4) for 3 different H with the same parameters: $V_1 = 5\mu m/s$, $V_{ev} = 0.78\mu m/s$, $\phi_{p0} = 8\%$, $\alpha = 15\mu m$.

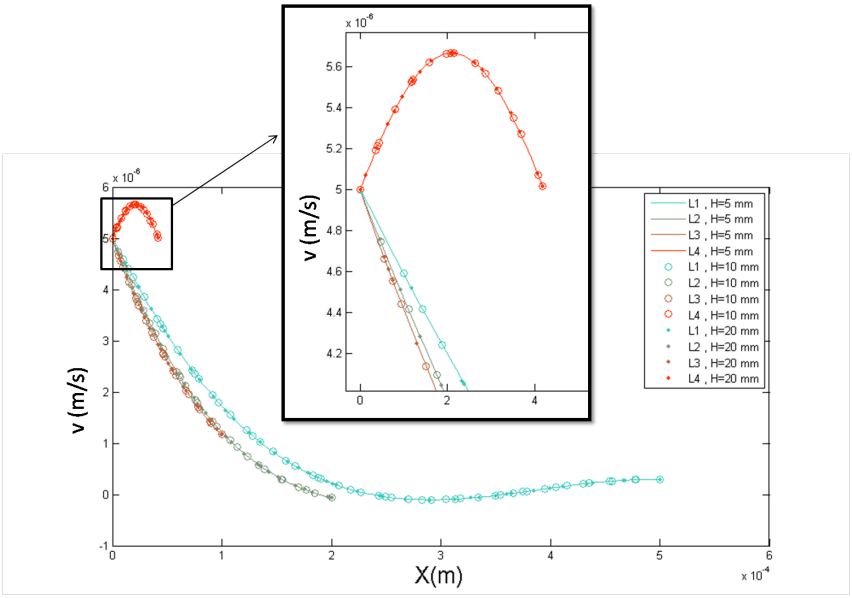

Figure 4.21: Velocity v along 4 cross sections for 3 different H with the same parameters: $V_1 = 5\mu m/s$, $V_{ev} = 0.78\mu m/s$, $\phi_{p0} = 8\%$, $\alpha = 15\mu m$.

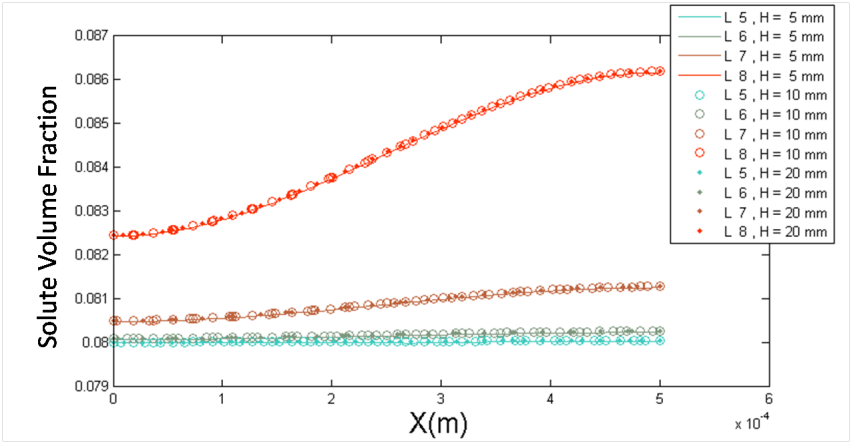

Figure 4.22: Concentration along 4 cross sections at lower meniscus for 3 different H. Parameters: $V_1 = 5\mu m/s$, $V_{ev} = 0.78\mu m/s$, $\phi_{p0} = 8\%$, $\alpha = 15\mu m$.

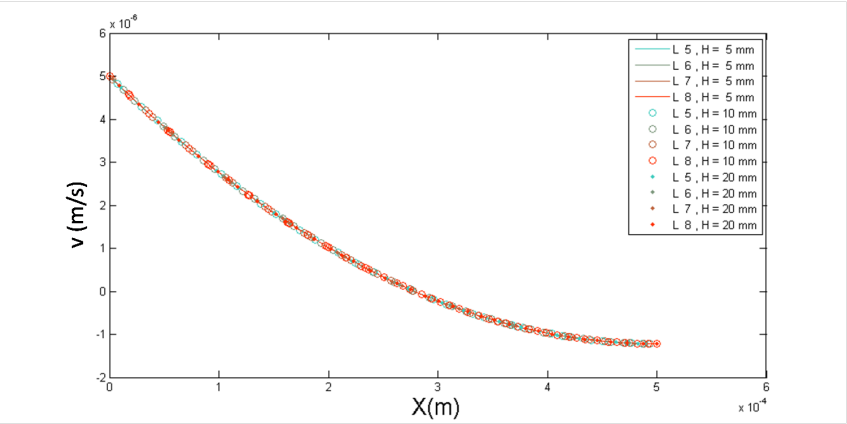

Figure 4.23: Velocity v along 4 cross sections at lower meniscus for 3 different H. Parameters: $V_1 = 5\mu m/s$, $V_{ev} = 0.78\mu m/s$, $\phi_{p0} = 8\%$, $\alpha = 15\mu m$.

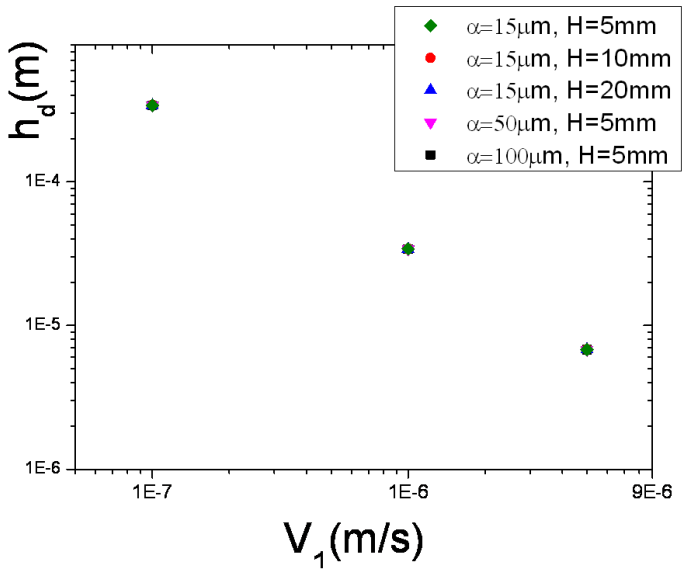

Figure 4.24: Film thickness versus substrate velocity for 3 different H at fixed $\alpha = 15\mu m$ and 3 different α at fixed $H = 5mm$.

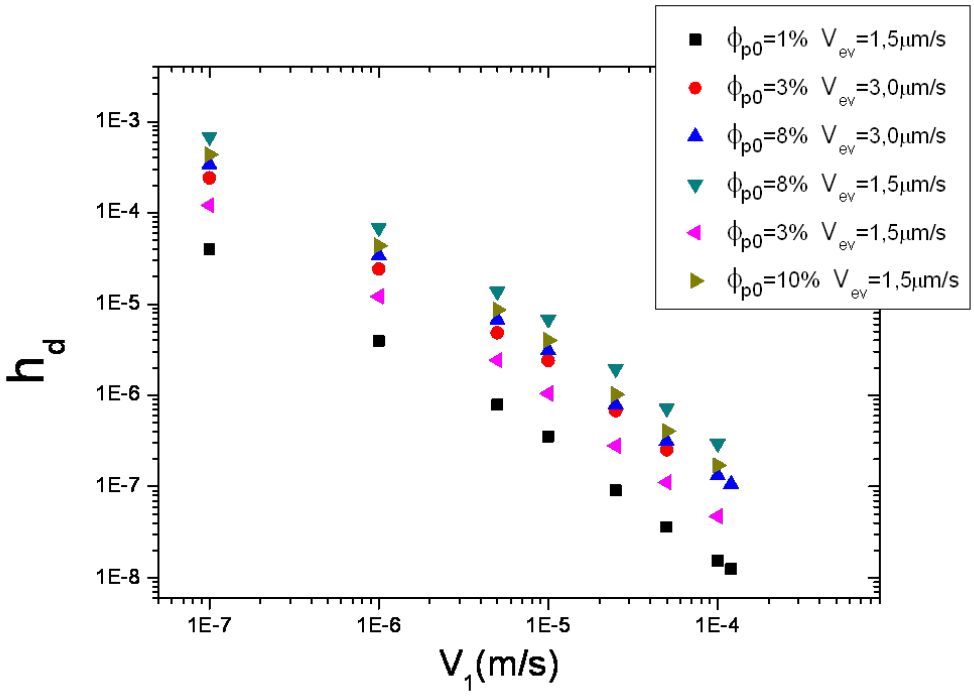

Figure 4.25: Film thickness versus substrate velocity.

The three heights give the same results.

4.4 Results and discussion

After validating some assumptions made in the boundary conditions, we can start to test all the parameters (the substrate velocity V_1, the initial solute volume fraction ϕ_{p0}, the mean evaporation velocity V_{ev}). We will compare the simulation results to a simple model, and also to the experimental results [33]. We will also discuss the effect of solution characteristics including dynamic viscosity and diffusion coefficient.

4.4.1 Prediction of deposit thickness

1. Deposit thickness by COMSOL simulation:

Figure 4.25 shows our results from COMSOL simulation. The dry thicknesses are deduced from the concentration along boundary 5 (cf section 4.1.5) $h_d = \frac{\bar{\phi}_p \times \delta \times \bar{V}_{tip}}{V_1}$. The configuration used here is:

- $H = 5mm$, $\alpha = 50\mu m$
- With 20 elements along boundary 5 for the mesh in the upper domain. Fine mesh in the other domain.
- Descritization are P2(velocity)+P1(pressure)+P2(concentration).
- $\mu = 0.001Pa \cdot s$, $D = 2 \times 10^{-10} m^2/s$.

Two mean evaporation velocities V_{ev} and three initial solute concentrations ϕ_{p0} are tested at different moving substrate velocities V_1. We can deduce the characteristic ratio $R_{com} = \frac{V_1 h_d}{F \phi_{p0}}$ for a later comparison. F (m^2/s) is the total volumetric flux along the meniscus surface and has a relation with the mean evaporation velocity as $F = V_{ev} \times d/2$ (cf Appendix D) in a total wetting case.

2. Deposit thickness by a simple model:

A simple model first proposed by Nagayama and co-authors [65] can also predict the deposit thickness shown in figure 4.26. The important assumptions of this model are: [33]

- There are two domains: the completely dried deposit which is in the tip part, and the liquid solution which is the major part (in color light blue). No transition domain between them.
- In a cross section L_y ($y = h = constant$), we assume uniform concentration ($\frac{\partial \phi_p}{\partial x} = 0$). In addition, the solute and solvent have equal densities.
- The following calculations are in steady state.

Based on global mass balance, the total flux going through L_y is either evaporating through the meniscus (solvent) or depositing on the substrate at the tip part (solute):

$$Q = \int_0^{d/2} v \, \mathrm{d}x = F + h_d \times V_1. \tag{4.19}$$

Where F is the total volumetric flux through the meniscus free surface, h_d is the deposition thickness. From solute mass balance, a second equation states that all the solute across the dash line (L_y) will deposit on the substrate.

$$Q_p = \int_0^{d/2} \phi_p v_p \, \mathrm{d}x = \int_0^{d/2} \phi_p v \, \mathrm{d}x = \phi_p \int_0^{d/2} v \, \mathrm{d}x = \phi_p \times Q. \tag{4.20}$$

This is by neglecting the diffusion term and assuming uniform concentration ϕ_p that will be considered as the bulk concentration ϕ_{p0}. Therefore, combining equation 4.19 and 4.20 with $\phi_{p0} \ll 1$, one can deduce:

$$R_{sm} \simeq \frac{h_d V_1}{F \phi_{p0}} = 1 \tag{4.21a}$$

3. Film thickness by experimental data fitting

By previous experimental studies on polymers and colloidal suspensions, there is an empirical law deduced by fitting the experimental data: $\frac{V_1 h_d}{V_{ev} \phi_{p0}} \simeq 330 \mu m = L_e$. Therefore, we have $R_{exp} = \frac{h_d V_1}{F \phi_{p0}} \simeq \frac{330}{500} \simeq 0.7$

In summary, we get for $\frac{h_d V_1}{F \phi_{p0}}$:

- $R_{sm} \simeq 1$ deduced from a simple model;
- $R_{exp} \simeq 0.7$ deduced from experimental data fitting;
- In the same way, R_{com} can be deduced from COMSOL simulation.

A summary is plotted in figure 4.27 which test various ϕ_{p0}, V_{ev} and V_1.

As can be seen, the three results have the same tendency: the higher substrate velocity, the lower value of $\frac{h_d}{\phi_{p0} V_{ev}}$. However, we found that for larger velocities ($> 10^{-5} m/s$),

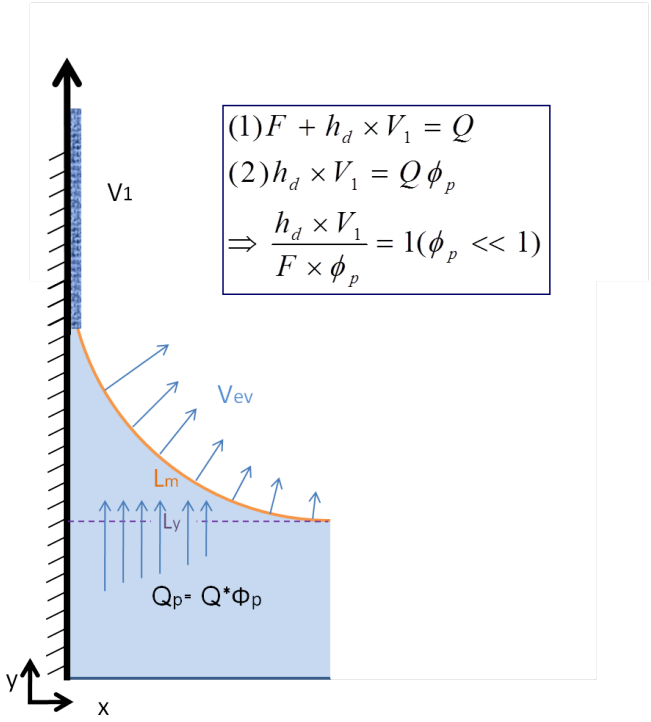

Figure 4.26: Simple model based on mass balance to deduce the deposit thickness.

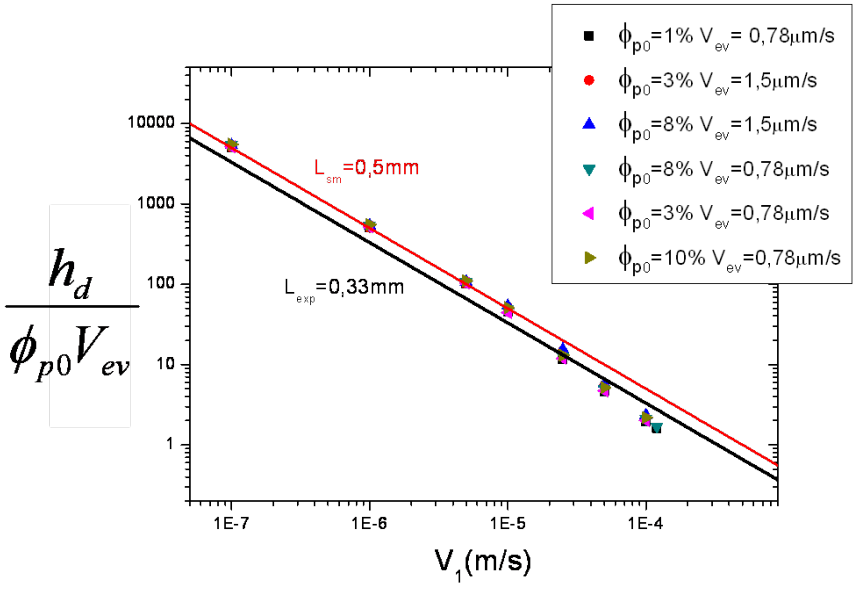

Figure 4.27: Three results comparison. Red line: simple model. Black line: experimental data fitting. Points: COMSOL simulations.

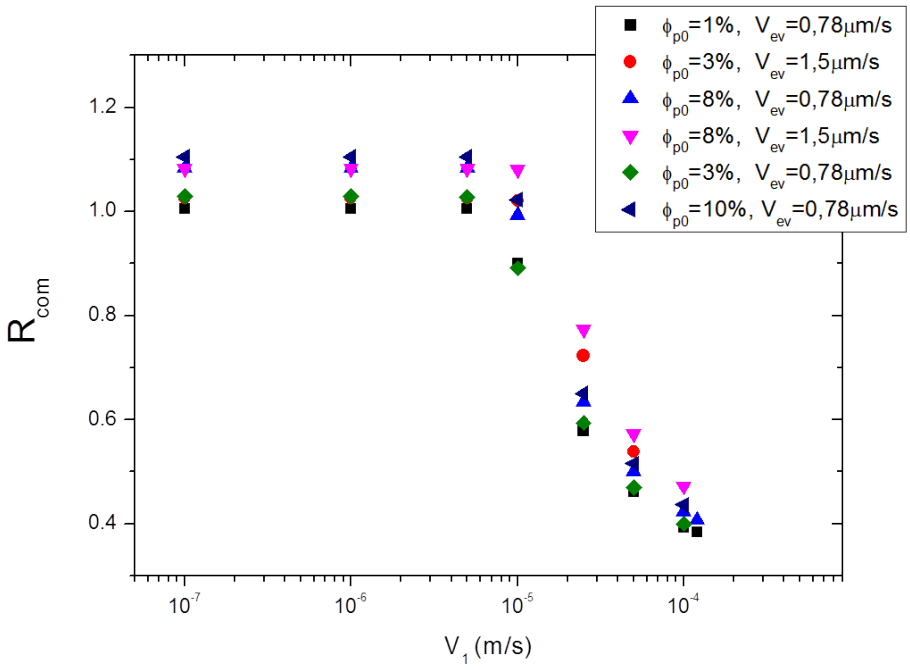

Figure 4.28: Characteristic length L_c normalized by L_m versus substrate moving velocity V_1. At low velocity, L_c is a constant, and it decreases when V_1 increases.

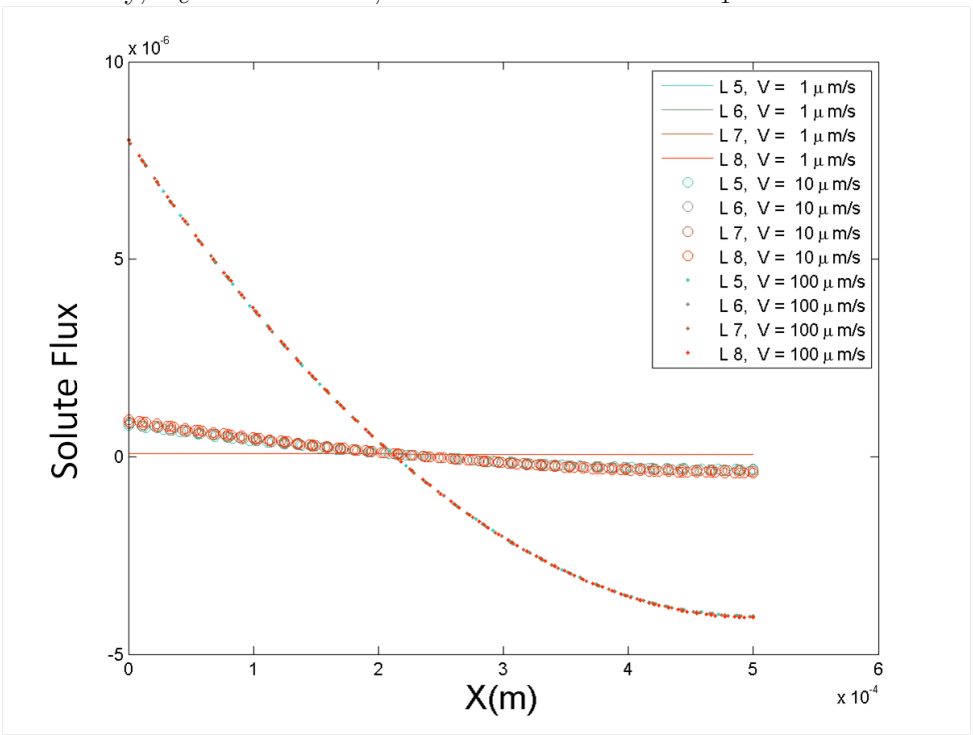

Figure 4.29: Flux distribution at cross sections (L5-L8) at the lower part of meniscus for three velocities.

V1	$\overline{\phi_p} \times \int_0^{d/2} v \cdot dx$	$\int_0^{d/2} \phi_p \times v \cdot dx$	Relative Error
1	3.41608E-11	3.4161E-11	-5.9E-6
10	3.4497E-11	3.1745E-11	0.087
100	3.19332E-11	1.3444E-11	1.38

Figure 4.30: Table to test the Nagayama assumption at different V_1.

the data from COMSOL simulations have no longer the same slope. To be more clear, we draw R_{com}. It is close to 1, i.e. to the simplified model at low velocities. The different values obtained for the different ϕ_{p0} are due to the approximation "$1 - \phi_{p0} \simeq 1$" used in the estimation of R_{com}. But a significant decreasing at velocities larger than $10\mu m/s$ is observed as shown in figure 4.28.

To explain the phenomena, we compare the solute flux along 4 cross sections at the lower part of meniscus (cf figure 4.19) for 3 velocities: low velocity($1\mu m/s$), median velocity $10\mu m/s$ and high velocity ($100\mu m/s$) as shown in figure 4.29.

- At low velocities, $V_1 = 1\mu m/s$, the flux ($\phi_p \times v$) is positive and uniform along the cross sections. There is no outflow across boundary B2.
- At median velocity $V_1 = 10\mu m/s$, the flux along the cross sections starts to become negative. It means the flow brings back some solute downward.
- At high velocity $V_1 = 100\mu m/s$, there is a significant negative part of the flux, which may break down the assumption of "uniform concentration" along x direction. Since the flow is large enough to bring back the solute, the thickness of the deposition will decrease as observed in figure 4.27.

As already mentioned, Nagayama's model assume a uniform solute volume fraction when computing the solute flux across the bottom boundary B2. Table 4.30 shows the approximation on the estimation of the solute flux, using the result of the numerical simulation as a reference. As can be seen, at low velocity ($V_1 = 1\mu m/s$), the two integrals are almost the same. The difference at $V_1 = 10\mu m/s$ is small (8%), while it is much large at $V_1 = 100\mu m/s$ (138%). When the velocity becomes large, the solute volume fraction is no longer constant along x direction. Therefore, Nagayama's assumption breaks down.

Even if experimental results show some dispersion, this transition between low and high velocities is not observed in the experiments. This means that some of the simplifying assumptions used in this model should be relaxed. This is beyond the scope of this work and will be discussed in the conclusion. In the next section we are going to study the influence of the viscosity and diffusion coefficient on the results.

4.4.2 Effect of viscosity

In this section, we will discuss the effect of solution viscosity . All above simulations have been performed with constant viscosity $\mu = 0.001Pa \cdot s$. To approach the experimental condition, a variable viscosity depending on the concentration is used. Kinetic viscosities as a function of solute volume fraction (polymer μ_p and colloids μ_c) are shown in the following equations:

$$\mu_p = 10^{\frac{-2.1827+7.9665\phi_p-6.2026\phi_p^2}{0.72-\phi_p}} Pa \cdot s., \tag{4.22a}$$

$$\mu_c = 0.912(1 - \phi_p/0.4125)^{-1.604} Pa \cdot s. \tag{4.22b}$$

The conditions for simulations are:

- mesh 10 elements at narrow region and fine mesh elsewhere.
- $\alpha = 15\mu m$, $H = 5mm$.

- $0.1\mu m/s < V_1 < 100\mu m/s$.
- $V_{ev} = 0.78\mu m/s$, $\phi_{p0} = 1\%$ and 8%.

Viscosity and flow distribution

Figure 4.31 shows one example at $V_1 = 10\mu m/s$ to estimate the effect of dynamic viscosity distributions. As can be seen the viscosity for the three cases are different. First, the viscosity for polymer or colloids are non-uniform and show small changes in the corner regions such as the tip part and the corner between B3 and B4. Second, the viscosity of the polymer is about 5 times larger than the viscosity of colloids shown in the color bar which is the concentration distribution. Third, the highest viscosity of polymer is one magnitude larger than the one of colloids.

However, it does not affect much the flow field which can be evidenced by stream lines and the concentration distribution plotted in figure 4.32.

Film thickness and cross sections

In order to quantitatively compare the viscosity effect, the film thickness is calculated by mass balance and plotted in figure 4.33. The thickness h_d of $\mu = 0.001$, μ_p and μ_c for different initial concentration $\phi_{p0} = 1\%, 8\%$ are identical. This is consistent to our experimental results where the film thickness was found independent on the solution viscosity (cf [33]).

Volume fraction distribution at upper meniscus along the cross sections(L1,L2,L3,L4) are plotted in figure 4.34. The **polymer** has the highest concentration distribution among the three cases, but note that it is less than 1% volume fraction difference and it is located at L1 for $x = 0.5mm$. For the velocity distribution and solute flux, the three cases are almost the same in the cross sections as shown in figure 4.35 and 4.36. And we found the same tendency for the lower part of meniscus (L5-L8).

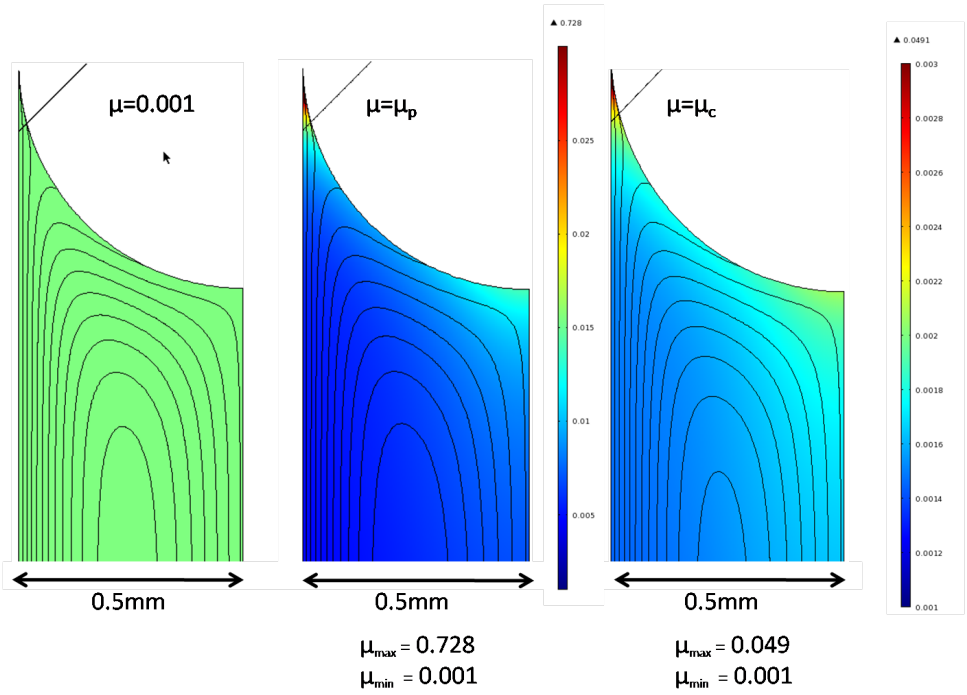

Figure 4.31: Viscosity distribution for: 1.Constant viscosity solution 2.Polymer solution ($\mu = \mu_p$) 3. Colloidal suspensions ($\mu = \mu_c$) in the condition of $V_{ev} = 0.78\mu m/s$, $\phi_{p0} = 8\%$.

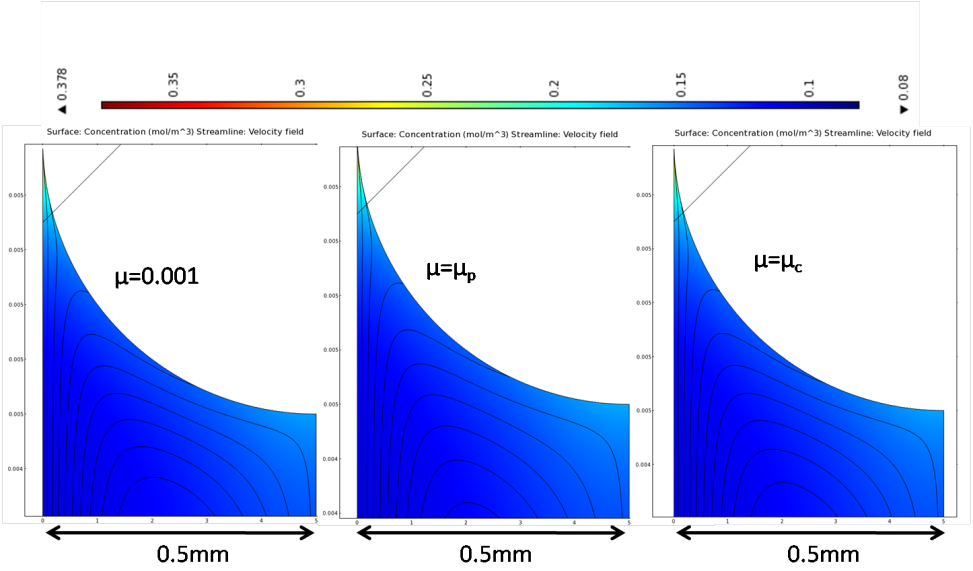

Figure 4.32: Concentration distribution and flow field for: 1.Constant viscosity solution 2.Polymer solution ($\mu = \mu_p$) 3. Colloidal suspensions ($\mu = \mu_c$) in the condition of $V_{ev} = 0.78\mu m/s$, $\phi_{p0} = 8\%$.

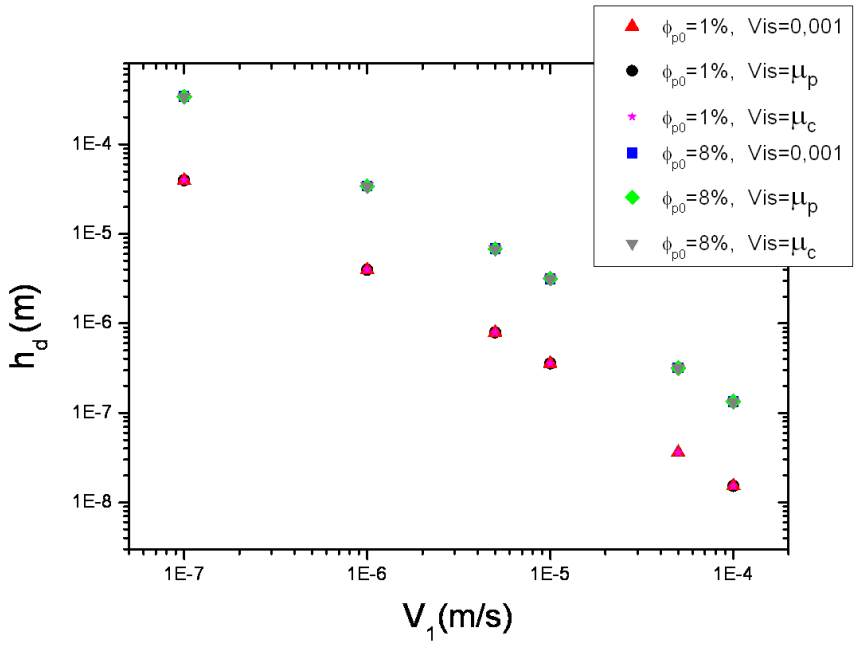

Figure 4.33: Deposition thickness plot.

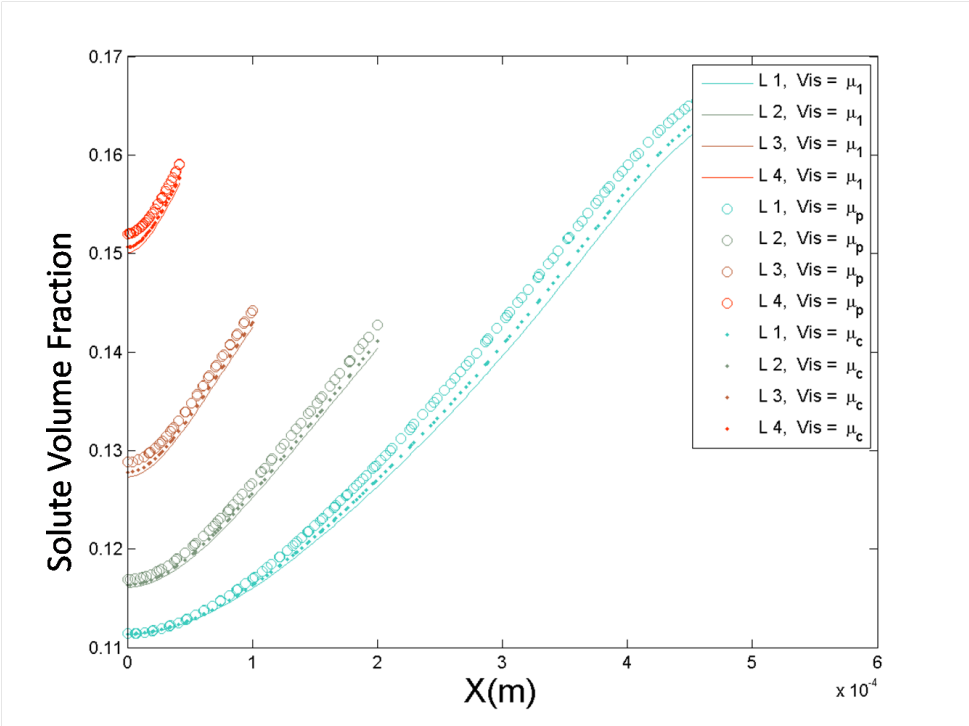

Figure 4.34: The concentration distribution along cross sections (L1-L4) at the upper part of meniscus for the three viscosities in the condition of $V_{ev} = 0.78\mu m/s$, $\phi_{p0} = 8\%$.

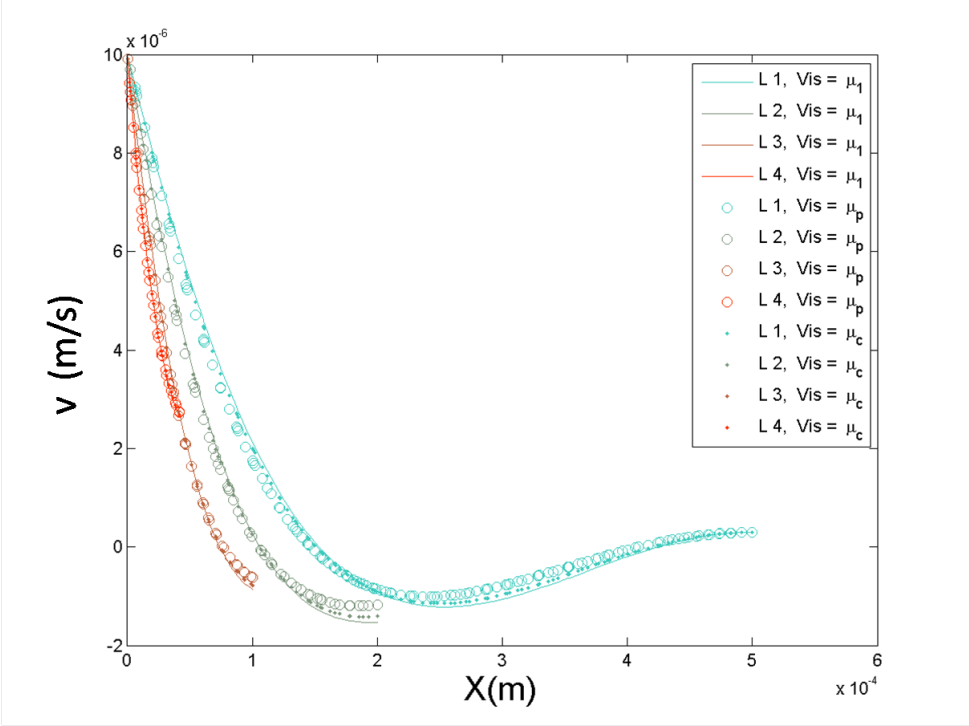

Figure 4.35: The velocity (v) profile along cross sections (L1-L4) at the upper part of meniscus for the three viscosities in the condition of $V_{ev} = 0.78\mu m/s$, $\phi_{p0} = 8\%$.

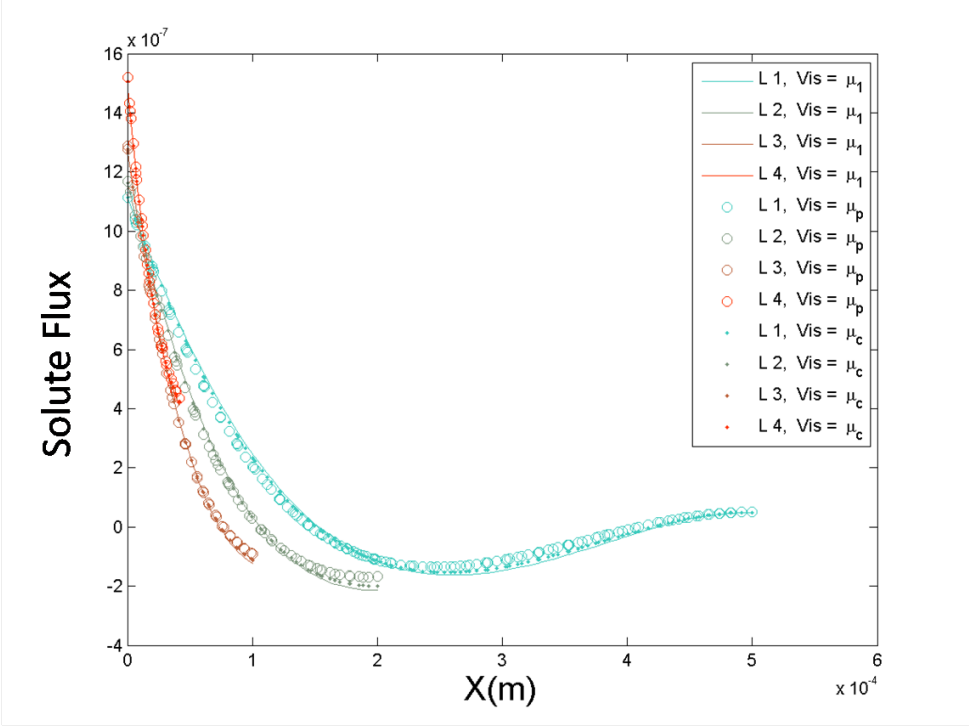

Figure 4.36: The solute flux along cross sections (L1-L4) at the upper part of meniscus for the three viscosities in the condition of $V_{ev} = 0.78\mu m/s$, $\phi_{p0} = 8\%$.

4.4.3 Effect of diffusion coefficient

It is known that the diffusion coefficient may depend on solute concentration. However, in our simulations, the solute volume fraction at the boundary B5 (truncated tip) is always smaller than 40%. Then we will assume that the diffusion coefficient D is almost constant, as shown in paper [66] for colloidal suspensions and in paper [60] for PAAm solutions. For colloids, the diffusion coefficient in the dilute regime can be described by Stokes-Einstein equation:

$$D = \frac{k_b T}{6\pi\mu R_p} \tag{4.23}$$

that is about $6 \times 10^{-12} m^2/s$ for $80nm$ particles. For polymers, experimental results obtained for PAAm solutions give a diffusion coefficient of about $2 \times 10^{-10} m^2/s$. Then in this section we will study the influence of D in the range $5 \times 10^{-12} m^2/s$ to $5 \times 10^{-10} m^2/s$, that is two orders of magnitude.

One special case is tested under parameters:

- the truncated region $\alpha = 15\mu m$ and $\delta = 0.225$.
- the mean evaporation velocity $V_{ev} = 0.78\mu m/s$.
- the initial volume fraction of solute $\phi_{p0} = 8\%$, dynamic viscosity $\mu = 0.001 Pa \cdot s$
- moving substrate velocity: $V_1 = 1, 10, 100\mu m/s$
- testing diffusion coefficient: $D = 5 \times 10^{-12}$, 2×10^{-11}, 6×10^{-11}, 9×10^{-11}, 2×10^{-10}, and $5 \times 10^{-10} m^2/s$.

Result is plotted in figure 4.37. At low velocity $V_1 = 1\mu m/s$, the deposition thickness does not depend on the diffusion coefficient (five green points are overlapped). Since only evaporation act as a pump for the flow field, all the flow goes toward the meniscus, there is no back flow to disturb/breakup the uniform concentration distribution (at x direction). The Nagayma's balance works well at low speed and diffusion dose not affect the

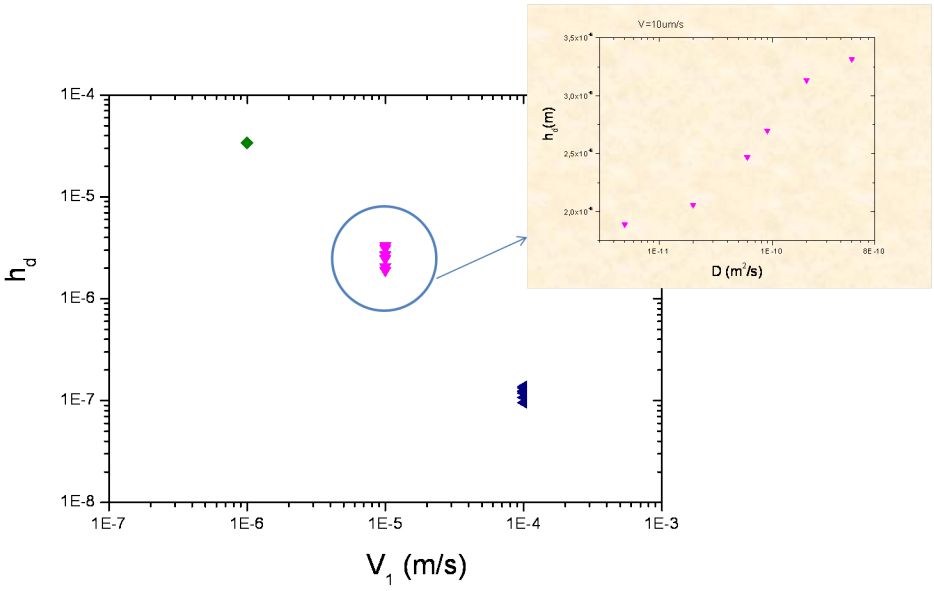

Figure 4.37: The film thickness comparison for different diffusion coefficients in the condition of $V_{ev} = 0.78\mu m/s$, $\phi_{p0} = 8\%$.

deposition.

At middle speed $V_1 = 10\mu m/s$, the higher the diffusion coefficient, the thicker deposition as shown in the insert in figure 4.37. One main reason is that when the velocity increases the Nagayama's balance was perturbed by the back flow due to convection. The diffusion plays a role to mix the solution. The larger diffusion coefficient, the more efficient the solute mixing. Therefore, some solute is brought back by diffusion and makes thicker deposition while the D increases. At high velocity $V_1 = 100\mu m/s$, the same tendency as $V_1 = 10\mu m/s$ is observed as shown in figure 4.37.

As a **conclusion**, this model was a first step to describe concentration and flow fields induced by the moving substrate and the evaporation at the meniscus free surface. It was shown that the cut-off introduced to suppress the divergence at the tip and the iterative procedure used to solve the problem allow to get pertinent results. However

some discrepancies between the simulations and experiments at high velocities show that some of the simplifying assumptions should be dropped. New mechanisms should then be taken into account. In a close future, this model will be improved by taking account **buoyancy** as well as **Marangoni** effect.

Chapter 5

Conclusion and outlook

5.1 Main results

The experimental set-up used in this study provides an accurate control of the substrate velocity and evaporation rate. Based on previous experiments [46, 48, 33], three regions can be defined for the film thickness, depending on the substrate velocities. At high velocities, we reach the dynamic regime governed by the Landau-Levich-Derjaguin theory. At lower velocities, we reach evaporative regime dominated by evaporation. At lower velocity, stick-slip motion can be observed and form periodic patterns.

In the first part of this study, we focus on experimental characterization in the **stick-slip regime**. The on-line recording of the contact line movement allows a detailed characterization of the stick-slip dynamic. **For colloidal suspensions**, we have studied the pinning force variation and the strip periodicity by systematically varying several parameters: receding velocity, particle size, and pH of the solution. Results show that the variation of the pinning force is proportional to $V_{ev}\Phi/V_1$ and does not depend on particles size or pH. The new results confirm the empirical law reported by Bodiguel *et al* [48], which is summarized in equation (3.7).

On the contrary, change in electrical surface charge changes the deposition morphologies significantly. At lower pH ($\lesssim pH2$) , the stripe patterns have lower wavelengths (a factor of 0.6 is obtained between S2 and S9). Besides, the downward slope is one order of

magnitude higher at lower pH than the one at high pH, therefore the shape of one stripe is asymmetric at lower pH unlike for higher pH's deposition. We tested several existing models but it appears there is currently no complete explanation for our results.

The same set-up and experimental parameters were then used for **polymer solution** (PAAm in water). Dried polymer films are almost flat at room temperature with only small undulations on the surface. It is only at high temperature ($60°C$) that we get clear and systematic stick-slip motion with periodic patterns. The same power law as for colloidal suspensions was found for the variation of pinning force. However, the preliminary results show different prefactors (1.4 for colloidal suspensions and 0.5 for polymer solutions). The wavelength of the polymer patterns is found smaller than the one of particle suspensions.

In the second part of our studies, we construct a **2D model** to simulate our experiment in the evaporative regime (stick-slip is not considered in this numerical part). In the first step presented here, we assume it is isothermal, without buoyancy or Marangoni effect. The velocity and concentration fields are thus only induced by the moving substrate and evaporation. The liquid phase flow and concentration gradients are obtained by solving the Stokes equations and Fick's law. At the meniscus free surface, a known but non uniform evaporation flux is imposed. The description for the contact line point is achieved by introducing an a priori cut-off α where boundary conditions result from a small scale description using lubrication approximation. Coupling the two models requires an iterative procedure to define the boundary conditions, based on a global mass balance for the truncated boundary. COMSOL software is used to solve the equations. The concentration distribution and velocity field are analyzed as a function of several parameters including: the solute bulk volume fraction ϕ_{p0}, the evaporation velocity V_{ev}, and the substrate moving velocity V_1. The drying film thickness can be deduced by mass balance which is then compared to our experimental results.

To validate our model, we first optimize the mesh by global mass balance. Then computational domain including meniscus height H and the truncated length α were

checked to be consistent with the assumptions used at the boundaries. After validation of the model, we compare to a simplified model based on global mass balance and assuming uniform concentration in a cross section. At low velocities ($V_1 < 10\mu m/s$), the two models have the same behavior. At high velocities ($V_1 > 10\mu m/s$), a small decreasing of the film thickness from the power law $\frac{h_d \times V_1}{\phi_{p0} V_{ev}} = 500\mu m$ (deduced from the simplified model) is observed. This can be explained by a break-up of the assumption of uniform concentration distribution in the bulk. A back flow induced by higher substrate velocity V_1 brings back the solute so that the film thickness is smaller. After understanding our model, we tested the viscosity effect and the diffusion coefficient effect. Results are consistent with our previous experiments [33]: in the evaporative regime, the film thickness does not depends on the viscosity. This is confirmed by observing the concentration distribution as well as the velocity field distribution.

5.2 Outlook

Experiment

From an engineering point of view, it is useful to control the final pattern by manipulating several parameters. Evaporation rate, substrate velocity and initial concentration have been well studied for our system. In the future, it would be interesting to change the system properties such as the **wettability** of the substrate (hydrophobic/hydrophilic/pre-patterned), the **properties** of the solutions (organic solvent/biomolecules solution/nano-material solutions), etc.

Moreover, it should be also interesting to perform **local observations** of the meniscus in order to **test our model** and **improve our understanding of the stick-slip mechanism**. One thing we could try is to get the **meniscus slope** by optical methods (for example, light interference [67] method or free-surface synthetic Schlieren (FS-SS) method [68, 69]), and the local **concentration and velocity fields** by using confocal microscope [70] or by Raman spectroscopy [71]. Despite the fact that some of these methods have been successfully applied to droplets, the application to our geometry is

still challenging (due to the high curvature meniscus shape) and will need feasibility study.

Simulation

In parallel, the next step for our 2D model should be to test the substrate wettability. Gap size will also be interesting to study because experimentally it is difficult to achieve (one order of magnitude smaller/larger than gap width = 1mm is not realistic for experiments, because $100\mu m$ has parallelism issue to solve and 10mm is too large to have a capillary rise).

From our simulation we found that the model is too simple to describe the hydrodynamic behavior at higher substrate withdraw speed ($V_1 > 100\mu m/s$). In order to improve our model, the next step can be adding buoyancy effect and Marangoni effect for the flow. Another interesting work will be to change from a steady state to a dynamic one (using Deformed-Mesh-Physics in COMSOL software) which implies the shape of the meniscus may change during the movement of the contact line. This is experimentally challenged. It has a potential to explain the periodic behavior of the final deposit patterns.

Appendix A

Debye Length in an electrolyte

One example is shown here to deduce the Debye-Length κ^{-1} for aqueous solutions NaCl at $25°C$. The definition of Debye length is following:

$$\kappa^{-1} = \left(\frac{e^2}{\epsilon\epsilon_0 k_B T} \Sigma_i n_i {z_i}^2 \right)^{-1/2} \tag{A.1}$$

where e is the electron charge ($1.6 \times 10^{-19} C$), ϵ is the relative dielectric constant for water at $25°C$ ($= 78.5$). ϵ_0 is the permittivity in vacuum ($= 8.854 \times 10^{-12} F/m$), k_B is the Boltzmann constant ($= 1.38 \times 10^{-23} J/K$), T is the temperature (assumed $298.2K$), n_i is the ion concentration ($ions/m^3$), z_i is the ion valence. For NaCl $z_i = 1$, we get:

$$\kappa^{-1} \simeq \ 3.055 \times 10^{-10} M^{-0.5} \tag{A.2a}$$

where M is the concentration in"mole/liter".

Appendix B

Comparison for 2 size particles

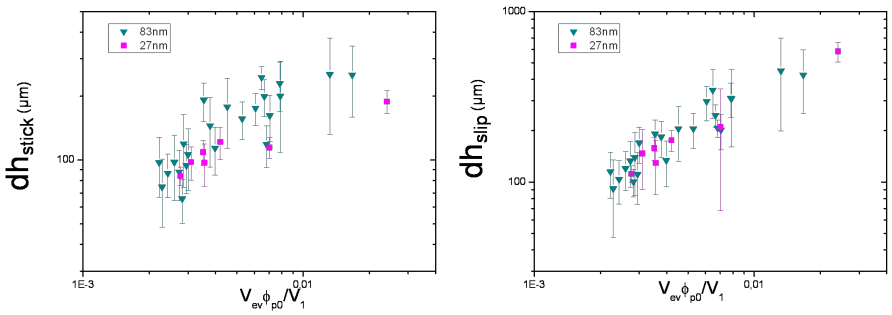

Figure B.1: dh_{stick} and dh_{slip} for both size particles.

Two different size of the silica particles ($D_p = 83nm$ and $D_p = 27nm$) are tested in the experiments at high pH values. Close results are obtained for dh_{stick}, dh_{slip}, V_{slip}, V_{stick} and the ratio between V_{slip} and V_{stick}.

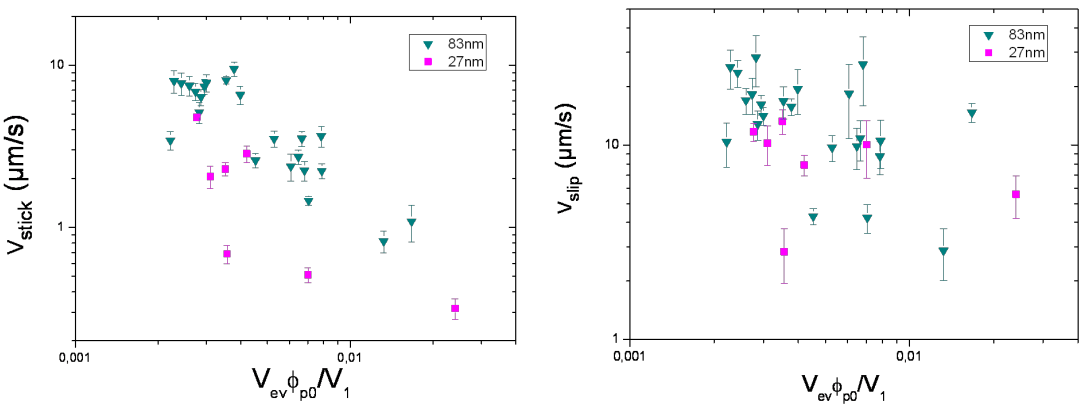

Figure B.2: V_{stick} and V_{slip} for both size particles.

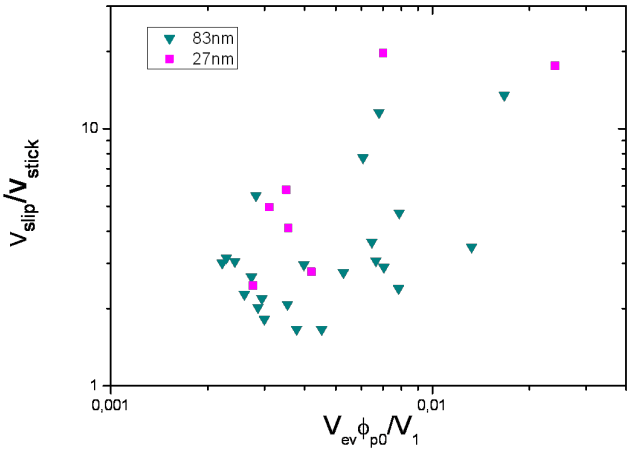

Figure B.3: Ratio between V_{slip} and V_{stick} for both size particles.

Appendix C

Mass flux J

In our discussion of normal flux due to evaporation across the meniscus free surface, **mass flux** J (density $\times$ velocity) with **SI** unit in kg/m^2s is discussed. For non volatile solute (p) and for volatile solvent (s) with evaporation rate j, one can write following equations:

$$\vec{J} = \rho\vec{v} = \rho_s\vec{v}_s + \rho_p\vec{v}_p, \quad (\rho = \rho_s + \rho_p)\,, \tag{C.1a}$$

$$w_s = \frac{\rho_s}{\rho}, \quad w_p = \frac{\rho_p}{\rho}\,, \tag{C.1b}$$

$$\vec{v} = w_s\vec{v}_s + w_p\vec{v}_p\,, \tag{C.1c}$$

$$\rho_p\vec{v}_p \cdot \vec{n} = 0\,, \tag{C.1d}$$

$$\rho_s\vec{v}_s \cdot \vec{n} = \frac{j}{\bar{V}_s}. \tag{C.1e}$$

with notations defined as:

- ρ_s is solvent density, ρ_p is solute density. Both are in the unit of kg/m^3.
- $\vec{v}_s$ is solvent velocity, $\vec{v}_p$ is polymer velocity. Both are in the unit of m/s.
- $w_s = \rho_s/\rho$ is solvent mass fraction and $w_p = \rho_p/\rho$ is solute mass fraction.

$\bar{V}_s = 1/\rho_s^0$ is defined as the inverse of **pure solvent** density, called solvent specific volume, which is a constant in our case. $\bar{V}_p = 1/\rho_p^0$ is the specific volume of **pure solute**. With $\phi_s = \rho_s \bar{V}_s$ is solvent volume fraction and $\phi_p = \rho_p \bar{V}_p$ is solute volume fraction we get:

$$w_p = \frac{\phi_p}{\frac{\bar{V}_p}{\bar{V}_s} + (1 - \frac{\bar{V}_p}{\bar{V}_s})\phi_p} \tag{C.2a}$$

In our model, we suppose $\bar{V}_p = \bar{V}_s$, namely pure solute and pure solvent have the same density $\rho_s^0 = \rho_p^0$. Combined with equation (C.1c):

$$w_p = \phi_p, \quad w_s = \phi_s\,, \tag{C.3a}$$

$$\vec{v} \cdot \vec{n} = w_s \vec{v}_s \cdot \vec{n} + w_p \vec{v}_p \cdot \vec{n}\,, \tag{C.3b}$$

$$= \phi_s \vec{v}_s \cdot \vec{n} + \phi_p \vec{v}_p \cdot \vec{n} \tag{C.3c}$$

From equation (C.1e), the evaporation rate across the free surface can be written:

$$j = \bar{V}_s \rho_s \vec{v}_s \cdot \vec{n} \tag{C.4a}$$

$$= \phi_s \vec{v}_s \cdot \vec{n} \tag{C.4b}$$

$$= \vec{v} \cdot \vec{n} - \phi_p \vec{v}_p \cdot \vec{n} \tag{C.4c}$$

$$= \vec{v} \cdot \vec{n} - w_p \vec{v}_p \cdot \vec{n} \tag{C.4d}$$

$$= \vec{v} \cdot \vec{n} \tag{C.4e}$$

$$= u_n \tag{C.4f}$$

Appendix D

Volumetric flux F

We call F the total volumic flux due to solvent evaporation, by unit length in the z direction orthogonal to the directions x, y of our 2D model. The unit is then m^2/s. From the local evaporation rate j, based on our assumption, $j = J_0/\sqrt{H-y}$ (cf figure 4.1), we get the total volume flux F by integral along the meniscus free surface (ds):

$$F = \int_{H-h_m}^{H} j(y)\, ds\,, \tag{D.1a}$$

$$= \int_{H-h_m}^{H} \frac{J_0}{\sqrt{H-y}}\, ds\,, \tag{D.1b}$$

$$= J_0 \times h_m \int_{H-h_m}^{H} \frac{dy}{\sqrt{(H-y)(h_m-H+y)(h_m+H-y)}} \tag{D.1c}$$

Where J_0 is a constant, H is the total height of the meniscus, and h_m is vertical distance of the meniscus free surface (cf figure 4.1).
From the contact line movement in pure water evaporation experiment (cf section 2.4), we deduce the mean evaporation velocity V_{ev}(m/s) defined in the following way:

$$F = d/2 \times V_{ev} \tag{D.2}$$

where d is gap width between the two substrates. For a total wetting case ($\theta_{eff} = 0$),

$h_m = d/2$. Combine the two equations (D.1c) and (D.2), we can get the mean evaporation velocity V_{ev}:

$$V_{ev} = J_0 \int_{H-R}^{H} \frac{dy}{\sqrt{(H-y)(R-H+y)(R+H-y)}} \tag{D.3}$$

where $R = d/2 = h_m$ is the radius of the meniscus in a total wetting condition. By changing J_0 we can change the mean evaporation rate for model testing. In our configuration ($d = 1mm$, total wetting), we get $V_{ev} \simeq 117 J_0$.

Appendix E

COMSOL implemetation

E.1 Domain physics and boundary conditions

Transport of dilute species (chds):

- Choose **Stationary** for equations and **convection** for additional transport mechanisms.
- Choose the discretization **quadratic** for the variable c.
- Enter diffusion coefficient $D_c = 2^{10}$.
- Enter $c0$ as the initial value for concentration.
- Add **No flux** at B1(moving wall) and B4 (the meniscus).
- Add **Open boundary** for B2 (bottom boundary)which we supposed a fully developed flow, enter $c0$ for $C_{0,c}$.
- Add **Open boundary** for B5 (the truncated part), enter 0.5 for $C_{0,c}$.
- Add **Symmetric boundary** condition for B3(symmetric wall).

Creeping flow(spf):

- Choose **Stationary** for equations and **Incompressible flow neglect inertial term (Stokes flow)** for Physical Model.

- Choose **Streamline diffusion** for Consistent Stabilization.
- Choose the discretization **P2+P1**, which means quadratic discretization for velocity and linear discretization for pressure.
- Set fluid properties: enter $\rho = 1kg/m^3$ and dynamic viscosity $\mu = 0.001Pa \cdot s$.
- Set initial conditions: $u = 0; v = 0; p = 0$.
- Add **moving wall** for B1, set $u = 0$ and $v = V_1$.
- Add **inlet** for B2, choose **pressure, no viscous stress type**, enter 0 for pressure.
- Add **pointwise constraint** for B2, choose **Bidirectional, symmetric** for constrain type. Enter **u** for constraint expression.
- Add **Symmetry** boundary for B3.
- Add **Boundary Stress** for B4 and choose **General stress**for boundary condition. Enter **0** for both component of stress.
- Add **pointwise constrain** for B4, set $u*nx+v*ny-Vev$ in Constrain expression. Choose **Lagrange** for shape function type and **Quadratic** for discretization.
- Add **Leaking wall** for B5 and set:

$$\begin{aligned} u &= (Vav * d\_delta\_dy * (3 * delta - 2 * x) + V1 * d\_delat\_dy * (2 * x - 3 * delta) \\ &\quad + delta * d\_Vav\_dy * (x - 3 * delta)) * x^2/2/delta^3\,, \\ v &= 3 * (Vav - V1) * x * (1 - x/2/delta)/delta + V1\,. \end{aligned}$$

E.2 Global definitions

Add **Parameters** and **Variables** in Global definitions. Set all the parameters and variable by typing as the following figures. Figure E.1 is for parameters and figure E.2 is for variables.

Parameters

Name	Expression	Value	Description
Ht	5[mm]	0.005 m	total hight
d	1[mm]	0.001 m	gap width
delta	2.5[um]	2.5E-6 m	truncated width
eta	50[um]	5.0E-5 m	truncated hight
V1	100[um/s]	1.0E-4 m/s	moving wall
Vav	5.0E-5	5.0E-5	Aver. vel. on tip leaking
R	d/2	5.0E-4 m	radius of the meniscus
theta	0	0	contact angle
c0	0.01	0.01	initial volume fraction

Figure E.1: Global definition of parameters

Variables

Name	Expression	Unit	Description
j0	6.7e-9		Evap rate constant
Vev	j0[m/s]/((Ht-y)/1[m])^0.5	m/s	Evap rate
d_delta_dy	(y-Ht)/R-theta		
d_Vav_dy	-(Vev+Vav*d_delta_dy)/delta		

Figure E.2: Global definition of variables

Bibliography

[1] A. D. Nikolov and D. T. Wasan. Mechanisms of the assembly of nano- and microparticle two-dimensional structures in a wedge film. *Industrial and Engineering Chemistry Research*, 48:2320, 2009.

[2] D. Brutin, B. Sobac, B.Loquet, and J. Sampol. Pattern formation in drying drops of blood. *J. Fluid Mech.*, 667:85, 2011.

[3] J. Park, J. Moon, H. Shin, D. Wang, and M. Park. Direct-write fabrication of colloidal photonic crystal microarrays by ink-jet printing. *Journal of colloid and interface science*, 298:713, 2006.

[4] J. Wang and J. R. G. Evans. Segregation in multicomponent ceramic colloids during drying of droplets. *Physical Reveiw E*, 73:021501, 2006.

[5] B. Trnovec, M. Stanel, U. Hahn, A.C. Hubler, H. Kempa, R. Sangl, and M. Forster. coated paper for printed electronics. *PRINTED ELECTRONICS*, 1:48, 2009.

[6] R. D. Deegan, O. Bakajin, T. F. Dupont, G. Huber, S. R. Nagel, and T. A. Witten. Capillary flow as the cause of ring stains from dried liquid drops. *Nature*, 389:827, 1997.

[7] J. Jia, B. Wang, A. Wu, G. Cheng, Z. Li, and S. Dong. A method to construct a third-generation horseradish peroxidase biosensor: Self-assembling gold nanoparticles to three-dimensional sol-gel network. *Anal. Chem.*, 74:2217, 2002.

[8] C. Boozer, Q. Yu, S. Chen, C.Y. Lee, J. Homola, S.S. Yee, and S. Jiang. Surface functionalization for self-referencing surface plasmon resonance (spr) biosensors by multi-step self-assembly. *Sensors and actuators B*, 90:22, 2003.

[9] M. Schaeferling, S. Schiller, H. Paul, M. Kruschina, P. Pavlickova, M. Meerkamp, C. Giammasi, and D. Kambhampati. Application of self-assembly techniques in the design of biocompatible protein microarray surfaces. *ELECTROPHORESIS*, 23:3097, 2002.

[10] V. Sivagnanam, A. sayah, and M. A. M. Gijs. Bead-based single protein micro-array realized through electrostatic self-assembly of carboxylated beads. *Microelectronic Engineering*, 85:1355, 2008.

[11] Y. Xia, B. Gates, Y. Yin, and Y. Lu. Monodispersed colloidal spheres: Old materials with new applications. *Advanced Materials*, 12(10):693–713, 2000.

[12] Y. A. Vlasov, X. Bo, J. C. Sturm, and D. J. Norris. On-chip natural assembly of silicon photonic bandgap crystals. *Nature*, 414:289, 2001.

[13] L. Leger, M. Erman, A. M. Guinet-Picard, D. Ausserre, and C. strazielle. Precursor film profiles of spreading liquid drops. *Physical Review Letter*, 60:2390, 1988.

[14] R. K. Roeder and E. B. Slamovich. Measuring the critical thickness of thin metalorganic precursor films. *Journal of Materials Research*, 14(6):2364, 1999.

[15] R. D. Deegan, O. Bakajin, T. F. Dupont, G. Huber, S. R. Nagel, and T. A. Witten. Contact line deposits in an evaporating drop. *PHYSICAL REVIEW E*, 62:756, 2000.

[16] A. G. Marin, H. Gelderblom, D. Lohse, and J. H. Snoeijer. Order-to-disorder transition in ring-shaped colloidal stains. *Physical Review Letters*, 107:085502, 2011.

[17] I. I. Smalyukh, O. V. Zribi, J. C. Butler, O. D. Lavrentovich, and G. C. L. Wong. Structure and dynamics of liquid crystalline pattern formation in drying droplets of dna. *Physical Review Letters*, 96:177801, 2006.

[18] B. M. Weon and J. H. Je. Capillary force repels coffee-ring effect. *Physical Review E*, 82:015305, 2010.

[19] C. Monteux and F. Lequeux. Packing and sorting colloids at the contact line of a drying drop. *Langmuir*, 27:2917, 2011.

[20] T. S. Wong, T. H. Chen, X. Shen, and C. M. Ho. Nanochromatography driven by the coffee ring effect. *Analytical Chemistry*, 83:1871, 2011.

[21] H. Hu and R. G. Larson. Analysis of the effect of marangoni stresses on the microflow in an evaporating sessile droplet. *Langmuir*, 21(9):3963, 2005.

[22] H. Hu and R. G. Larson. Analysis of the effect of marangoni stresses on the microflow in an evaporating sessile droplet. *Langmuir*, 21(9):3972, 2005.

[23] H. Hu and R. G. Larson. Marangoni effect reverses coffee-ring depositions. *Journal of Physical Chemistry B*, 110(14):7090, 2006.

[24] X. Xu and J. Luoa. Marangoni flow in an evaporating water droplet. *APPLIED PHYSICS LETTERS*, 91:124102, 2007.

[25] W. D. Ristenpart, P. G. Kim, C. Domingues, J. Wan, and H. A. Stone. Influence of substrate conductivity on circulation reversal in evaporating drops. *Physical Review Letters*, 99(23):234502, 2007.

[26] Daniel M. Kuncicky and Orlin D. Velev. Surface-guided templating of particle assemblies inside drying sessile droplets. *Langumuir*, 24:1371, 2008.

[27] J. Leng. Drying of a colloidal suspension in confined geometry. *Physical Review E*, 82:021405, 2010.

[28] P. J. Yunker, T. Still, M. A. Lohr, and A. G. Yodh . Suppression of the coffee-ring effect by shape-dependent capillary interactions. *Nature*, 476:308, 2011.

[29] Q. Yan, L. Gao, V. Sharma, Y. Chiang, and C. C. Wong. Particle and substrate charge effects on colloidal self-assembly in a sessile drop. *Langmuir*, 24:11518, 2008.

[30] R. Bhardwaj, X. Fang, and D. Attinger. Pattern formation during the evaporation of a colloidal nanoliter drop: a numerical and experimental study. *New Journal of Physics*, 11:075020, 2009.

[31] R. Bhardwaj, X. Fang, P. Somasundaran, and D. Attinger. Self-assembly of colloidal particles from evaporating droplets: Role of dlvo interactions and proposition of a phase diagram. *Langumuir*, 26:7833, 2010.

[32] H. Yabu and M. Shimomura. Preparation of self-organized mesoscale polymer patterns on a solid substrate: Continous pattern formation from a receding meniscus. *Adv. Funct. Mater.*, 15:575, 2005.

[33] H. Bodiguel G. Jing, F. Doumenc, E. Sultan, and B. Guerrier. Drying of colloidal and polymer solutions near the contact line: deposit thickness at low capillary. *Langumuir*, 26:4, 2010.

[34] M. Le Berre, Y. Chen, and D. Baigl. From convective assembly to landau-levich deposition of multilayered phospholipid films of controlled thickness. *Langmuir*, 25:2554, 2009.

[35] M. Faustini, B. Louis, P. A. Albouy, M. Kuemmel, and D. Grosso. Preparation of sol-gel films by dip-coating in extreme conditions. *J. Phys. Chem. C*, 114:7637, 2010.

[36] G. Berteloot, C.-T. Pham, A. Daerr, F. Lequeux, and L. Limat. Evaporation-induced flow near a contact line: Consequences on coating and contact angle. *EPL*, 83:14003, 2008.

[37] F. Doumenc and B. Guerrier. Drying of a solution in a meniscus: A model coupling the liquid and the gas phases. *Langumuir*, 26:17, 2010.

[38] Alain de Ryck and D. Quere. Gravity and inertia effects in plate coating. *Journal of Colloid and Interface Science*, 203:278, 1998.

[39] Maniya Maleki, Etienne Reyssat, David Qur, and Ramin Golestanian. On the landau-levich transition. *Langmuir*, 23:10116, 2007.

[40] D. M. Campana, S. Ubal, M. D. Giavedoni, and F. A. Saita. A deeper insight into the dip coating process in the presence of insoluble surfactants: A numerical analysis. *PHYSICS OF FLUIDS*, 23:052102, 2011.

[41] Satoshi Watanabe, Koji Inukai, Shunsuke Mizuta, and Minoru T. Miyahara. Mechanism for stripe pattern formation on hydrophilic surfaces by using convective self-assembly. *Langmuir*, 25:7287, 2009.

[42] Z. Lin and S. Granick. Patterns formed by droplet evaporation from a restricted geometry. *J. Am. Chem. Soc.*, 127:2816, 2005.

[43] Manouk Abkarian, Janine Nunes, and Howard A. Stone. Colloidal crystallization and banding in a cylindrical geometry. *JACS*, 126:5978, 2004.

[44] J. Xu, J. F. Xia, S. W. Hong, Z. Q. Lin, F. Qiu, and Y. L. Yang. Self-assembly of gradient concentric rings via solvent evaporation from a capillary bridge. *Physical Review Letters*, 96:066104, 2006.

[45] Moniraj Ghosh, Fengqiu Fan, and Kathleen J. Stebe. Spontaneous pattern formation by dip coating of colloidal suspensions on homogeneous surfaces. *Langmuir*, 23:2180, 2007.

[46] H. Bodiguel, F. Doumenc, and B. Guerrier. Patterns formation during the drying of a colloidal suspension; pinning of a receding contact line. *EPJ-ST*, 166:29, 2009.

[47] J. Alex Lee, Kayla Reibel, Mark A. Snyder, L. E. Scriven, and Michael Tsapatsis. Geometric model describing the banded morphology of particle films formed by convective assembly. *Chem. Phys. Chem*, 10:2116, 2009.

[48] H. Bodiguel, F. Doumenc, and B. Guerrier. Stick-slip patterning at low capillary numbers for an evaporating colloidal suspension. *langumuir*, 26:13, 2010.

[49] Lubor Frastia, Andrew J. Archer, and Uwe Thiele. Dynamical model for the formation of patterned deposits at receding contact lines. *PRL*, 106:077801, 2011.

[50] E. Rio, A. Daerr, F. Lequeux, and L. Limat. Moving contact lines of a colloidal suspension in the presence of drying. *Langmuir*, 22(7):3186–3191, 2006.

[51] D. Orejon, K. Sefiane, and M. E. R. Shanahan. Stick-slip of evaporating droplets: Substrate hydrophobicity and nanoparticle concentration. *Langmuir*, 27(21):12834, 2011.

[52] R. Bhardwaj, X. Fang, and D. Attinger. Pattern formation during the evaporation of a colloidal nanoliter drop: a numerical and experimental study. *New J. Phys.*, 11(7):075020, 2009.

[53] A.J. Petsi, A.N. Kalarakis, and V.N. Burganos. Deposition of brownian particles during evaporation of two-dimensional sessile droplets. *Chem. Eng. Sci.*, 65(10):2978, 2010.

[54] Surface patterning via evaporation of ultrathin films containing nanoparticles. *J. Colloid Interface Sci.*, 267(1):92, 2003.

[55] R. V. Crasterand, O. K. Matar, and K. Sefiane. Pinning, retraction, and terracing of evaporating droplets containing nanoparticles. *Langmuir*, 25(6):3601, 2009.

[56] J. F. Zhao, Z. Y. Luo, M. J. Ni, and K. F. Cen. Dependence of nanofluid viscosity on particle size and ph value. *Chin. Phys. Lett.*, 26:066202, 2009.

[57] J. Mewis and N.J. Wagner. *Colloidal Suspension Rheology.* Cambridge University Press, 2012.

[58] V.Trappe, V. Prasad, L. Cipelletti, P. N. Segre, and D. A. Weitz. Jamming phase diagram for attractive particles. *Nature*, 411:14, 2001.

[59] B. P. COOK, A. L. BERTOZZI, and A. E. HOSOI. Shock solutions for particle-laden thin films.

[60] D. A. Mezquia, F. Doumenc, and M. M. Bou-Ali. Sorption isotherm, glass transition, and diffusion coefficient of polyacrylamide water solutions. *Journal of chemical and engineering data*, 57:776, 2012.

[61] P. Yimsiri and M.R. Mackley. Spin and dip coating of light-emitting polymer solutions: Matching experiment with modelling. *Chem. Eng. Sci.*, 61:3496, 2006.

[62] L. Shmuylovich, A. Q. Shen, and H. A. Stone. Surface morphology of drying latex films: Multiple ring formation. *Langmuir*, 18:3441, 2002.

[63] P. G. de Gennes. Wetting: statics and dynamics. *Rev. Mod. Phys.*, 57:827–863, 1985.

[64] F. Doumenc and B. Guerrier. Drying of a solution in a meniscus: A model coupling the liquid and the gas phases. *Eur. Phys. J. Special Topics*, 197:281, 2011.

[65] E. Adachi, A. Dimitrov, and K. Nagayama. Stripe patterns formed on a glass surface during droplet evaporation. *Langumuir*, 11:1057, 1995.

[66] L.Daubersies and J. B. Salmon. Evaporation of solutions and colloidal dispersions in confined droplets. *Physical Review E*, 84:031406, 2011.

[67] G. Guna, P. Allanson, and A. M. Cazabat. Receding contact angle in the situation of complete wetting: Experimental check of a model used for evaporating droplets. *Colloids and surfaces A*, 300:307, 2007.

[68] F. Moisy, Marc Rabaud, and K. Salsac. A synthetic schlieren method for the measurement of the topography of a liquid interface. *Exp Fluids*, 46:1021, 2009.

[69] M. Banahaa, A. Daerr, and L. Limat. Spreading of liquid drops on agar gels. *EPJ-ST*, 166:185, 2009.

[70] H. Bodiguel and Jacaues Leng. Imaging the drying of a colloidal suspension. *Soft Matter*, 6:5451, 2010.

[71] C. Monteux A. Tay, T. Narita, Y. De Wilde, and F. Lequeux. The role of hydration in the wetting of a soluble polymer. *Soft Matter*, 5:3713, 2009.